Meanders as a toy model of two-dimensional quantum gravity

Thesis BSc Physics and Astronomy

Radboud University Nijmegen

Faculty of Science

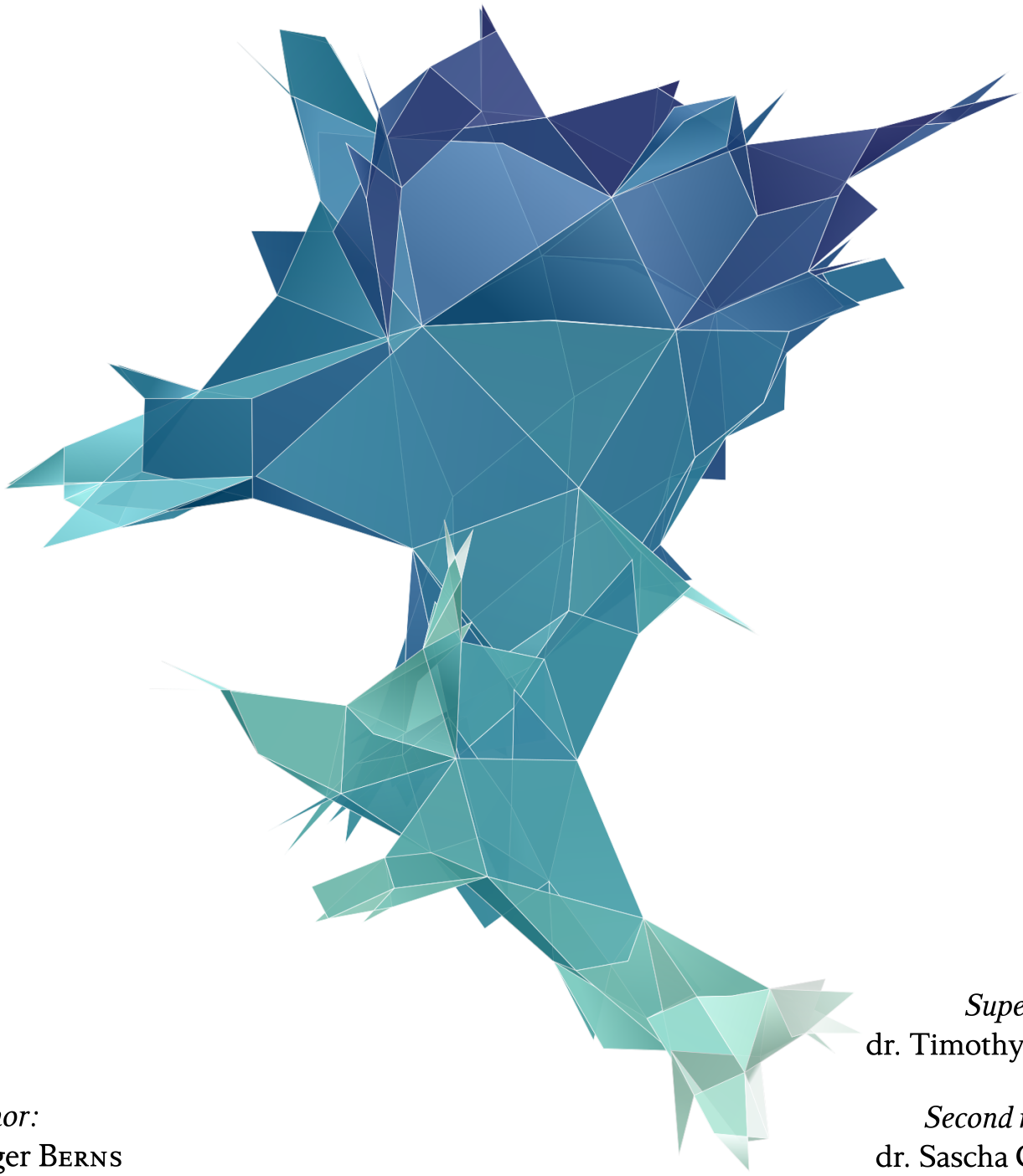

Author:
Rutger Berns

Supervisor:
dr. Timothy Budd

Second reader:
dr. Sascha Caron

August 2022

The image on the cover is a 3D visualisation of a discrete surface which in the continuum limit is two-dimensional quantum gravity. The discrete surface is drawn by a spring layout using NetworkX and visualised using Manim Community.

Abstract

Two-dimensional quantum gravity (2DQG) can be seen as the continuum limit of discrete random surfaces. Matter can be introduced in 2DQG by coupling it to a statistical system. Meanders are a combinatorial problem of non-intersecting, closed, self-avoiding loops and are conjectured to be a statistical system coupled to 2DQG. In the 90s, Di Francesco et al. made several predictions about the critical exponents of 2DQG coupled to the statistical system of meanders in [1, 2]. In this work, the predictions of Di Francesco et al. are studied numerically using Markov chain Monte Carlo techniques for which a new flip move is developed. The numerical simulations in this work use significantly larger system sizes than studied in previous research [1, 3]. The Hausdorff dimension, which describes the dimension and the string susceptibility which describes the spikiness of the 2DQG surfaces were measured as a function of q. The new numerical evidence between $0.2 < q < 2$ supports the predictions made by Di Francesco et al., however the transition to branched polymers for $q > 2$ is smooth instead of sharp which could be due to discretization effects.

Contents

CHAPTER 1

Introduction

Figure 1.1: *Google Earth image of the river Arno in Pisa.*

A meander is typically a river that zigzags through some landscape like in Figure 1.1. Meanders are also a combinatorial problem or statistical system. A question one might ask: how many unique loops can you make using the four bridges in Figure 1.1? You are only allowed to pass every bridge once. This seemingly simple question can only be solved by counting all the possible combinations. It has not (yet) been solved exactly [2]. That is fascinating for a simple problem like this. The loop and the river in Figure 1.1 are drawn more structured in Figure 1.2.

Meanders as a toy model of two-dimensional quantum gravity is quite an abstract title. In the 90s Francesco et al. conjectured that Meanders are a model of two-dimensional quantum gravity (2DQG). How can one see this intuitively? Quantum gravity aims to unify quantum mechanics and general relativity. General relativity is a theory of geometry and quantum mechanics is a theory of probability and integrals over all possibilities. Analytically the combination of these theories is quite complex. So one way of studying the combination of them is by random geometry which is discrete and easier to study. Taking quadrangles as a building block

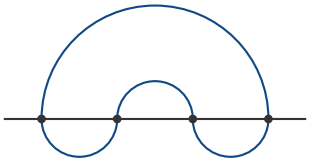

Figure 1.2: *Example of a meander of order 2, which has 4 bridges. The horizontal line is the river and the loop is the road.*

and glueing them together based on a meander gives a geometry. Taking the continuum limit of that surface is conjectured to be 2DQG. The continuum limit is taking the size of the building blocks to zero and taking the number of building blocks to infinity. One can also say, the continuum limit of random geometry decorated by meander is conjectured to be 2DQG. 2DQG is a toy model of quantum gravity that allows for studying quantum gravity in a more simple manner. But why would physics want to have a theory of quantum gravity?

In the 17th century, Isaac Newton transformed the way we think of gravity through his theory of Newtonian gravity. Newtonian gravity gave accurate predictions of the orbits of planets. At the beginning of the 19th century, Maxwell and Lorentz unified electricity and magnetism into Electromagnetism. In the 20th century, Albert Einstein was intrigued by the principle of relativity, which means that physical laws are the same in any inertial frame. Einstein thought that it was no coincidence to find the principle of relativity in both electromagnetism and classical mechanics. Based on the Michelson-Morley experiment, which proved that there is no ether, Einstein came up with the theory of special relativity [4]. Later, he generalised special relativity into general relativity by also considering accelerating inertial frames. General relativity predicts phenomena like the bending of light around the sun and gravitational waves [5]. The big difference is that special relativity and general relativity treat the 3-space dimensions on the same footing as the time dimension.

In the 20th century, another advancement was made in the field of quantum mechanics. Quantum mechanics is about the microscopic interactions between particles. A major takeaway is the wave-particle duality: particles can be considered as waves or particles. Applying quantum mechanics to fields led to the quantum field theories known as the standard model, which describes the electromagnetic, strong and weak interaction, as well as matter [6].

We know that matter described by the standard model also curves spacetime, therefore one would like to describe general relativity and quantum mechanics in a common framework, called quantum gravity (QG) [7]. There are however more reasons for wanting quantum gravity. In the singularity of a black hole, general relativity breaks down [8] which is an example that the current theoretical knowledge is lacking.

Setting up quantum gravity turns out to be quite hard analytically. One of the issues is, that gravity is perturbatively non-renormalisable. Perturbatively non-renormalisable means that there is a maximum energy up to which a perturbative theory is valid [7]. So in the ideal case, you would want to research quantum gravity non-perturbatively. Studying quantum gravity non-perturbatively can be done using dynamical triangulations for 2D, and causal dynamical triangulations (CDT) for 4D. Dynamical triangulations (DT) are a form of random geometry. Dynamical triangulations are originally inspired by how QCD is studied. QCD can be studied using Monte Carlo simulations after a lattice regularization which is discretizing the problem onto a finite lattice [6]. When studying quantum gravity using DT or CDT, the problem is not only put on a finite lattice but also the lattice itself becomes variable.

2DQG is the continuum limit of random geometry and more precisely the continuum limit of discrete random surfaces of the 2-sphere. 2DQG aims to extend Feynman's path integral to surfaces [9]. These random surfaces

have fractal properties. Matter can be introduced to 2DQG by coupling it to a certain critical statistical system. Meanders are such a critical statistical system. Therefore, meanders can be seen as matter coupled to 2DQG. One of the main things studied in 2DQG is how the critical exponents of 2DQG react to coupling to matter. A critical exponent is an observable that describes for example the dimension of a surface.

As mentioned earlier the meanders can be described as a statistical system coupled to 2DQG. In the 90s Di Francesco et al. conjectured the critical exponents of the statistical system coupled to 2DQG. This thesis will be about checking the predicted critical exponents using numerical simulations of discrete random surfaces decorated with meanders. So far, previous research has only studied the predictions of the conjecture for small systems, using a developed flip move for Markov chain Monte Carlo simulations larger systems can be studied.

The conjectured critical exponents also make predictions about the asymptotic of the question asked in the beginning: how many unique loops can you make using n bridges? This is why it can also be said that meanders are governed by matter coupled to 2DQG. The numerical simulations in this thesis will therefore also somewhat contribute to the combinatorial meander problem.

In chapter 2, the theoretical background for understanding meanders and 2DQG is described. Also, the conjectures of Di Francesco et al. are described there in detail. In chapter 3, the methods for studying meanders as a statistical system coupled to 2DQG are described, like the Markov chain Monte Carlo techniques. The research question is introduced more formally in chapter 4, in chapter 5 the results are presented and lastly in chapter 6 the results are concluded and discussed.

CHAPTER 2

Theoretical background

In this theoretical background, meanders and meander systems will be introduced formally in section 2.1. In the introduction, it was already mentioned that 2DQG is the continuum limit of random surfaces. Random planar maps are a way to study discrete random surfaces which will be introduced in section 2.2. It was also mentioned that matter fields in 2DQG are conformal field theories which will be introduced in section 2.3. These conformal field theories and 2DQG have scale-invariant properties which will be discussed in section 2.4. Lastly, 2DQG and observables in 2DQG will be introduced in section 2.5.

2.1 Meanders

Meanders can be regarded as a road and a river that cross each other at $2n$ points (bridges) or more generally speaking: two crossing self-avoiding loops. Meanders have several applications like the combinatorics of folding polymer chains [2].

For the number of meander configurations no exact formula has been found so far. However, in the 90s Di Francesco et al. conjectured that meanders are governed by the gravitational version of a two-dimensional conformal field theory with a central charge of -4. The critical exponents that can be extracted from this conjecture, allows to approximate the number of meander configurations at large system size n.

2.1.1 Meanders as a combinatorial problem

A meander is a closed self-avoiding road that intersects an infinite line (river) $2n$ times [2].

M_n denotes the number of unique meanders (inequivalent meanders) with a fixed number of bridges. Next to meanders there are meander systems that allow for more than one closed-road. A meander system is defined by having one infinite river and multiple self-avoiding closed roads. M_n^k denotes the number of inequivalent meander systems of order n with k non-intersecting closed loops. Meanders and meander systems are con-

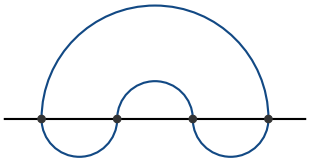

Figure 2.1: *Example of a meander of order 2, which has 4 bridges.*

sidered inequivalent when there is no smooth way of deforming them into each other without changing the order of the bridges [10].

Meander systems are easier to work with than pure meanders, since some of their properties can be calculated analytically using combinatorics. Later, some of these analytic properties will be used to check simulation results. Meanders with just one road is such a specific case, that the name meander will often be used for the more general meander systems.

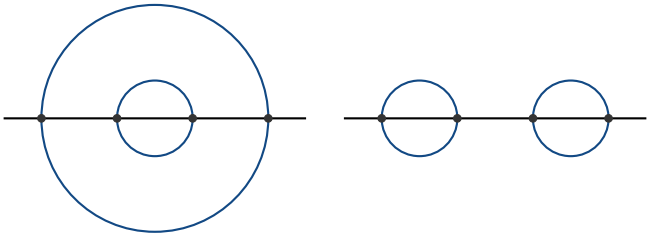

Figure 2.2: *Meander that is symmetric with respect to the river (horizontal line). One can calculate* $M_2^{(2)} = c_2 = 2$ *by Equation* (2.1).

Some meander systems can be seen as arches that can be reflected in the river, see Figure 2.2. For these types of configurations the number of meander systems is given by

$$M_n^{(n)} = c_n = \frac{1}{n+1}\binom{2n}{n} \tag{2.1}$$

where c_n is n^{th} Catalan number [10].

The total number of inequivalent meander systems can also be calculated taking the product of two arch configuration of size n:

$$\sum_{k=1}^{n} M_n^{(k)} = (c_n)^2 \tag{2.2}$$

since the number of arch configuration is counted by the Catalan numbers.

2.2 Graphs and planar maps

Maps are a way to describe discrete surfaces. There are several ways to define maps (and the following are not all): as the embedding of a graph on a surface, as the glueing of polygons or as permutations. In the following, a few of the definitions for maps and other preliminaries will be introduced. The introduction is based on Guillaume Chapuy's lecture notes "An introduction to map enumeration" [11] and "Peeling random planar maps" by Nicolas Curien.

Let's start with surfaces. A surface $\mathbb{S}$ is homeomorphic (*bijective image*) to the sphere with g handles (holes), where g is the genus [11]. An example of a genus 1 surface is a donut and an example of a genus 0 surface is the 2-sphere. All surfaces in this work will have genus 0, and therefore the surfaces associated will be the 2-sphere $\mathbb{S}$, like in Figure 2.3.

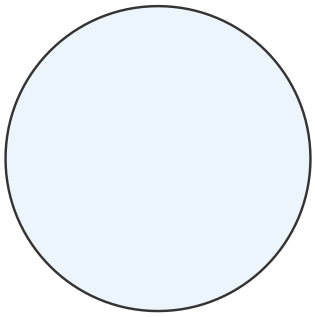

Figure 2.3: $\mathbb{S}_0$ *surface*

Secondly, a graph G is defined as a structure consisting of vertices V, edges E and faces F, where each edge consist of two half-edges [12]. The half-edges can also be called oriented edges because they point in opposite direction, see Figure 2.4. Two half-edges that form an edge are defined as each other's adjacent.

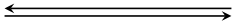

Figure 2.4: *Edge consisting of two oppositely oriented half-edges.*

The degree of a face is defined as the number of incident half-edges [12]. A face of degree of 4 is called a quadrangle. The degree of a vertex is defined as the number of incoming half-edges.

The different definitions of a map

A map, **m** can be defined as the embedding of a graph, G, into a surface $\mathbb{S}$. The **embedding** refers to drawing the graph in such a way on the surface $\mathbb{S}$ that the edges do not cross. In Figure 2.5, a planar map is drawn. A **planar map** is defined as a map of genus 0 [11]. For the embedding onto the plane, the planar map had to be rooted. Rooted planar maps have a root edge and root face. In Figure 2.5, the root edge is represented using the arrow and the root face is the white area right of the root edge. The root face is sent to infinity to draw this planar map on a plane [11].

Maps can also be seen as the glueing of polygons. In Figure 2.6, quadrangles are glued together along their edges. The quadrangles are glued together along their edges such that the half-edges are oriented in opposite direction. The result is a quadrangulation which is defined as a map with faces of degree 4.

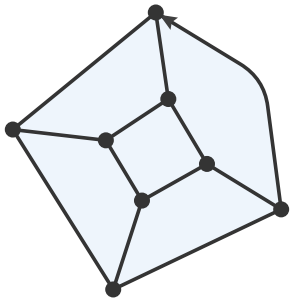

Figure 2.5: *Embedding of a planar map into a flat plane with a root edge, denoted by the edge with the arrow. The face right of the root edge is the root face. The root face is the white region, thus the page is also a face.*

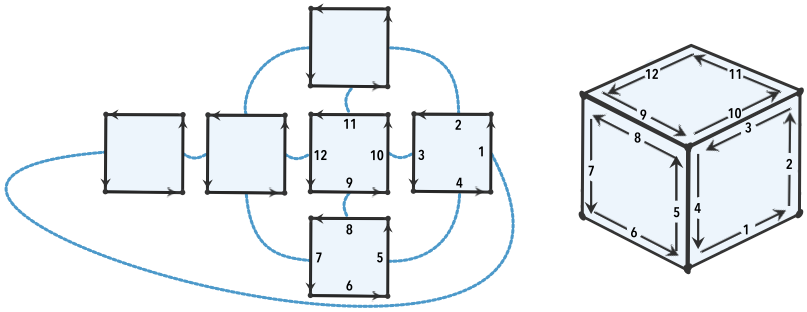

Figure 2.6: *Quadrangles are being glued into a cube.*

Lastly, maps can also be described using **permutations** [13]. There can be cycles n that represent the faces and cycles a that represent the adjacent edges. The cycles n encode what is the 'next' half-edge on a face. For example 2 is the next half-edge with respect to 1 in Figure 2.6. Here the cycles for the glued cube in Figure 2.6 are given by

$$a = (4\,5)(10\,3)(8\,9)\cdots \tag{2.3}$$

$$n = (1\,2\,3\,4)(5\,6\,7\,8)(9\,10\,11\,12)\cdots \tag{2.4}$$

Additional preliminaries

The **dual** map is defined as the map build out of the vertices on every face of the original map and links the new vertices together by making new edges perpendicular to the original edges. **Duality** changes faces into vertices and vertices into faces [11]. The idea of a dual map is sketched in blue in Figure 2.7.

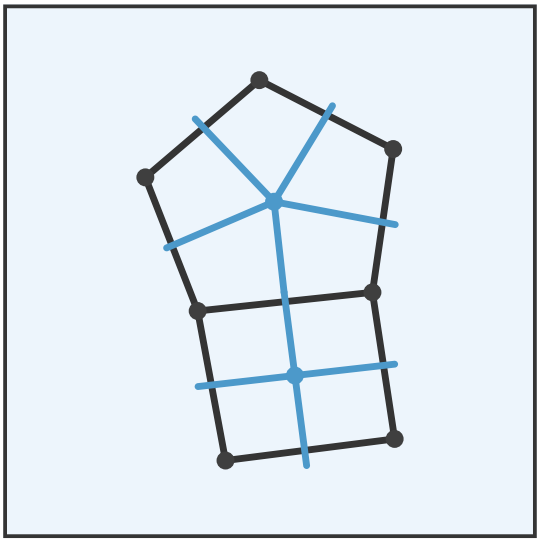

Figure 2.7: *The dual map is represented with the blue edges and blue vertices.*

A graph is defined to be **bipartite** when the vertices can be divided into two subsets of **black** and **white** vertices where every edge connects a white and black vertex [14, 15]. This also means that the graph is **bicolorable**.

2.3 Conformal field theory

Conformal field theories don't care about distances, but only angles. Conformal field theories (CFTs) are quantum field theories that are invariant under conformal transformations. The property of these conformal transformations is that they conserve the angles between vectors [16, 17]. A more formal way to describe a conformal transformation is by considering this change of coordinates: $x^\alpha \to \tilde{x}^\alpha(x)$. Under a conformal transformation the metric changes by

$$\tilde{g}_{\alpha\beta}(x) = \Omega^2(x) g_{\alpha\beta}(x) \tag{2.5}$$

where $\Omega^2(x)$ is an arbitrary non-vanishing function of coordinates x^α [16, 17].

An operator for CFTs is the central charge, c. The central charge is a measure for the number of degrees of freedom in a CFT and therefore an important and useful property of a CFT [17]. One example of a CFT is the free scalar field. The free scalar field has a central charge, $c = 1$. N non-interacting free scalar fields will give $c = N$ [17].

2.4 Universality

Scale-invariance has a central position in physics. One example of scale-invariance in physics are conformal field theories discussed in section 2.3.

In the theory of phase transitions there are so-called critical exponents, these exponents are observables that qualitatively describe the critical behavior of a system near a phase transition [18]. It turns out that these critical exponents are often not fully independent of each other. The critical exponents may depend on only a few characteristics of a certain system. Characteristics may be microscopic or macroscopic [18]. A critical exponent that depends just on a few characteristics results in different systems having the same critical exponents. Systems that display the same critical behavior, thus have similar critical exponents, are said to be in the same **universality class**.

An explanation for the origin of the universality classes is found when considering correlations on a microscopic level. If the correlations are large enough to influence macroscopic properties then local/microscopic details are irrelevant [18]. So when one changes a microscopic detail of a system to get a new system, but the macroscopic properties do not change, then the two systems are in the same universality class. Even tough they are different on a microscopic scale. If a change in microscopic details does change the macroscopic properties then the new system is in a different universality class [19].

In figure 2.8 some plots can be seen of discrete surfaces of different sizes where the macroscopic characteristics match for 2.8a, 2.8b and 2.8c and for 2.8d, 2.8e and 2.8f. It is clear that 2.8d, 2.8e and 2.8f show a branched structure. It can be said that these surfaces are in the branched polymer universality class. The surfaces of 2.8a, 2.8b and 2.8c look smooth instead and are in a different universality class.

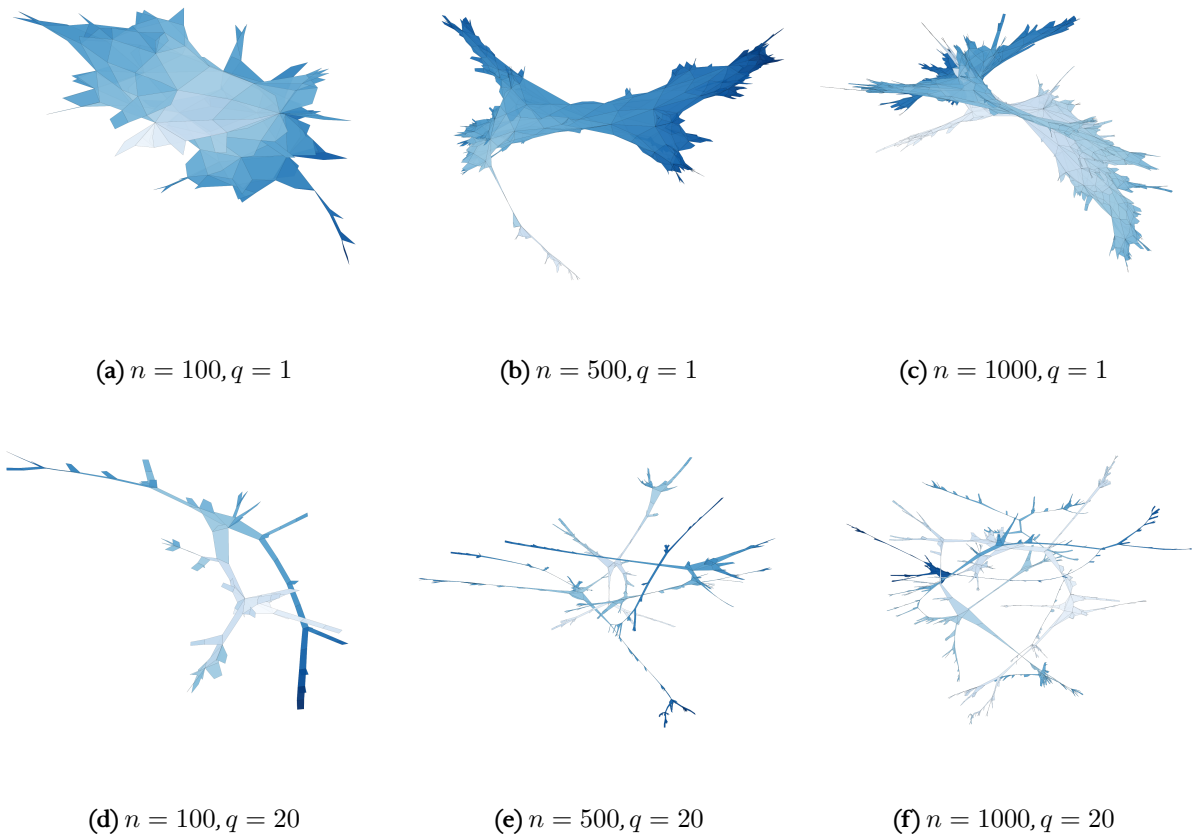

(a) $n = 100, q = 1$ (b) $n = 500, q = 1$ (c) $n = 1000, q = 1$

(d) $n = 100, q = 20$ (e) $n = 500, q = 20$ (f) $n = 1000, q = 20$

Figure 2.8: *3D visualisation surfaces of the 2-sphere using a spring layout embedding. Geometries (a), (b) and (c) correspond to two-dimensional quantum gravity to a conformal field theory with a central charge of -2 and the continuum limit of spanning tree decorated quadrangulations. Geometries (d), (e) and (f) show 'branched polymer' behavior.*

2.5 Two-dimensional quantum gravity

Two-dimensional quantum gravity can be defined via two routes: via the scaling limit of discrete random geometries or via Liouville quantum gravity [20]. The two routes both try to solve performing the path integral over metrics on a surface. Two-dimensional quantum gravity as the scaling limit of discrete random geometries originates from doing a lattice discretization to solve the path-integral [20]. In the lattice discretization also the lattice itself is variable which is why planar maps are used. Liouville quantum gravity can be seen as an analytic interpretation of two-dimensional quantum gravity, and it is conjectured to be the scaling limit of discrete random geometries [21].

Two-dimensional quantum gravity without matter is called 'pure gravity' which is a universality class with certain critical exponents. Matter can be introduced in two-dimensional quantum gravity by dressing/coupling the geometry to a critical statistical system with a certain central charge [20]. The coupling changes the critical exponents and thus allows for discovering other universality classes. **Note that the statistical system is the matter field, so the matter is quite abstract** [22].

Liouville quantum gravity is characterized by its coupling constant γ. The 'pure gravity' universality class corresponds to the coupling constant $\gamma = \sqrt{8/3}$ [20, 21]. (Undecorated) uniform quadrangulations in the continuum limit are an example of 'pure gravity'. Adding matter fields changes the coupling constant, γ, of Liouville quantum gravity.

Two-dimensional quantum gravity will be coupled to meanders. Specifically, quadrangulations will be decorated by meanders which will change the universality class of the system. Critical exponents can then be measured to find out the universality class of those systems. These critical exponents which are observables will be described in the following section. Also, the KPZ formula will be introduced which describes the critical exponents when a statistical system with a certain central charge is coupled to 2DQG.

Actually, the quadrangulations will be built based on meander configurations. It is a common thing in 2DQG to build discrete surfaces based on a statistical system. In [22] by Budd and Castro, random surfaces are for example built by knitting trees which also allows creating random surfaces of a certain universality class.

2.5.1 Observables

The critical exponents are observables of 2DQG. Two critical exponents that will be considered are the Hausdorff dimension and the string susceptibility. The Hausdorff dimension describes how geodesic distances grow on a surface and the string susceptibility describes the roughness or spikiness of a geometry.

String susceptibility

The string susceptibility measures the fractal structure of two-dimensional quantum gravity (2DQG). It quantifies the roughness of a surface [23, 24]. The method to find the string susceptibility is by taking a discrete surface and counting the number of spikes of a certain size, more formally called the number of baby universes.

A baby universe is like a balloon on a surface connected through a minimal neck, like in Figure 2.9. The minimal neck is the smallest possible loop in a geometry. More formally, a baby universe is defined as a simply connected area whose boundary length is much smaller than the square root of its area [24]. The area of the baby universe can be denoted by n and the area of the total geometry by N. The area n of a baby universe

must satisfy $n < N/2$.

In the case of quadrangulations the smallest loop or **minimum** neck is equal to 2 and in the case of triangulations the smallest loop is equal to 3. A baby universe connected through a minimum neck is called a **mimbu** short for 'minimum neck baby universe' [24].

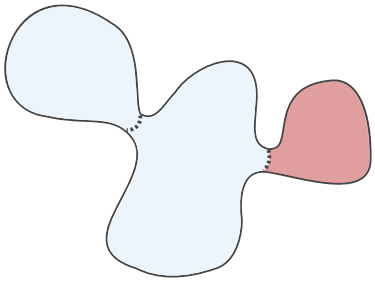

Figure 2.9: *Sketch of a geometry with 2 minimal necks indicated by the dashed lines. For the rightmost minimal neck, the baby universe is indicated in red.*

An interesting measure to look at, is the distribution describing mimbu's of size n. When the genus is set to zero, $g = 0$, the partition function of random surfaces in two-dimensional quantum gravity generally grows asymptotically with N as

$$Z(N) \approx e^{\mu_c N} N^{\gamma_s - 3} \tag{2.6}$$

where γ_s is the string susceptibility. Using this partition function one can approximate the probability for a **mimbu** of size n on a geometry of size N, given by

$$p \approx \frac{nZ(n)(N-n)Z(N-n)}{NZ(N)} = (n \cdot (1 - n/N))^{\gamma_s - 2} \tag{2.7}$$

For calculating the probability of a **mimbu** of size n on a geometry of size N, it is used that a geometry of size N will be made out of a geometry of size n and a geometry of size $N - n$.

From equation (2.7) one can see that the string susceptibility is easily retrieved by measuring p and then performing regression on $\ln p$ versus $\ln(n \cdot (1 - n/N))$. The slope should then measure $\gamma_s - 2$.

Hausdorff dimension

Hausdorff dimension, d_H is a critical exponent which describes the dimension of a geometry. For flat geometry $\mathbb{R}^d$, the dimension d is equal to d_H [25]. For self-similar, fractal geometry the Hausdorff dimension is less trivial. One way to define the Hausdorff dimension is by the scaling of the number of vertices in a geodesic ball of size r where

$$V \sim r^{d_H} \tag{2.8}$$

for the number of edges $n \to \infty$. The number of vertices on a surface of a geodesic ball grows then like $r^{d_H - 1}$ for $n \to \infty$ [26].

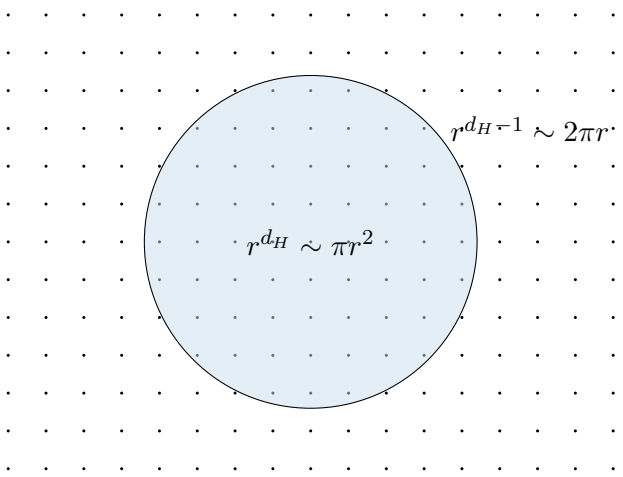

Figure 2.10: $\mathbb{R}^2$ *surface with a circle of area* $r^{d_H} \sim \pi r^2$ *and the number of vertices at the distance* r *is equal to* $r^{d_H-1} \sim 2\pi r$.

A trivial example is the Hausdorff dimension of a circle, see Figure 2.10. The area of the circle πr^2 which should be proportional to the number of dots (vertices) in the circle. Comparing this to equation (2.8) yields a Hausdorff dimension of $d_H = 2$. The same can be concluded when counting the number of vertices at the border of the circle which scales like $2\pi r$ and thus also yields a Hausdorff dimension of 2.

The Hausdorff dimension can be measured using the relations for the number of vertices at a distance r. It will however be difficult to measure accurately because it is only valid when $1 \ll r \ll N^{1/d_H}$ and would thus require huge system sizes [13]. A way to get around that is by using finite size scaling which allows to measure the Hausdorff dimension accurately [13]. The idea of finite size scaling is to rescale the distance profiles in Figure 2.11 such that they overlap. Finite size scaling will be more practically introduced in section 5.3.2.

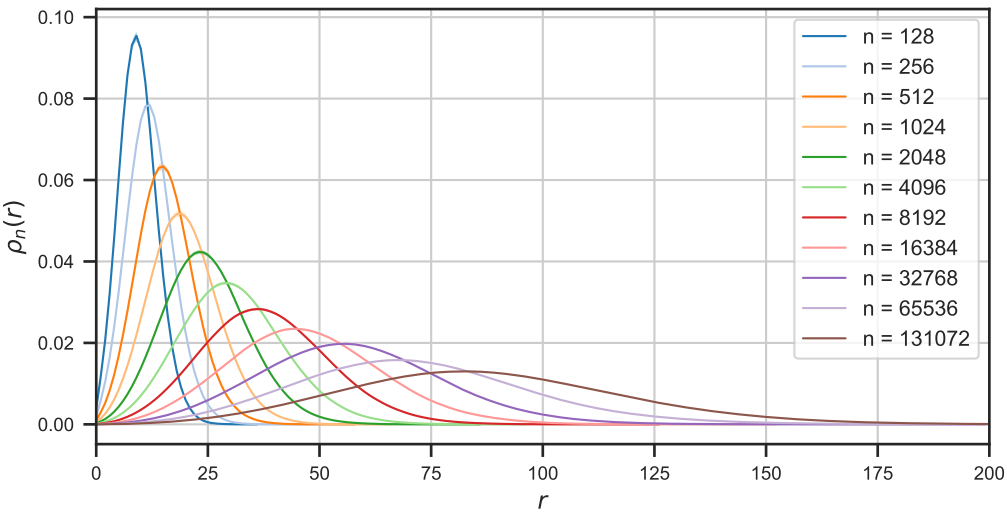

Figure 2.11: *Histogram of* $\rho_n(r)$ *of meander decorated geometries with* $q = 1$.

2.5.2 Relation string susceptibility, Hausdorff dimension and central charge

As mentioned earlier, the critical exponents of two-dimensional quantum gravity change when coupled to a critical statistical system with a certain central charge c. Here the relations between the central charge, Liouville coupling constant γ, string susceptibility and Hausdorff dimension will be given.

Central to studying the critical behaviour of statistical systems is the KPZ formula founded in the 80s by Knizhnik, Polyakov and Zamolodchikov [9]. The KPZ formula tells how the critical exponents of the original statistical system on a flat, regular (Euclidean) system are related to the critical exponents of the statistical system coupled to 2DQG [9]. Coupling the statistical system to 2DQG can be seen as studying the statistical system on a random planar lattice [9]. The KPZ formula is a widely used application of Liouville Quantum Gravity [21]. It is however a conjecture and not rigorously proven [9]. More details about the KPZ formula can be read in [9] by Christophe Garban.

Using the KPZ formula, the string susceptibility γ_s can be related to the central charge of the statistical system by

$$\gamma_s = \frac{c - 1 - \sqrt{(c-1)(c-25)}}{12} \tag{2.9}$$

which is valid for $c \in (-\infty, 1]$ [20].

The coupling constant $\gamma \in (0, 2]$ of Liouville quantum gravity is related to the central charge by

$$c = 25 - 6\left(\frac{2}{\gamma} + \frac{\gamma}{2}\right)^2 \tag{2.10}$$

where again $c \in (-\infty, 1]$ [20]. The string susceptibility γ_s is related to the Liouville coupling constant γ by

$$\gamma_s = 1 - \frac{4}{\gamma^2} \tag{2.11}$$

One of the challenges in the field is obtaining a relation between the Liouville coupling constant γ and the Hausdorff dimension. In [20] Barkley and Budd did numerical research into the relation. Numerical evidence and earlier derived bounds supports

$$d_H = 2 + \frac{\gamma^2}{2} + \frac{\gamma}{\sqrt{6}} \tag{2.12}$$

proposed by Ding and Gwynne in [27]. Liouville quantum gravity only describes the coupling of a statistical system to random geometry for $c \in (-\infty, 1]$ [20] instead of the older Watabiki formula [20]. There is the $c = 1$-barrier beyond which the random geometries degenerate into branched polymers, like in Figures 2.8d, 2.8e and 2.8f. This branched polymer phase (shaded in light blue in Figure 2.12) for $c > 1$ is characterized by Hausdorff dimension $d_H = 2$ and string susceptibility $\gamma_s = \frac{1}{2}$ [25]. It is interesting to note that $d_H = 2$ would suggest flat geometry, although branched polymers are not flat geometry [28]. The string susceptibility γ_s and the Hausdorff dimension d_H are plotted as a function of the central charge c in Figure 2.12.

For $c = 0$, there is the 'pure gravity' universality class with the Liouville coupling constant $\gamma = \sqrt{8/3}, \gamma_s = -\frac{1}{2}$ and $d_H = 4$ [20, 21]. A Hausdorff dimension of 4 is quite high, usual surfaces have a fractal dimension of 2, so 'pure gravity' is very fractal [29]. $c = -2$ corresponds to the universality class of quadrangulations decorated by a spanning tree [20].

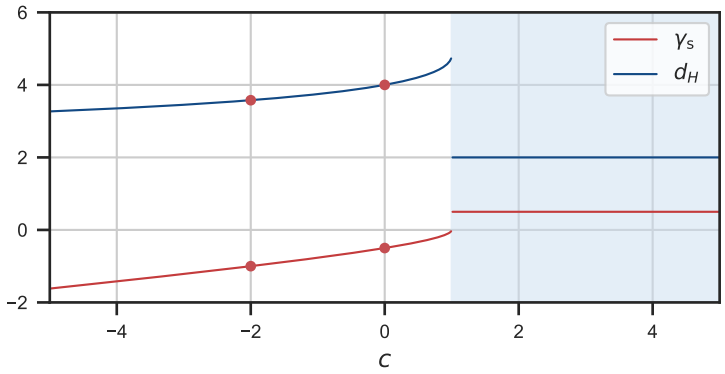

Figure 2.12: *The string susceptibility γ_s and the Hausdorff dimension d_H as a function of the central charge c of the coupled statistical system are plotted. The highlighted red dots indicate at $c = 0$ 'pure gravity' and at $c = -2$ the spanning tree decorated quadrangulations universality class. The branched polymer phase, $c > 1$, is shaded in light blue. For the Hausdorff dimension equations (2.12), (2.11) and (2.10) were used and for the string susceptibility equation (2.10).*

Being able to sample large and independent random surfaces of a certain universality class can help to collect numerical data on the relation between the Hausdorff dimension and the Liouville coupling constant γ. Meanders are a statistical system that could possibly to collect numerical data of that relation.

2.6 Meanders as a conformal field theory coupled to two-dimensional quantum gravity

Matter can be introduced to 2DQG by coupling 2DQG to a statistical system, like meanders. Meanders are conjectured to be a conformal field theory coupled to two-dimensional quantum gravity (2DQG). Di Francesco et al. introduced this conjecture in [2] and later numerical evidence and theoretical arguments were put forward in references [1, 3]. The basic idea is that the meanders can be seen as two fully-packed loops on a random geometry. In the continuum limit, these fully-packed loop models are described by a conformal field theory. In the following section, the background of meanders as a CFT coupled to 2DQG will be discussed. The goal is to explain how the central charge of that CFT is derived by Di Francesco et al. Using the KPZ formula introduced in section 2.5.2, the central charge can be used to predict the critical exponents of meanders coupled to 2DQG.

First, fully-packed loop models on a regular lattice will be introduced in section 2.6.1, then in section 2.6.3, the two fully-packed loop models will be coupled to 2DQG, which will then be called GFPL^2 model. The two fully-packed loop models are denoted by the FPL^2 model. By taking the limits of parameters of the fully-packed loop model coupled to 2DQG, one can recover meanders and meanders systems. These steps are also displayed in Figure 2.13.

The intuitive idea of the following section is that the central charge is an indication for the number of degrees of freedom. The type of lattice and the properties of meanders influence the number of degrees of freedom and therefore the central charge. Coupling to 2DQG is a change of lattice for the CFT that was first defined on a regular lattice. Studying a theory in its gravity-form is studying it on a random lattice instead of a regular lattice.

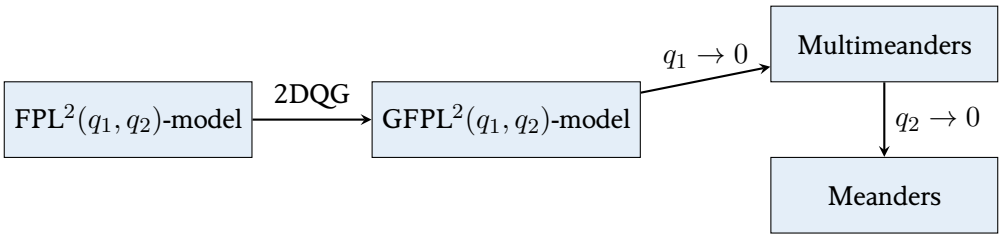

Figure 2.13: *Steps to relate* FPL^2*-model to meanders. The* FPL^2*-model can be transformed into the* GFPL^2*-model by coupling the model to two-dimensional quantum gravity. The coupling is realised by replacing the square lattice of the* FPL^2*-model with random quadrangulations of the 2-sphere. The* GFPL^2*-model can again be related to meanders and meander systems by taking the parameter* $q_1 \to 0$ *and* $q_2 \to 0$.

2.6.1 Fully-packed loop models

The connection of meanders to two-dimensional quantum gravity starts by discussing fully-packed loop models. **Fully-packed** means that every vertex is visited. In the case of fully-packed loop models, all vertices are visited by a self-avoiding random walk exactly once [30, 31]. Here fully packed loop models will be studied on a square lattice which can be seen in Figure 2.14a. The procedure described here is based on the work of Jacobsen and Kondev and Di Francesco et al. [1, 30].

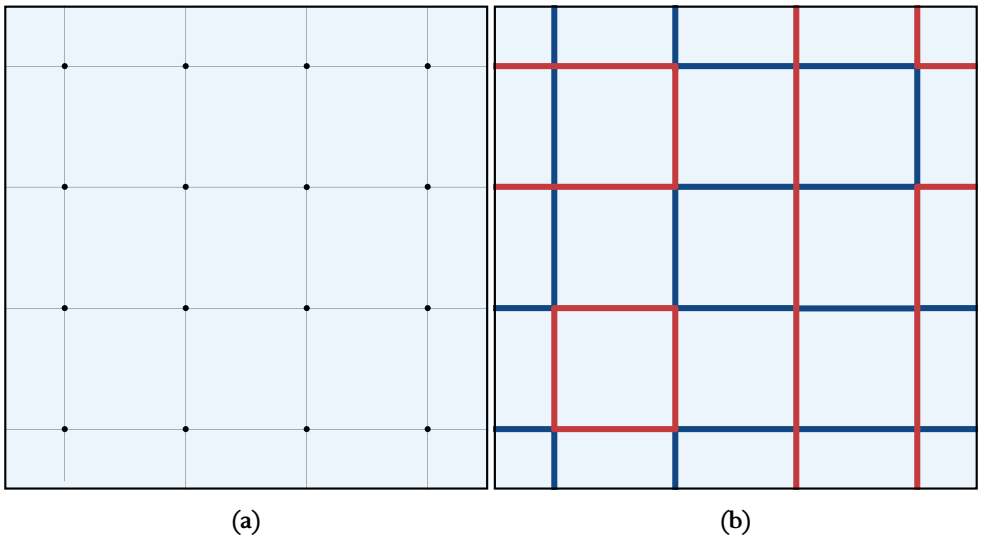

Figure 2.14: *(a) Square lattice (b)* FPL^2*-model short for two-flavored fully packed loop model. The red loops refer to roads and the blue loops refer to the rivers.* ***Note****: the lattices have periodic boundary conditions in up/down and left/right directions.*

Figure 2.15: *Vertices of the fully-packed loop model, (a) "crossing" vertex and (b) "avoiding" vertex.*

Meanders have two distinct types of loops, a river and a road, in other words two flavors of loops. It is therefore natural to look at the two-flavored fully-packed loop model (FPL^2-model). The FPL^2-model can be described on a square lattice in which two loops visit every vertex once, so two **fully-packed** loop models. At every vertex the loops can avoid or cross, see the two vertex types in Figure 2.15. Moreover, two weights q_1 and q_2 are assigned to the river and the road loop respectively [32]. The model is critical for weights $0 \leq q_1, q_2 \leq 2$, within this area every point (q_1, q_2) has different universality class when coupled to 2DQG. By assigning weights to the river and road loops results in the following partition function:

$$Z_{\mathrm{FPL}^2}(q_1, q_2) = \sum_{\text{fully-packed loop configurations}} q_1^{k_1} q_2^{k_2} \tag{2.13}$$

where q_1, q_2 are interpreted as the weights assigned to rivers and roads respectively [1].

Equation (2.13) describes a more general case of meanders where the number of roads and rivers are variable. The partition function for meander systems is recovered by taking $q_1 \to 0$ which gives:

$$Z(q) = \sum_{\text{configurations}} q^k \tag{2.14}$$

where $q = q_2$ is the weight assigned to the roads and $k = k_2$ is the number of roads. From equation (2.14), the partition function of meanders is recovered by taking the limit $q \to 0$.

2.6.2 Finding the CFT describing the continuum limit of the FPL^2-model

The continuum limit of the FPL^2-model can be described by a conformally invariant effective field theory. The goal is to find the critical exponents of this conformal field theory, which can be done by describing the FPL^2-model using a height model. A height model defines a height h at each lattice site [33]. The height can be for example a scalar, but here the height will be considered a vector.

Every face in the lattice of Figure 2.14b is given a height h. In other words, the height h is assigned to vertices of the dual map of Figure 2.14b. Now one needs to come up with a set of height rules that define how the height h changes when going to a different faces (or vertices in the dual map). Firstly, the vertices of Figure 2.14a need to be bicolorable and for that the map needs to be bipartite (see section 2.2). This can be easily realized for the square lattice, since a checkerboard pattern easily allows to divide the graph up into two subsets where only vertices of a different color will neighbor each other. The bicoloring is visualised in Figure 2.16a.

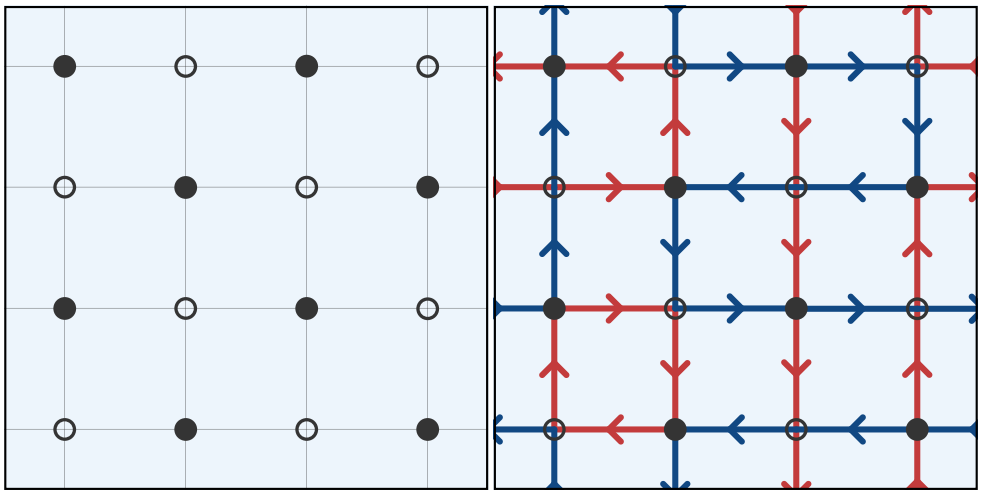

(a) (b)

Figure 2.16: *Visualisation of (a) bipartite square lattice with two vertex colors: filled ● and empty ○ (b)* FPL^2*-model with orientation of the edges indicated by the arrows and bicolored vertices. The red loops refer to roads and the blue loops refer to the rivers.* ***Note:*** *the lattices have periodic boundary conditions in up/down and left/right directions.*

Secondly, the loops can be assigned an orientation, like in Figure 2.16b. The orientation and the bicoloring

allows to define the height rules given in Figure 2.17[1].

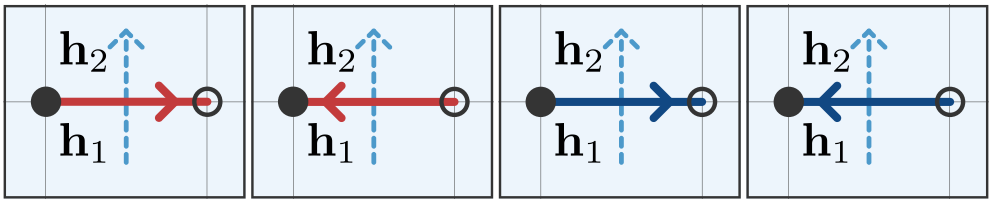

(a) $\mathbf{h}_1 - \mathbf{h}_2 = \mathbf{A}$ (b) $\mathbf{h}_1 - \mathbf{h}_2 = \mathbf{B}$ (c) $\mathbf{h}_1 - \mathbf{h}_2 = \mathbf{C}$ (d) $\mathbf{h}_1 - \mathbf{h}_2 = \mathbf{D}$

Figure 2.17: *The four height rules that determine how the height changes when going to an adjacent face by crossing one of four types of edges. The height rules are drawn as crops of a square lattice with one type of edge.* $\mathbf{h}_1$ *is the vector-height associated with the face below the edge and* $\mathbf{h}_2$ *with the face above the edge.*

The height rules have to be well-defined. In other words, when one makes a **closed** walk, there should be no net height change. Making a simple walk around a vertex like in Figure 2.18 results in the following condition on the height values:

$$\mathbf{A} + \mathbf{B} + \mathbf{C} + \mathbf{D} = 0 \tag{2.15}$$

which can de derived by applying the height rules defined in Figure 2.16. The procedure is simple, by starting at $\mathbf{h}_1$ one gets $\mathbf{h}_2 = \mathbf{h}_1 - \mathbf{D}, \mathbf{h}_3 = \mathbf{h}_1 - \mathbf{D} - \mathbf{A}, \mathbf{h}_4 = \mathbf{h}_1 - \mathbf{D} - \mathbf{A} - \mathbf{B}, \mathbf{h}_1 = \mathbf{h}_1 - \mathbf{D} - \mathbf{A} - \mathbf{B} - \mathbf{C}$ which ultimately results in equation 2.15.

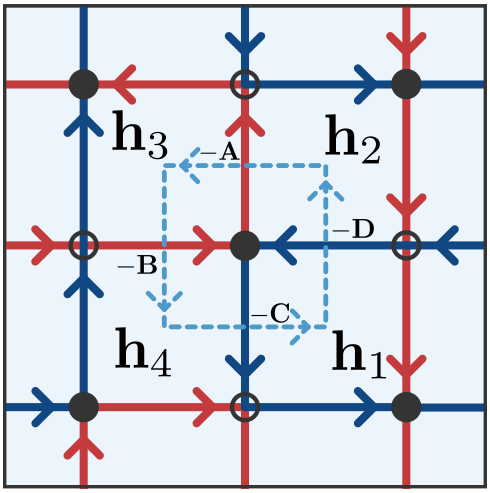

Figure 2.18: *Walking around a vertex to ensure that the height is well-defined.* $\mathbf{h}_1, \mathbf{h}_2, \mathbf{h}_3$ *and* $\mathbf{h}_4$ *indicate the height of the face and* $-\mathbf{D}, -\mathbf{A}, -\mathbf{B}$ *and* $-\mathbf{C}$ *next to the blue dashed line indicate the change of height in the direction of the arrow.*

From $\mathbf{A}+\mathbf{B}+\mathbf{C}+\mathbf{D} = 0$ can be concluded that there are 3 degrees of freedom and thus the height, $\mathbf{h} \in \mathbb{R}^3$, is a 3-vector. In the continuum limit, this height model was therefore argued to become a 3D scalar field (CFT) with the following central charge [1, 30, 34]

[1] Note that there is a certain ambiguity in choosing the height rules. The height rules are however chosen in such a way that one should get $\mathbf{A} + \mathbf{B} + \mathbf{C} + \mathbf{D} = 0$ when walking around a vertex. This is the same convention as in references [1, 2] by Di Francesco et al.

$$c = 3 - 6\left(\frac{e_1^2}{1-e_1} + \frac{e_2^2}{1-e_2}\right) \tag{2.16}$$

where e_1 and e_2 are related to q_1 and q_2 by:

$$q_i = 2\cos(\pi e_i) \tag{2.17}$$

where q_1 and q_2 are the weights assigned to the river and road respectively and e_i is constrained by $0 \leq e_i \leq 1/2$. The derivation of the central charge is rather technical and can be found in detail in [30] by Jacobsen and Kondev.

2.6.3 Coupling the FPL^2-model to gravity

Taking the limit $q_1 \to 0$ and $q_2 \to 0$ of the FPL^2-model does not give meanders [1, 3]. The correct statistical system can be retrieved by coupling the FPL^2-model to gravity, which is then called the GFPL^2-model. Coupling the FPL^2-model to gravity means that the square lattice is changed to a random planar four-valent graph, i.e. random quadrangulations. This change is not trivial, since not every planar four-valent graph is bicolorable and so the height rules must change. When the bicolorability of vertices is removed, the first two edges and last two edges in Figure 2.17 will be the same. The new height rules are given in Figure 2.19.

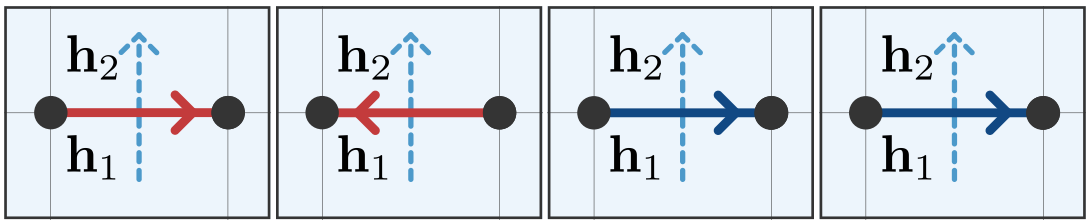

(a) $\mathbf{h}_1 - \mathbf{h}_2 = \mathbf{A}$ (b) $\mathbf{h}_1 - \mathbf{h}_2 = \mathbf{B} = -\mathbf{A}$ (c) $\mathbf{h}_1 - \mathbf{h}_2 = \mathbf{C}$ (d) $\mathbf{h}_1 - \mathbf{h}_2 = \mathbf{D} = -\mathbf{C}$

Figure 2.19: *The four height rules that determine how the height changes when going to an adjacent face by crossing one of four types of edges. Note however that there are effectively only two edge types because the vertices are not bicolored. The height rules are drawn as crops of a square lattice with one type of edge highlighted.* $\mathbf{h}_1$ *is the vector-height associated with the face below the edge and* $\mathbf{h}_2$ *with the face above the edge.*

From the height rules one can also see that the new conditions to keep the height model well-defined are $\mathbf{A} + \mathbf{B} = \mathbf{0}$ and $\mathbf{C} + \mathbf{D} = \mathbf{0}$. Now the height model has only two degrees of freedom, resulting in a central charge of

$$c = 2 - 6\left(\frac{e_1^2}{1-e_1} + \frac{e_2^2}{1-e_2}\right) \tag{2.18}$$

where one sees a $c \to c - 1$ shift with respect to the former central charge given by Equation (2.16) [1].

Losing the bicolorability means that the "avoiding" vertex in Figure 2.15b, will become irrelevant for the GFPL^2-model. It is argued in [1] by Di Francesco et al. that the disappearing of this "avoiding" vertex is not problematic. One of the reasons is that meanders with this "avoiding" vertex, called tangent meanders, have exactly the same universality class as meanders. So the "avoiding"/tangency points can just be neglected.

Now one can take $q_1 \to 0$ in Equation (2.18) to get to the case of one-infinite river, i.e. meander systems. This corresponds to $e_1 = \frac{1}{2}$ which gives

$$c = -1 - 6\left(\frac{e^2}{1-e}\right) \tag{2.19}$$

where $e_2 = e$ is substituted and $q = q_2 = 2\cos(\pi e)$ where q is the weight assigned to roads in the meander systems.

Now several remarks about meanders and multi-meander systems can be made. First, $0 \leq q \leq 2$ which translates to $c \in [-4, -1]$. A geometry decorated with a multi-meander system can therefore be tuned such that it corresponds to a CFT with a central charge $c \in [-4, -1]$ coupled to 2DQG. For the pure meander limit $q \to 0$, one finds 2DQG coupled to a CFT with central charge $c = -4$.

2.6.4 Critical exponents of meanders

Now that the central charge of the statistical system coupled to 2DQG is known, the KPZ formula can be used to extract the critical exponents. In Figure 2.20b, the critical exponents γ_s and d_H are plotted as a function of q using Equation (2.9) and Equation (2.19). Note however that those conjectured formulas are only valid up to $q = 2$. For $q > 2$, Di Francesco et al. made several predictions. For $0 \leq q \leq 2$ every point is expected to be in a different universality class. This can be clearly seen because between $0 \leq q \leq 2$ the string susceptibility and Hausdorff dimension change continuously as a function of q. This red shaded region also corresponds to the red region in Figure 2.20a with the only difference the x-axis. For $q > 2$ the model is no longer critical and corresponds to the branched polymer phase shaded in blue. At $q = 2$, a phase transition to the branched polymer phase is predicted.

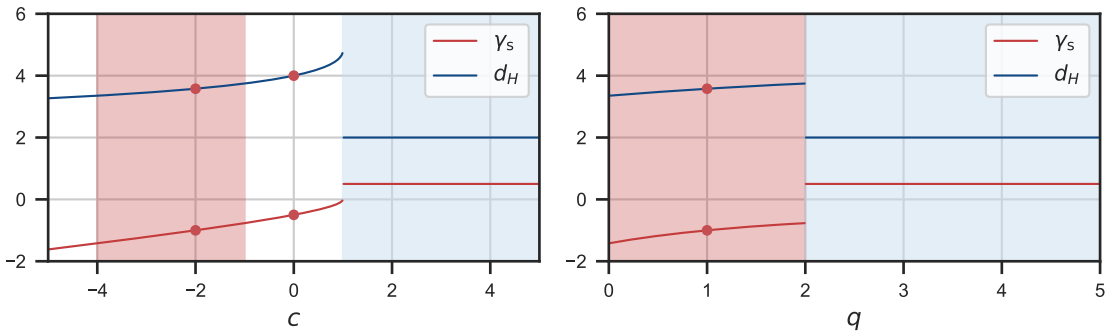

(a) (b)

Figure 2.20: *(a) Central charge of coupled system versus the string susceptibility γ_s and the Hausdorff dimension d_H. For the Hausdorff dimension equation (2.12) was used. Shaded in red are the central charges the* GFPL^2*-model can achieve by tuning the weight q. (b) The string susceptibility γ_s and the Hausdorff dimension d_H are plotted versus the weight q. The red shaded area corresponds to the same range of universality classes. The same goes for the blue area. The red dots in the red shaded region correspond to the same universality class (spanning tree) with $c = -2$ in both plots. Note that the vertical-axis is the same for both plots.*

2.6.5 Studying the GFPL^2-model

There are two non-rigorously proven steps used above. Firstly, the KPZ formula is not rigorously proven. Secondly, the connection between meanders and the fully packed loop model coupled to meanders is also not rigorously proven but made based on reasonable arguments made above and more presented in [1, 2]. A system that is similar to the GFPL$^2(q_1, q_2)$-model are random quadrangulations. In the following the connection between the GFPL$^2(q_1, q_2)$-model and random quadrangulations will be made.

The GFPL$^2(q_1, q_2)$-model can be studied using random quadrangulations [3], in the following section will be argued why this approach is correct. Firstly, one takes a square lattice and four-colors $(1, 2, 3, 4)$ all the vertices, like in Figure 2.21a. The square lattice here is also face bicolorable. On this lattice, the height rules of Figure 2.21b can be chosen and for a consistent height model $\mathbf{A} = -\mathbf{B}$ and $\mathbf{C} = -\mathbf{D}$. This change of height is equivalent to the GFPL$^2(q_1, q_2)$-model [3].

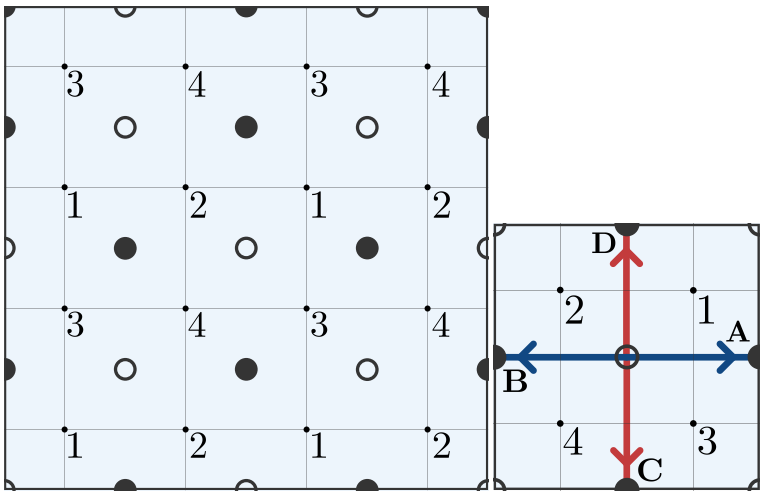

Figure 2.21: *(a) Quadrangulations of which the vertices are four-colored and the faces bicolored. (b) Height rules*

As seen in section 2.2, maps can be built by glueing polygons. Here a quadrangle with the "avoiding" vertex in Figure 2.22 is taken as the polygon/building block. The horizontal half-edges in Figure 2.22 are called the shore half-edges because the road indicated with the red dashed line crosses them.

Glueing rivers to rivers results in a row of quadrangles and then one can glue the roads based on a certain meander configuration resulting in a quadrangulation, see Figure 2.23a. Embedding the system on a flat plane then results in Figure 2.23b.

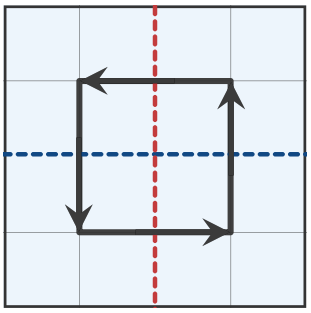

Figure 2.22: *The building block for building a quadrangulations of the 2-sphere. Road indicated by the red dashed line and the river indicated by the blue dashed line.*

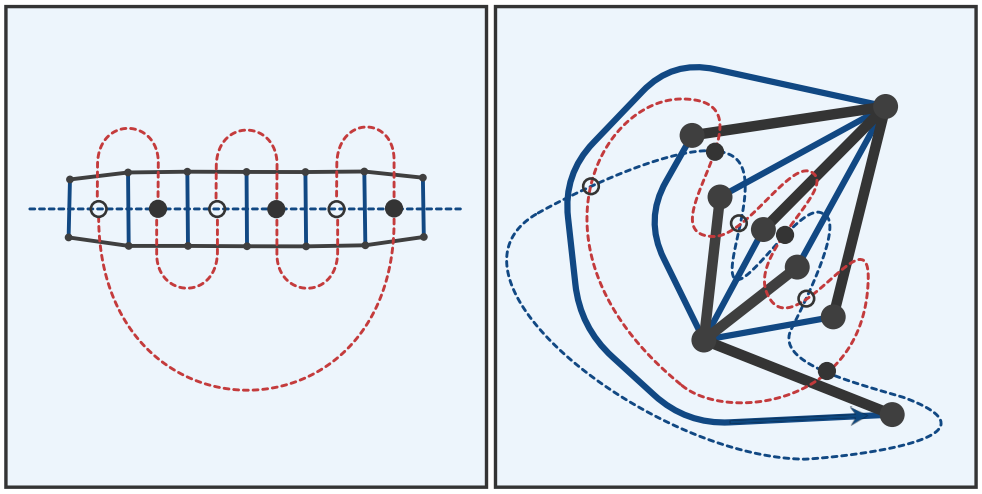

(a) (b)

Figure 2.23: *(a) Drawing of a quadrangulation based on a meander configuration. (b) Embedding of the quadrangulation of Figure a on the flat plane.*

2.7 Predicting the string susceptibility for multi-meanders

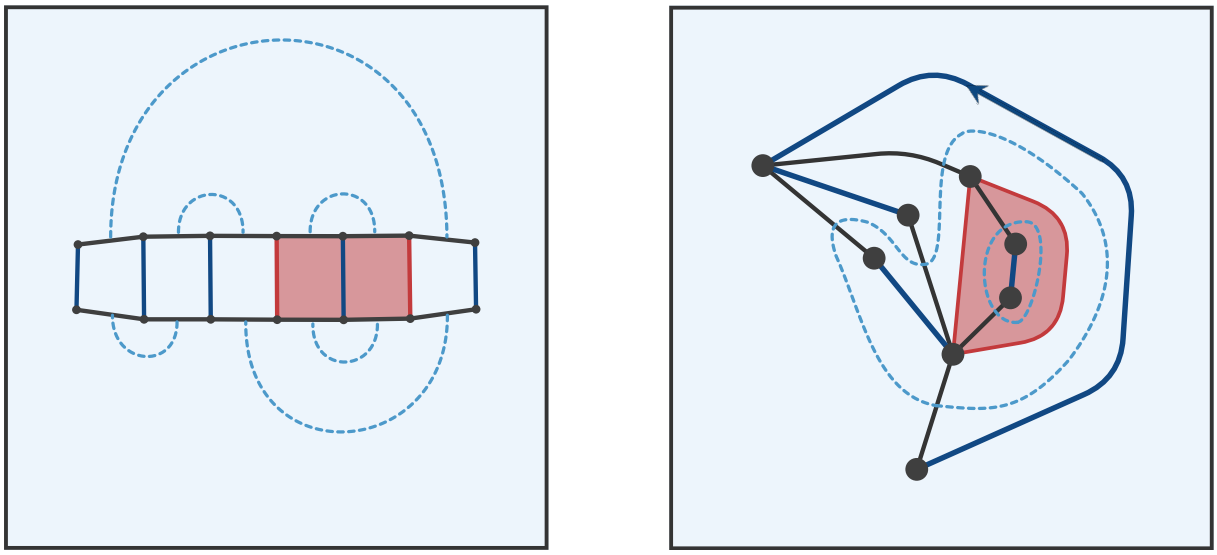

(a) (b)

Figure 2.24: *(a) Sketch of how quadrangles can be glued into a geometry using a meander configuration as the glue rule. The baby universe/mimbu is indicated in red. (b) 2D representation of the planar map of the geometry. Here it is clear that the faces painted red are only connected to the rest of the geometry through a minimum neck of size* 2*. The minimum neck is indicated by the red edges. The root edge is indicated by the arrow and the root face is the face right of the root edge.*

In section 2.5.1, the string susceptibility was introduced which measures the roughness of a surface. A **mimbu** corresponded to a minimum neck baby universe, i.e. a piece of the geometry only connected through a minimum neck of size 2. For meanders the equivalent of a mimbu is an area of the meander that is only connected/contained via the river to the rest of the structure and has no roads leaving. It is a meander system that you could take out and replace with another meander system without changing the rest of the structure. For clarity, such a 'meander baby universe' is drawn in Figure 2.24. It is clear in Figure 2.24 that the red baby universe is connected only through 2 edges which is the minimum neck. For $q = 1$, the total amount of meander configurations of size n is given by Equation (2.2). This allows to calculate the probability for finding a 'meander baby universe' of size n and ultimately make predictions about the string susceptibility at $q = 1$. The probability for a 'meander baby universe' of size n defined as p is given by:

$$p = \frac{2(c_n)^2(c_{N-n})^2}{(c_n)^2} \tag{2.20}$$

where c_n are the Catalan numbers. It should be noted that N and n in this case correspond to the order of the meander. This means that the number of faces of the geometry is always even, because there is one face per bridge and a meander of order N has $2N$ bridges. The mimbu's therefore also need to consist of an even number of faces, because it must be possible 'to take a mimbu out'. There will however still be $2N$ possible starting positions for the 'meander baby universe' of order n which explains the factor 2 in the numerator.

From the probability defined in Equation (2.20), one can try to find the asymptotic behavior and then compare

it to Equation (2.7) to find the analytic string susceptibility.

In order to expand the Equation (2.20), the asymptotic approximation of the Catalan numbers is used

$$c_n = \frac{4^n}{\sqrt{\pi} n^{3/2}} \left(1 + O\left(\frac{1}{n}\right)\right) \tag{2.21}$$

which when substituted into Equation (2.20) gives

$$\begin{aligned} p &= \frac{2}{\pi} \frac{N^3}{n^3(N-n)^3} \frac{\left(1 + O\left(\frac{1}{n}\right)\right)^2 \left(1 + O\left(\frac{1}{N-n}\right)\right)^2}{\left(1 + O\left(\frac{1}{N}\right)\right)^2} \\ &= \frac{2}{\pi} (n \cdot (1 - n/N))^{-3} \frac{\left(1 + O\left(\frac{1}{n}\right)\right)^2 \left(1 + O\left(\frac{1}{N-n}\right)\right)^2}{\left(1 + O\left(\frac{1}{N}\right)\right)^2} \end{aligned} \tag{2.22}$$

Comparing the $(n \cdot (1-n/N))^{-3}$ term in Equation (2.22) to $(n \cdot (1-n/N))^{\gamma-2}$ in equation (2.7) describing the probability of finding a baby universe of size n, gives for the string susceptibility a value of $\gamma = -1$ for $q = 1$, which corresponds to the critical exponents found in section 2.6.4.

Equation (2.22) can be used to fit the string susceptibility by substituting -3 by $\gamma_s - 2$ which gives

$$p = \frac{2}{\pi} (n \cdot (1 - n/N))^{\gamma_s - 2} \frac{\left(1 - c(n)^{-d}\right)^2 \left(1 - c(N-n)^{-d}\right)^2}{\left(1 - c(N)^{-d}\right)^2} \tag{2.23}$$

where also $O\left(\frac{1}{n}\right)$ is substituted by $-cn^{-d}$ and c and d will be fit parameters determined by fitting. The signs in front of the free parameter have been determined by comparing the approximation (Equation (2.23)) to the analytic result and setting the free parameters such that for $q = 1, c > 0, d > 0$ one gets the best fit. The approximation can be seen in Figure 2.25 where $\gamma = -1, c = 1$ and $d = 1$.

From Figure 2.25, it is clear that the probability for a mimbu of size n approaches the analytic probability for meanders with a mimbu in the asymptotic. Furthermore, the same goes for the approximation of the analytic result.

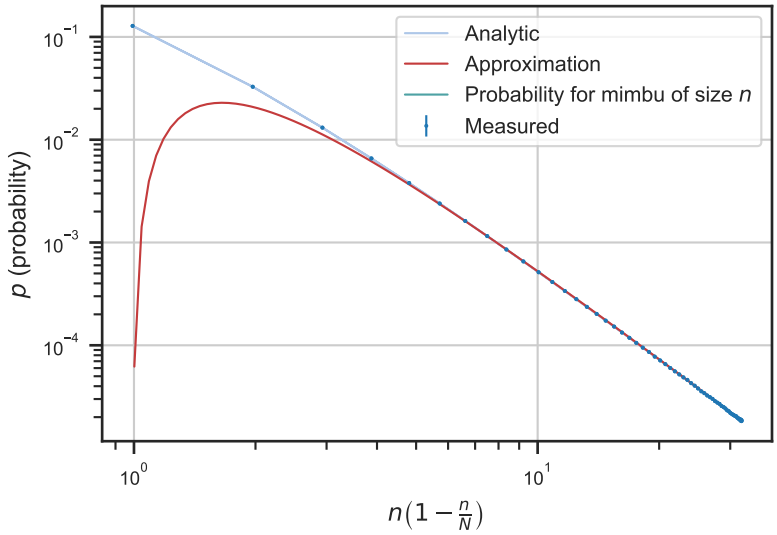

Figure 2.25: *Plot of p versus $n\left(1-\frac{n}{N}\right)$ on a logarithmic scale. The measured data in the plot is taken from a meander system of $n = 128$ and $q = 1$. The analytic graph is Equation (2.20) with exact values for the Catalan numbers c_n. The approximation is based on Equation (2.23) with $\gamma = -1, c = 1, d = 1$. The probability for mimbu of size n is based on the approximation from Equation (2.20).*

CHAPTER 3

Methods

3.1 Markov chain Monte Carlo Techniques

In order to study the conjectures by Di Francesco et al. about meanders, geometries decorated with meanders will be generated using Markov Chain Monte Carlo Techniques. Markov chain Monte Carlo was introduced by Nicholas Metropolis et al. in 1953 [35]. The main goal of Markov chain Monte Carlo techniques is sampling a certain probability distribution $\pi(\mathbf{x})$.

In Monte Carlo techniques there are actually two main directions, direct sampling and Markov chain sampling. The latter will be used here. With the former, direct sampling, one can for example calculate the area of a circle by generating random coordinates in a square and checking whether the distance to the origin is smaller than 1 [36]. An example is given in Figure 3.1 where using a 1000 samples π is approximated to be 3.16.

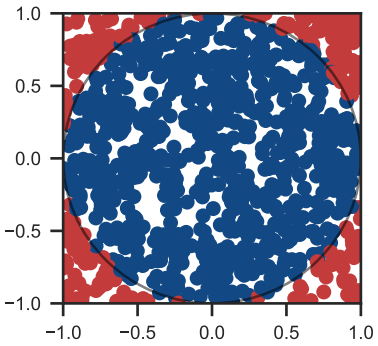

Figure 3.1: *Direct Monte Carlo sampling with* 1000 *samples estimates* $\pi \approx 3.16$.

Markov chain sampling will be used here because it doesn't sample all configurations or states but only the states most relevant which makes it more efficient than direct sampling [37]. Markov chain Monte Carlo is based on a Markov chain. The Markov chain can be represented by $X_1, X_2, X_3, \cdots \in \Gamma, \Gamma$ is a state space and X_i can be seen as a state in the Markov chain. The defining property of the Markov chain is the Markov property which states that the probability of the next configuration, X_{i+1}, only depends on the preceding configuration, X_i [13, 36]. A nice way of saying this: "The future depends on the past only through the present" by Joseph [38].

For a Markov chain to have the desired stationary distribution $\pi(\mathbf{x})$ there are two requirements: ergodicity and detailed balance. **Ergodicity** says that all possible configurations have to be reachable in the Markov chain if the Markov chain is run for sufficiently long [37]. **Detailed balance** says that the probability current between two states ν and μ should be equal. The detailed balance condition is given by

$$\pi(\nu)P(\nu \to \mu) = \pi(\mu)P(\mu \to \nu) \tag{3.1}$$

where P is the transition probability. Using the transition probability, one can define a **stationary distribution** as the distribution that satisfies

$$\pi = \mathbf{P} \cdot \pi \tag{3.2}$$

where **P** is the Markov matrix or transition matrix that encodes the transition probabilities between the different states [38]. In other words, the distribution $\pi(\mathbf{x})$ is in equilibrium when it is an eigenstate of the Markov matrix.

The goal is to use these Markov chains to calculate useful properties. For that one can define an observable $f : \Gamma \to \mathbb{R}$. So the function f translates the sample X_i into a real number.

Metropolis-Hastings algorithm

The Markov chain converges to the correct distribution $\pi(\mathbf{x})$ when detailed balance and ergodicity are satisfied. One needs to find an algorithm to generate a new configuration X_{i+1} out of X_i that satisfies detailed balance and ergodicity. The Metropolis-Hastings algorithm is suitable for this. The Metropolis-Hastings algorithm consists of two steps: proposing and accepting, visualised in Figure 3.2. First the "proposer" generates a new configuration ν from the original configuration μ with probability $g(\mu \to \nu)$. The new configuration ν is then rejected or accepted based on a certain acceptance probability $A(\mu \to \nu)$. So $g(\mu \to \nu)$ quantifies the preference or bias that the algorithm has to generate a configuration ν from μ. The acceptance probability $A(\mu \to \nu)$ fixes the probabilities in order to satisfy detailed balance. Also, one should make sure that the "proposer" satisfies ergodicity.

But what should one choose as the acceptance probability $A(\mu \to \nu)$? The first step is to split the transition probability $P(\mu \to \nu)$ (from Equation (3.1)) up into $P(\mu \to \nu) = g(\mu \to \nu)A(\mu \to \nu)$. Now one can calculate the ratio of the transition probabilities as

$$\frac{P(\mu \to \nu)}{P(\nu \to \mu)} = \frac{g(\mu \to \nu)A(\mu \to \nu)}{g(\nu \to \mu)A(\nu \to \mu)}, \frac{\pi(\nu)}{\pi(\mu)} = \frac{g(\mu \to \nu)A(\mu \to \nu)}{g(\nu \to \mu)A(\nu \to \mu)} \tag{3.3}$$

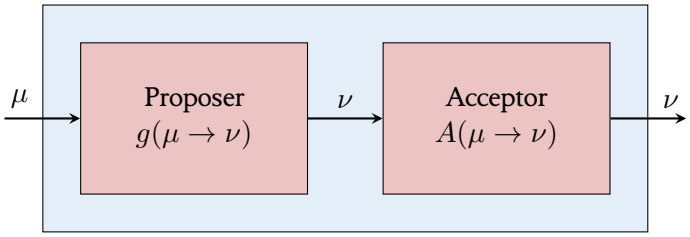

Figure 3.2: *Algorithm*

where the detailed balance condition (Equation (3.1)) is used to go from the transition probability to the ratio of the probability distribution. Rewriting Equation (3.3) gives

$$\frac{A(\mu \to \nu)}{A(\nu \to \mu)} = \frac{\pi(\nu) g(\nu \to \mu)}{\pi(\mu) g(\mu \to \nu)} \tag{3.4}$$

To satisfy Equation (3.4) the acceptance probability can be chosen as

$$A(\mu \to \nu) = \min\left(1, \frac{\pi(\nu) g(\nu \to \mu)}{\pi(\mu) g(\mu \to \nu)}\right) \tag{3.5}$$

which makes sure detailed balance is satisfied.

3.1.1 The flip algorithm

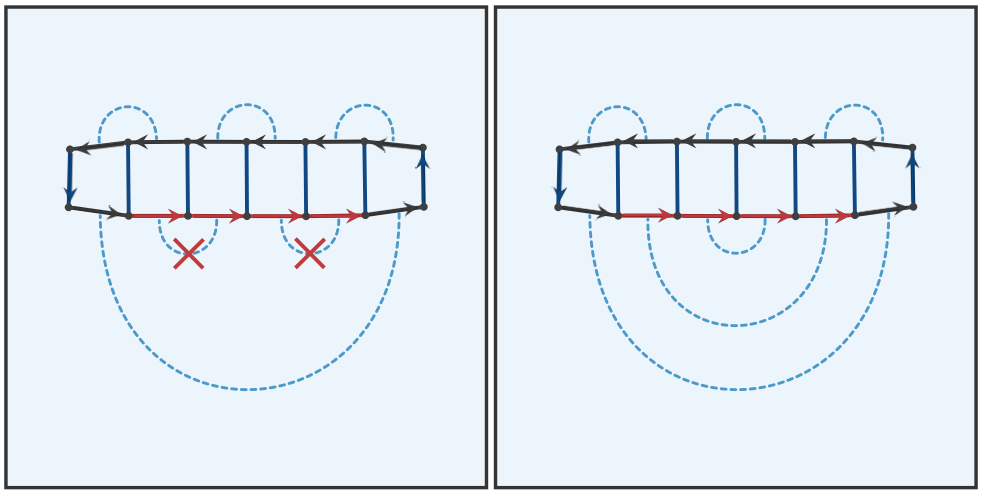

(a) $n = 3$

(b) $n = 3$

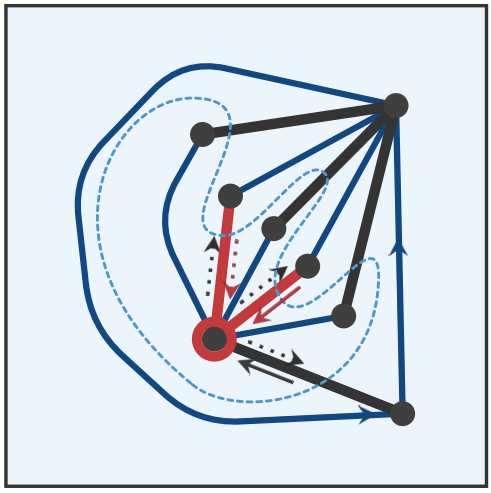

(c) $n = 3$

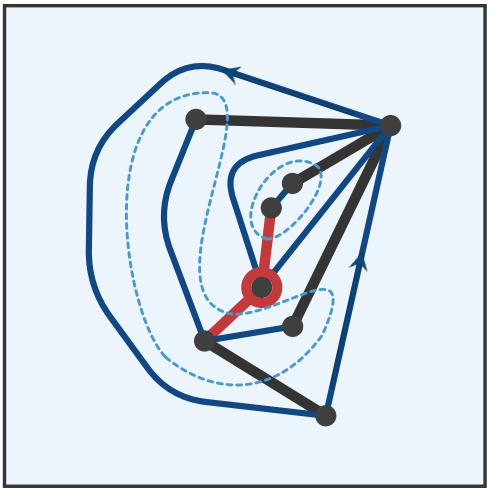

(d) $n = 3$

Figure 3.3: *Sketch of the algorithm to propose new meander configurations. (c), (d) is the map that one gets when (a), (b) are embedded on a flat plane. The algorithm transforms (a) into (b) and (c) into (d). The blue dashed line represents the road and how the quadrangles should be glued together. The river flows perpendicular to the blue edges. The red outlined lined vertex indicates the relevant vertex for the flip and v is the number of shore edges connected a red-lined node. The red and dark grey are the shore edges. The shore edges are perpendicular to the road (they can also be seen as the 'bridge pillars'). In (a),*

Here the algorithm to propose a new quadrangulation X_{i+1}, decorated with a meander system, from the original configuration X_i will be introduced. In Figure 3.3a, the flip move can be regarded as cutting the two arcs at the locations indicated with the red crosses. Then in Figure 3.3b, the red shore edges are glued back together but switched. The computer understands the quadrangulations as a combinatorial object described by cycles of the next and adjacent edges. For finding the exact proposal algorithm, one should look at Figures 3.3c and 3.3d. The interpretation of the move in Figures 3.3c and 3.3d is described in the following.

In Figure 3.3c, a shore half-edge i is selected by randomly sampling one of all the shore half-edges. Shore edges are indicated by the red and dark grey lines in Figure 3.3. The shore edges are perpendicular to the roads and roads are indicated by the blue dashed line. There are a total of $4n$ shore half-edges and therefore the shore half-edge with index i is selected with a probability $\frac{1}{4n}$. In Figure 3.3c, the dotted red half-edge pointing to the red outlined vertex is the initially selected shore half-edge. From the other half-edges pointing to the red outlined vertex, a new shore edge j is randomly selected. In Figure 3.3c, the non-dotted red half-edge is the newly selected shore edge. There are $v-1$ **other** shore half-edges pointing to the vertex and thus the probability for picking a shore half-edge j is $\frac{1}{v-1}$. The amount of shore half-edges pointing to the red outlined vertex in Figure 3.3c is equal to $v=3$.

The procedure to generate configuration ν from μ is done by un-glueing the initially selected shore half-edge and the new selected shore half-edge from their adjacent edges and then re-glueing to the adjacent edges switched. In Figure 3.3d, the resulting new configuration ν is drawn. The un-glueing and re-glueing is demonstrated in Figure 3.4 where i is the initially select half-shore edge, $a(i)$ is the adjacent half-edge of i, j is the new half-shore edge and $a(j)$ the adjacent half-edge of j. The glueing changes from $i \leftrightarrow a(i), j \leftrightarrow a(j)$ to $i \leftrightarrow a(j), j \leftrightarrow a(i)$, where $a(i)$ and $a(j)$ refer to the old glueing.

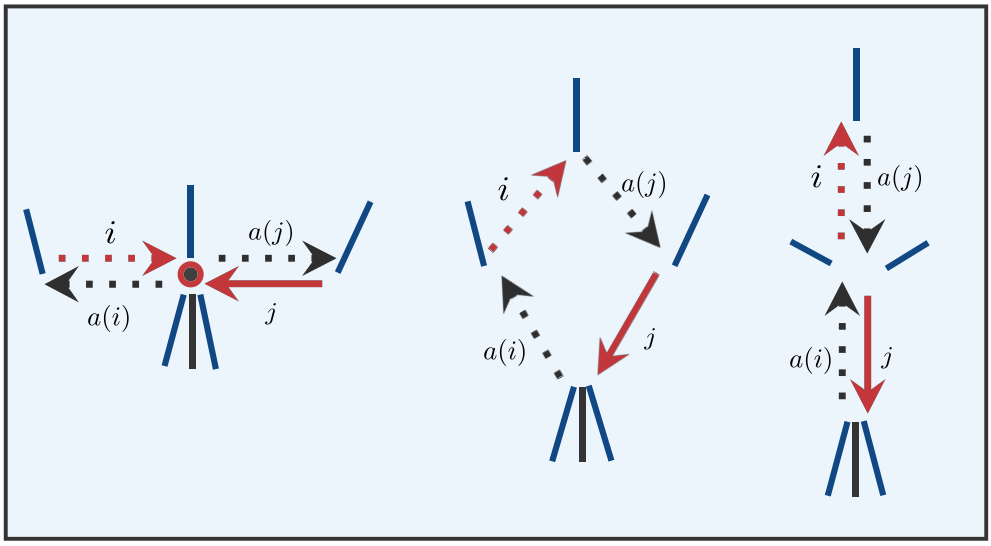

Figure 3.4: *Detailed drawing what happens around the flip vertex indicated by the red outlined vertex. The drawing is a part of Figure 3.3c and Figure 3.3d with the same meaning to colors and dotted edges. On the left is the initial state μ, in the middle the un-glued state and on the right the re-glued new state ν.*

The probability for selecting a certain new configuration ν is $g(\mu \to \nu) = \frac{1}{4n}\frac{1}{v_\mu - 1}$ where v is the amount of shore half-edges pointing to the red outlined vertex. The probability for going from state ν to state μ is similarly given by $g(\nu \to \mu) = \frac{1}{4n}\frac{1}{v_\nu - 1}$.

With the introduced information about the proposing algorithm, the acceptance probability can be derived. The Metropolis-Hastings acceptance probability from equation (3.5) can be used to sample based on the probability distribution $\pi(x)$ [13]. The partition function for the meander systems from section 2.6.1 is given by

$$Z = \sum_{configurations} q^k \tag{3.6}$$

and the probability distribution is then given by

$$\pi(\mathbf{x}) = \frac{1}{Z} q^{k(\mathbf{x})} \tag{3.7}$$

where k is the number of components and q is the weight of the roads. Substituting g and π into Equation (3.5) gives

$$A(\mu \to \nu) = \min\left(1, q^{k_\nu - k_\mu} \cdot \frac{v_\mu - 1}{v_\nu - 1}\right) \tag{3.8}$$

which is the acceptance probability to accept or reject a proposed configuration.

The algorithm proposed in this section allows generating Markov chains of these meander configurations where q, the weight assigned to the roads, is variable.

3.1.2 Practical Markov-Chain Monte Carlo

One can only perform measurements when the probability distribution is stable, and the samples should be independent of one another to get accurate error estimates. The analysis of Markov chain Monte Carlo data involves several steps: finding the equilibration time, finding the correlation time and estimating the error. These practicalities will be described in this section.

It is best to start with small system sizes on which many flips can be performed in little time. This way, one can check that the Markov chain is discovering the entire state space and thus ergodicity holds [38].

Convention and notation

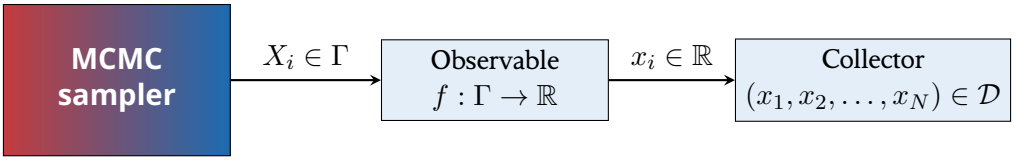

Figure 3.5: *Performing a Markov chain Monte Carlo Experiment*

As defined in section 3.1, the Markov chain can be represented by $X_1,\ X_2,\ X_3, \cdots \in \Gamma$ where X_i is a state in the Markov chain. One can perform measurements on these states X_i using an observable $f : \Gamma \to \mathbb{R}$, for example $f(X_i) = k_{\text{components}}(X_i)$. For simplicity from here on, x_i shall refer to a sample of an observable in the dataset $\mathcal{D}$ of N measurements. The idea is sketched in Figure 3.5 where $x_i = f(X_i) \in \mathcal{D}$.

The values of a variable x_i will be distributed according to a certain probability distribution $P(x)$. One property to characterise this probability distribution is the standard deviation, σ, which is the square root of the variance. $\overline{\cdots}$ indicates an average over N data points and $\langle \cdots \rangle$ indicates the average over a distribution. The mean is then defined as $\mu \equiv \langle x \rangle$ and the standard deviation is $\sigma^2 \equiv \langle (x - \langle x \rangle)^2 \rangle$ [39]. This notation is based on a summary by Peter Young about data analysis [39].

The goal is estimate μ and σ using the data points. For that the sample mean, $\bar{x}$, and sample variance, s^2, are defined by:

$$\bar{x} = \frac{1}{N} \sum_{i=1}^{N} x_i \tag{3.9}$$

$$s^2 = \frac{1}{N} \sum_{i=1}^{N} (x_i - \bar{x})^2 \tag{3.10}$$

where N is the number of data points [39].

Performing many repetitions of the experiment gives the best estimate of the mean μ as

$$\mu = \bar{x} \tag{3.11}$$

and the best estimate for the variance, σ^2, by

$$\sigma^2 = \frac{N}{N-1}s^2 = \frac{1}{N-1}\sum_{i=1}^{N}(x_i - \bar{x})^2 \tag{3.12}$$

which follows from equation (3.10).

One can now define the standard error, $S_{\bar{x}}$ which is the standard deviation on the mean, $\bar{x}$ given by

$$\mu = \bar{x} \pm S_{\bar{x}} \tag{3.13}$$

where, if all x_i and x_j are statistically independent, $S_{\bar{x}}$ is given by

$$S_{\bar{x}} = \frac{\sigma}{\sqrt{N}} = \frac{s}{\sqrt{N-1}} \tag{3.14}$$

$$S_{\bar{x}} = \sqrt{\frac{1}{N(N-1)}\sum_{i=1}^{N}(x_i - \bar{x})^2} \tag{3.15}$$

where σ is the standard deviation and N is the number of data points [39]. Equation (3.15) follows from equation (3.14) by substituting equation (3.12). The standard error given by equation (3.15) is unbiased [39]. The notation $S_{\bar{x}}$ is chosen to really emphasize that it is a statistical error or standard deviation of the mean and NOT the standard deviation. For a detailed and clear derivation of the quantities described have a look at [39] by Young.

Equilibration time

Since a Markov chain depends on its history and the initial conditions, the chain has to equilibrate. The unequilibrated part of the Markov chain must be removed in order to only work with a properly equilibrated chain. This means that the equation to calculate the expectation value for the observable f must be slightly changed to

$$\overline{f} = \frac{1}{n-b}\sum_{i=b+1}^{n} f(X_i) \tag{3.16}$$

where X_i is a state in the Markov chain and where b is the cut-off.

The first variable to find is the equilibration time τ_{eq} and choose b well above the equilibration time τ_{eq}. Time in these Markov chains are the number of performed flips. For simplicity, this can be expressed in the number of sweeps which is the average number of flips per element of the system. In the case of meanders, the number of sweeps will be defined as the average number of flips per bridge. So a sweep will be defined as $2n$ flips.

$$1 \text{ sweep} = 2n \text{ flips} \tag{3.17}$$

where n refers to the order of the meander. A sweep corresponds performing on average one flip per bridge or face.

Correlation time

The Markov chain is statistical method that uses randomness to approximate a certain distribution. The Markov-chain changes when one performs flips. Performing x flips can be interpreted as a time-axis and samples on this time-axis are correlated. The correlation means that the state X_i and X_j in the Markov chain are correlated, and thus not statistically independent. The standard method of estimating the statistical error given by equation (3.15) is invalid for a Markov chain.

For an observable f, one can quantify this correlation by the autocorrelation function. The autocorrelation function is the normalized autocovariance given by

$$\Gamma_a = \frac{1}{N-a} \sum_{k=1}^{(N-a)} (f_k - \langle f \rangle)(f_{k+a} - \langle f \rangle) \tag{3.18}$$

and the autocorrelation function is given by

$$\rho_a = \frac{\Gamma_a}{\Gamma_0} \tag{3.19}$$

The normalized sample autocovariance that estimates the normalized autocovariance is given by

$$\gamma_a = \frac{1}{N-a} \sum_{k=1}^{(N-a)} (x_k - \bar{x})(x_{k+a} - \bar{x}) \tag{3.20}$$

where $x_i \in \mathcal{D}$ and the sample autocorrelation function is then given by [13, 38]

$$\bar{\rho}_a = \frac{\gamma_a}{\gamma_0} \tag{3.21}$$

The autocorrelation function can be approximated by an exponential $\exp(-t/\tau)$ where τ is the so-called autocorrelation time. One method of determining the autocorrelation time is therefore by fitting an exponential to the autocorrelation function [13]. The other method is using τ_{int} which is the integrated autocorrelation time given by [38]

$$\tau_{\text{int}} = \frac{1}{2} + \sum_{a=1}^{M} \rho_a \tag{3.22}$$

Taking $M \to \infty$ would give a high uncertainty since we would consider the autocorrelation over a small section of the Markov chain (as can be seen from equation (3.18)) which causes a higher variance. To get around this problem a cut-off should be chosen [38]. One can choose M as the first M that satisfies

$$M \geq 4\tau_{\text{int}} + 1 \tag{3.23}$$

for which τ_{int} is the autocorrelation time, so $\tau_{\text{int}} = \tau$.

Fitting an exponential to the autocorrelation function is demonstrated in Figure 3.6a. In Figure 3.6a, the easiest method is for fitting an exponential is used: namely by checking where the exponential intersects with $1/e$. This works because at $t = \tau$, $e^{-t/\tau} = 1/e$. The other method is using least-mean squares/regression

and transform to a logarithmic scale for that, however a cut-off should be implemented since the tail of the autocorrelation function will be noisy [37]. In Figure 3.6b, fitting based on the τ_{int}-method is demonstrated by finding the first M for which $M \geq 4\tau_{\text{int}} + 1$.

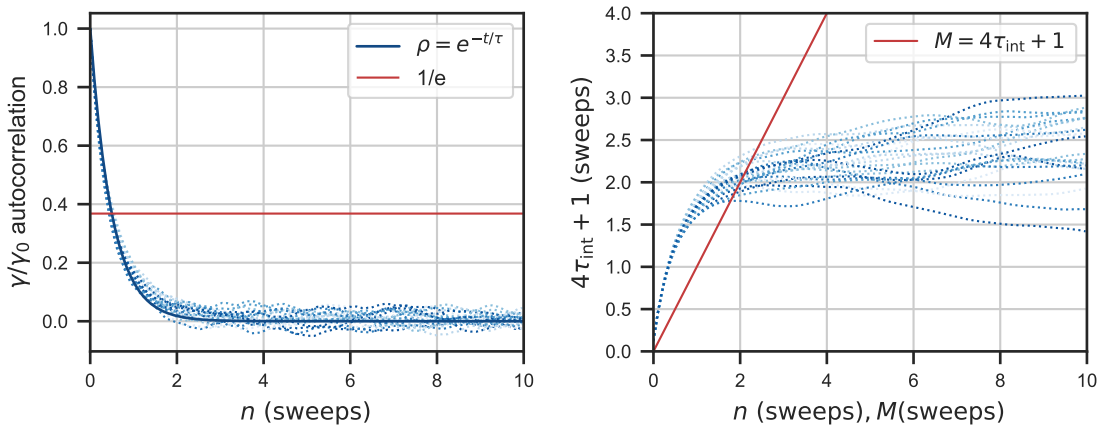

(a) (b)

Figure 3.6: *Measurements of the autocorrelation time τ in* sweeps. *(a) The autocorrelation time is measured by finding the intersection with $\gamma/\gamma_0 = 1/e$. (b) The autocorrelation time is fitted using the τ_{int}-method. The measured autocorrelation times by averaging 24 measurements are (a) $\tau = 0.498 \pm 0.006$ and (b) $\tau = 0.516 \pm 0.008$. The different measurements are indicated with the dotted lines.*

Using the autocorrelation of an observable of the Markov chain, the statistical error of the Markov chain can be studied. The promise of this method is to be more effective than binning strategies which will be later introduced [38].

The statistical error $S_{\bar{x}}$ for an observable f with a correlated dataset $(x_1, x_2, \ldots, x_N) \in \mathcal{D}$ is given by

$$S_{\bar{x}} = \sqrt{\frac{1 + 2\tau/\Delta t}{n-1}\left(\frac{1}{N}\sum_{i=1}^{N}(x_i - \bar{x})^2\right)} \tag{3.24}$$

where τ is the autocorrelation time that was defined earlier and Δt is the measurement interval. The measurement interval is introduced such that the information saved is less ambiguous because the measurements will be less correlated. Equation (3.24) has some properties, if the autocorrelation time τ is very small, one finds the usual definition for the statistical error, like in equation (3.15). When $\tau \gg \Delta t$ and $n \gg 1$, equation (3.24) can be simplified. First, use $n \gg 1$ and $n = \frac{t_{\text{max}}}{\Delta t}$ which gives

$$S_{\bar{x}} = \sqrt{\frac{\Delta t(1 + 2\tau/\Delta t)}{t_{\text{max}}}s^2} \tag{3.25}$$

and now use $\tau/\Delta t \gg 1$ resulting in

$$S_{\bar{x}} = \sqrt{\frac{2\tau}{t_{\text{max}}} s^2}, S_{\bar{x}} = \sqrt{\frac{2\tau}{n\Delta t} s^2} \tag{3.26}$$

where it must be emphasized that this formula is **only valid under the assumptions**: $n \gg 1$ and $\tau \gg \Delta t$, i.e. many samples per autocorrelation time τ and the measurement interval must be way smaller than the autocorrelation time. Equation (3.26) shows that one can choose the most convenient measurement interval Δt. We should however keep the **assumptions** in mind [37].

Taking the measurement interval Δt to be equal to 2τ is the most natural definition of statistical independence [37]. This follows from taking $\Delta t = 1$ in equation (3.26) which results in

$$S_{\bar{x}} = \sqrt{\frac{2\tau}{n} s^2} \tag{3.27}$$

Taking $\Delta t = 2\tau$ would have resulted in the standard formula for the statistical error of the observable f. This is not true, since $\Delta t = 2\tau$ does not satisfy $\tau / \Delta t \gg 1$. The correct error for samples taken at $\Delta t = 2\tau$ can be derived from equation (3.24), which yields

$$S_{\bar{x}} = \sqrt{\frac{2\sigma^2}{n}} = \sqrt{2 \left(S_{\bar{x}}^{\text{statistically independent}} \right)^2} \tag{3.28}$$

3.1.3 Error analysis

In this section binning, bootstrap, stationary bootstrap and jackknife will be introduced as another way to estimate statistical errors.

Blocking, binning, bunching or batching

The binning method, also known as blocking method or batching method, splits the Markov chain into N_b equal sized bins of length m [13, 36, 37, 40]. By taking the average of each bin, one can interpret the N_b averages as performing the experiment N_b times. The opinion about binning for estimating errors is mixed. Although, with the right procedures and checks, binning can give good results. As described by Krauth in [36], it is useful to do binning for different bin sizes. In the case of working below the correlation time of the Markov chain the error will be underestimated since the averages of the bins will then also be correlated. For bin sizes larger than the autocorrelation time, one expects to find the same and correct error. This can be seen in Figure 3.7 where the error flattens when the bin size m is sufficiently large. For very large bin sizes the error of the error will increase because the total number of bins N_b will be low. The batching method will thus give good results for bin sizes way larger than the autocorrelation time (while still having sufficient bins to get an accurate statistical error).

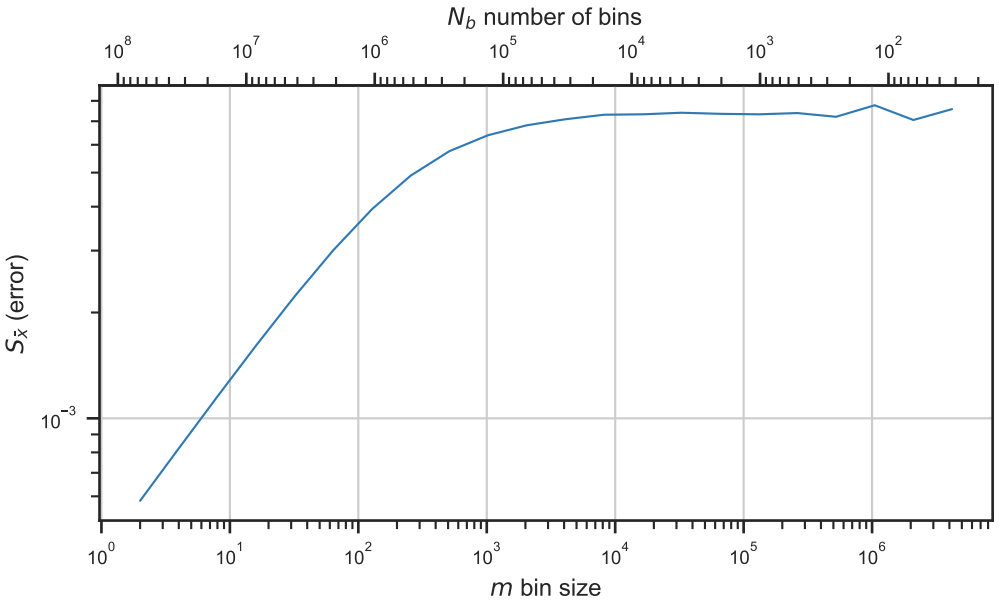

Figure 3.7: *Demonstration of the binning method on a Markov chain. The observable is the number of components, k. The statistical error versus the bin sizes is plotted in the diagram. We can clearly identify the statistical error increasing for larger bin sizes and thus fewer bins. The region where bins are independent can also be identified. The properties of the system: a measurement interval $\Delta t = 1$, size $n = 128$ and number of samples $N = 2^{27} = 1,34218 \cdot 10^{18}$. Smallest bin size $m = 2$ and smallest number of bins $N_b = 32$.*

Bootstrap method

The bootstrap method is a resampling method of a dataset $\mathcal{D}$ of size n, $x_1, x_2, x_3, \ldots, x_n$, one samples randomly n data points resulting in a new dataset $x_{\text{RNG}(1)}, x_{\text{RNG}(2)}, \ldots, x_{\text{RNG}(n)}$. In the new dataset, there can be **duplicate** elements, on average 63% will be duplicates. From this new resampled dataset, one can again calculate the average denoted by c_i [37]. Typically, one resamples m times, so m new datasets and m averages, $c_1, c_2, \ldots, c_m$. Lastly, the final statistical error is calculated by:

$$S_{\bar{x}} = \sqrt{\sum_{i=1}^{n}(c_i - c)^2} = \sqrt{\overline{c^2} - \bar{c}^2} \tag{3.29}$$

The Bootstrap method promises to also handle correlated data [37].

A slightly modified version of the Bootstrap method is Stationary bootstrap. Stationary Bootstrap adds a resampling probability p. The resampling probability results in resampling subsequences of typical lengths $1/p$ of the original data [13]. Here insert.....[41].

Jackknife method

The jackknife method, somewhat similar to leave-one-out cross-validation, creates n datasets from the original data set, but the i^{th} element of the original dataset is left out. The averages of these datasets can be called c_i. The error estimate is then given by [37]

$$S_{\bar{x}} = \sqrt{\sum_{i=1}^{n}(c_i - c)^2} = \sqrt{\overline{c^2} - \bar{c}^2} \tag{3.30}$$

Jackknife is best fit for smaller datasets since it creates n new datasets from one dataset of length n. Jackknife only works with uncorrelated data [37]. Jackknife is typically used to calculate the statistical error of the final results of an experiment conducted 10 times.

3.1.4 Performing Monte Carlo simulations

In the previous section, it was discussed that Markov chains are correlated. Storing information about every state in the Markov chain is inefficient. It is best to measure at a rate r, as described in Figure 3.8.

Two good variables to control are the number of sweeps and the number of measurements per sweep. These two variables have a natural relation with the autocorrelation and statistical error and thus one can intuitively change the accuracy. Here these quantities are related to each other.

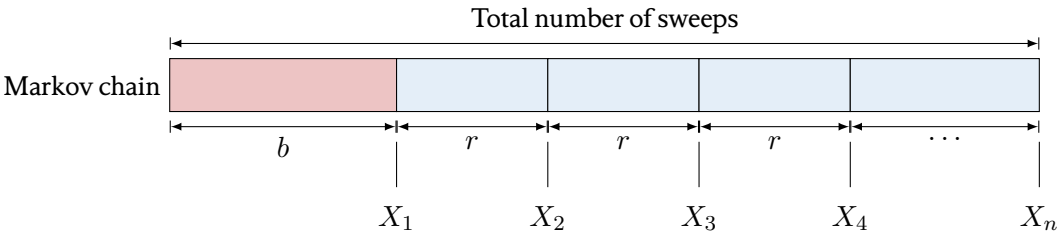

Figure 3.8: *Markov chain Monte Carlo simulation setup, where* $b \geq \tau_{\text{eq}}$

ρ_{samples} is the number of measurements per sweep (density). This translates to a rate $r = \frac{2n}{\rho_{\text{samples}}}$ and a total number of measurements $n_{\text{measurements}} = \frac{n_{\text{sweeps}} 2n}{r}$.

3.2 Phase transitions

Measuring and identifying phase transition is an important problem in physics. First one must introduce an order parameter, ϕ, which is a local observable of the system that is $\phi = 0$ for $q > q_c$ and $\phi \neq 0$ for $q < q_c$.

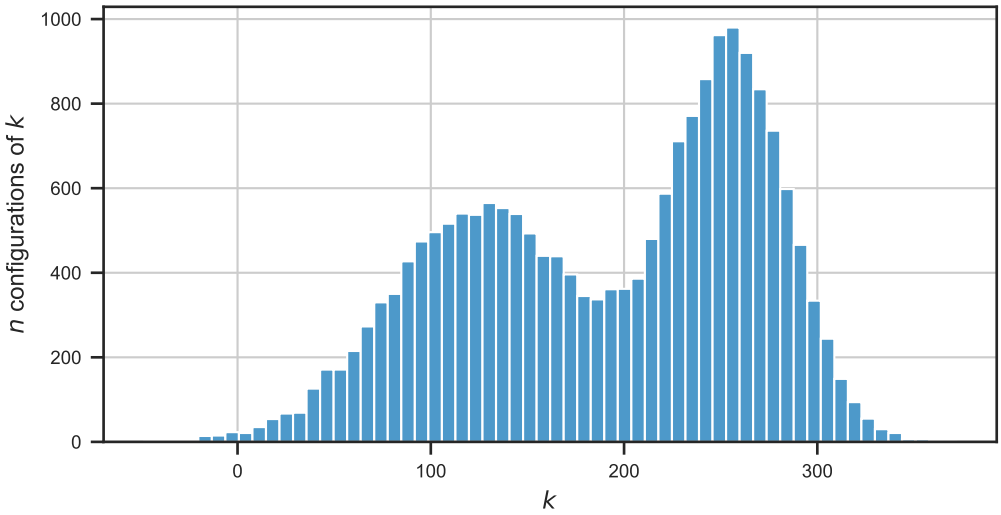

Figure 3.9: *Made-up plot of histogram of k-components of meander configuration in a Markov-chain double that shows a double-peak structure at q_c.*

At the critical point q_c of a phase transition, one would expect to find configurations of both phases at the phase transition. In the case of a Markov chain Monte Carlo simulation, the Markov-chain will then contain samples from both phases, which results in a histogram with two peaks, in other words a double-peak structure like in Figure 3.9. The Markov chain then jumps between two metastable states [25].

In Figure 3.9, the double peak structure is clearly visible. That is however not always the case and therefore one needs a tool to measure deviations from a Gaussian distribution. For that, one can use the Binder cumulant. The Binder cumulant is defined as

$$U_4 = 1 - \frac{\langle f^4 \rangle}{3\langle f^2 \rangle^2} \tag{3.31}$$

where $\langle f \rangle$ is the order parameter.

When the distribution is Gaussian the relation: $\langle f^4 \rangle = 3\langle f^2 \rangle^2$, will cause the Binder cumulant to go to zero. If the Binder cumulant is calculated for different system sizes versus a parameter (take the weigth q for example) then the graphs of the different system sizes should cross at a point q_c [42, 43]. For large systems sizes, the Binder cumulant, U_4, should be $U_4 \to 0$ for $q > q_c$ and $U_4 \to 2/3$ for $q < q_c$ for system size $L \to \infty$[44].

CHAPTER 4

Research question, goals and setup

Di Francesco et al. conjectures that meanders are governed by a conformal field theory (CFT) coupled to two-dimensional quantum gravity (2DQG). Several predictions are made about the phases and the associated critical exponents of 2DQG coupled to meanders, see section 2.6.4. This also leads to a general research question: is there numerical evidence that verifies or falsifies the conjecture that meanders are governed by CFT coupled to 2DQG?

From this the following goals and research questions can be formulated:

- The goal is to study the predicted phase transition to the branched polymer phase for $q > 2$. This phase transition is however quite special since there are not two distinct phases. Instead, the phase is predicted to change continuously for $0 \leq q \leq 2$ and jump to a branched polymer phase for $q > 2$.
- Can the phase transition at $q = 2$ be measured using the Binder cumulant with the number of roads/-components as the order parameter?
- Does the predicted string susceptibility as a function of q match the numerical results? The string susceptibility will be explicitly looked at for $q = 2$ where Di Francesco et al. report deviations from their numerical simulations in [3] and [1].
- Does the predicted value Hausdorff dimension as a function of q match numerical results? The predictions for the Hausdorff dimension are calculated from the string susceptibility. The string susceptibility γ_s is related to the Liouville coupling constant γ which can be related to the Hausdorff dimension using the Ding and Gwynne formula, see Equation (2.12).

Numerical studies of the critical exponents of meanders have been done in the past. In [1] by Di Francesco et al. in 2000, all meanders were enumerated up to $n = 24$ [1] which allowed to measure critical exponents. In [45] by Golinelli in 2000, meanders were sampled up to $n = 400$ using a Monte Carlo method which was based on a recursion relation. In [46] by Jensen and Guttmann in 2000, all meanders were enumerated up

to $n = 48$ using a new algorithm that they developed. In [46], they also show that the conjectured critical exponent predicted for semi-meanders (one road does not cross the river but instead goes around the river) could be incorrect [46]. A review [47] by Legendre in 2014 mentions a new algorithm from 2012 to enumerate semi-meanders and open meanders by [48]. For this work however only closed meanders will be studied.

Little to no numerical work has been done on large size ($n > 1000$) closed meander systems. This work will try to fill this knowledge gap using the in section 3.1.1 developed Markov chain Monte Carlo flip. The Markov chain Monte Carlo method allows generating configuration up to $n = 262144$ and even higher which are sizes never studied before. Also, the Hausdorff dimension has never been measured for random surfaces decorated with meanders. Using these novel techniques, the aim is to find new numerical evidence about the conjecture that meanders are governed by 2DQG.

4.1 Setup

Performing the Markov chain Monte Carlo simulations is done by writing a C++ program that implements the flip algorithm developed in section 3.1.1. The implementation contains a few non-trivialities in order to optimize the performance such that the time-complexity of the flip algorithm scales like $O(\log n)$ where n is the system size of the meander.

For calculating the acceptance probability, it is required to know the number of roads of the meander system. The number of roads are tracked using "dynamic permutations" that can be cut and linked in $O(\log n)$ time. The dtree library by David Eisenstat (www.davideisenstat.com/dtree/) is used, which implements dynamic sequences based on Splay trees. Splay trees are invented by Sleator and Tarjan in 1985 [49]. The dtree library by David Eisenstat library is used because it already implements a lot of the functionality required for making "dynamic permutations" possible. The dynamic sequences of the library were used to implement "dynamic permutations", in other words permutations that can be cut and linked in $O(\log n)$ time.

In C++ also routines for measuring distance profiles and finding baby universes were implemented. The program also handles the creation of labeled files encoded in JSON [50]. Managing the compiling was done using CMake and the GNU GCC 9.4.0 compiler was used to compile the sources on the clusters. Catch2 was used to write some unit tests for testing different sizes and measuring the performance.

The implementation of the algorithm has a performance of 18.8 ms for 10000 flips at system size $n = 100$. For system size $n = 1000000$, it takes about 80 ms to perform 10000 flips. The implementation therefore scales really well in terms of performance when increasing the system size. This allows to study large meander systems.

The data analysis took place in Python (Anaconda3-2022.05 and Python 3.9.12) using mostly Numpy, Pandas, Scipy and Scikit-learn.

CHAPTER 5

Results

Using Markov chain Monte Carlo simulations quadrangulations glued based on meander configurations/quadrangulations decorated by meanders were sampled. The numerical results are presented in the following sections and contain the number of components, Binder cumulant, string susceptibility and the Hausdorff dimension. For the number of components, a detailed analysis was done of the different error estimation techniques for Markov chain Monte Carlo. Note that if not otherwise noted the system size n refers to the order of the meander system.

5.1 Number of components

To study the predicted phase transition, the number of components k is studied as a function of the order of the meander system n and the weight q. The number of components k is the number of roads in a meander system. Also, the Binder cumulant is calculated to further investigate the predicted phase transition.

5.1.1 Preliminaries

Thermalization time

As described in Figure 5.1, the Monte Carlo sampler requires a measuring rate k at which the Markov chain will be measured and the total number of measurements $n_{\text{measurements}}$ that need to be performed. The goal is to only save to the disk what is needed. It will be assumed that the order of magnitude of the thermalization time will be around $10 - 100$ sweeps. It is therefore also assumed that the thermalization time scales linearly with the system size.

For the following measurements, the sample density, was chosen to be $\rho_{\text{samples}} = 64$ samples per sweep. The number of values for a 1000 sweep run is therefore limited to a maximum of 64.000 samples independent of

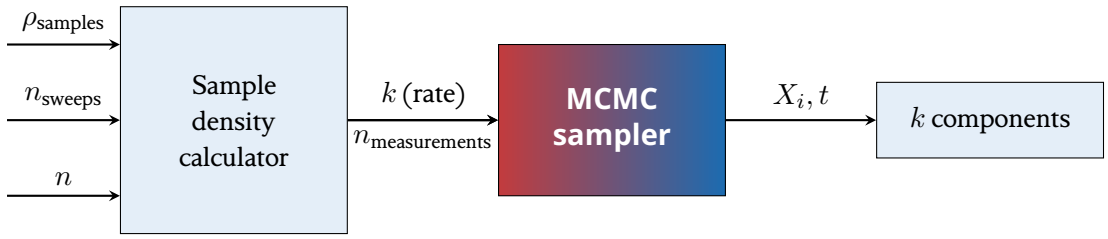

Figure 5.1: *Setup for measuring thermalization time*

the system size n. Now the thermalization time can be determined using Figure 5.2. Based on Figure 5.2, a very safe thermalization time is chosen of 512 sweeps. The assumption that the thermalization time grows linearly with the system size is also true based on Figure 5.2. The following safe thermalization time given by

$$\tau_{\text{eq}} = 512q \approx 512 \cdot \exp\left(\text{abs}(\log\left(q\right))\right) \tag{5.1}$$

which is chosen by also taking into account the thermalization graphs for different values of q.

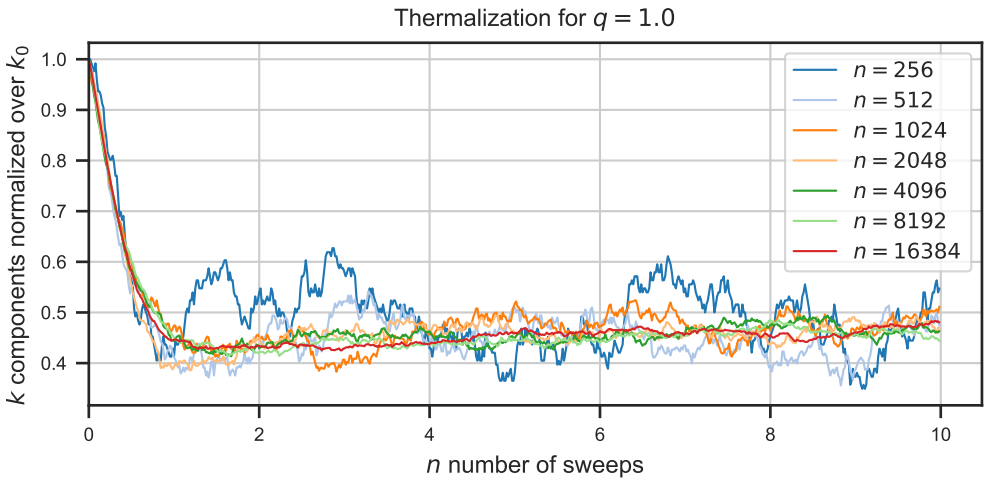

Figure 5.2: *Markov chain of the number of components k. The measurements are taken at $q = 1$ for different system sizes n. A sweep corresponds to $2n$ flips.. Note that not all data is visible in this plot. The sampling rate is* $\frac{1}{64}$ sweeps.

Unfortunately, the thermalization cannot be compared to an analytic average number of components for meanders, which would be given by

$$\langle k \rangle = \sum_k k \cdot \frac{M_n^{(k)}}{M_n} \tag{5.2}$$

since there is no analytic formula for $M_n^{(k)}$. Next up the autocorrelation of the Markov chain should be calculated. This allows to estimate a measuring rate for sampling uncorrelated/independent samples.

Autocorrelation time

In Figure 5.3, the autocorrelation time is plotted determined by the τ_{int} method, see section 3.1.2.

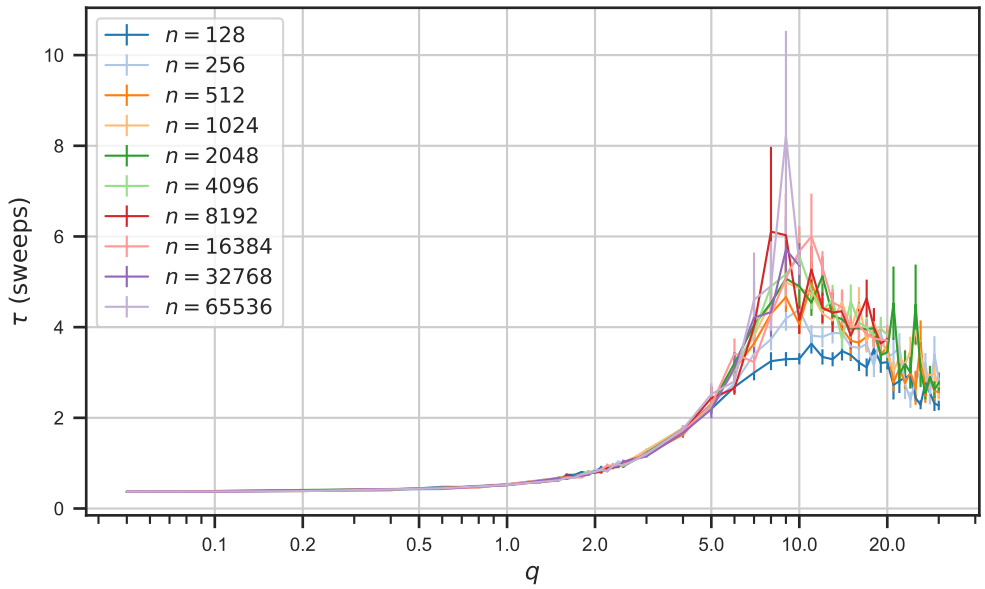

Figure 5.3: *Measurements of the autocorrelation time τ in* sweeps *for different system sizes as a function of the weight q. The autocorrelation time is fitted using the τ_{int}-method.*

Now all the variables to measure the number of components systematically are collected.

5.1.2 Error analysis

The goal is to estimate the error with an accuracy of $20 - 30\%$ of the correct error. For the k-components simulation, six methods were used to estimate the standard error (see Table 5.1). The dataset consists of measurements of the number of components, k, every 2τ autocorrelation times. The methods for estimating the error were introduced in section 3.1.3. The first method "Standard mean error" refers to simply using the standard deviation and dividing by the square root of the number of data points, the autocorrelation is then neglected. The second method uses the autocorrelation and Equation (??) to correct the statistical error of the first method. The third, fourth, fifth and sixth methods are binning, jackknife, bootstrap and stationary bootstrap respectively. They are described in section 3.1.3.

Error estimates of the different methods are displayed in Table 5.1. One can observe that the "Standard mean error" estimate equals the "Jackknife" estimate. The standard error of the "Autocorrelation", "Binning", and "Stationary Bootstrap" are similar. The "Bootstrap" estimate is somewhere in the middle with respect to the other error estimates.

Table 5.1: *Error estimates, $S_{\bar{k}}$, of the different methods introduced in section 3.1.3. The observable is k-components of a meander system. The measurements are taken at 2τ autocorrelation times and the $N = 131072$ measurements and the Markov chain consists of $N = 2.7 \cdot 10^8$ flips. The measuring rate, $r = 2\tau = 2048$.*

Method	$S_{\bar{k}}$
Standard mean error	0.037
Autocorrelation	0.052
Binning $(m = 1024)$	0.050
Jackknife	0.037
Bootstrap	0.039
Stationary bootstrap $(p = 0.005)$	0.045

For binning, a plot is made in Figure 5.4 of the standard error $S_{\bar{k}}$ versus the bin size m. In the plot, one can see that the error flattens from around a bin size of $m = 1024$. The bin size should therefore be at least $m = 1024$. Note that the measurements are taken at 2τ autocorrelation times, thus having 2048 autocorrelation times worth of data yields reliable binning estimates. 2048 autocorrelation times for $q = 1$ are equivalent to 1024 sweeps.

The error estimated using the standard mean error and jackknife doesn't take into account the correlation of the data, contrary to binning and the autocorrelation method. Autocorrelation and binning give the most accurate results and Figure 5.4 allows to check the hypothesis that the data is correlated, but if the bins are large enough the data becomes uncorrelated and the statistical error stops increasing.

For the stationary bootstrap, the data is resampled at sequences of about $1/p$ which is typically chosen on the order of the autocorrelation time. For this dataset, which is sampled at every 2τ, one should choose $p = 1$ which is the regular bootstrap estimate. By trail and error $p = 0.005$ or $1/p = 200$ was chosen since this best resembled the errors found with the autocorrelation and binning methods. It must be noted that $1/p = 200$ has the same order of magnitude as the start of the flattening for the binning analysis which will most likely explain the better results.

In conclusion, the valid methods are: binning with a bin size of $m = 1024$, stationary bootstrap and autocorrelation. The stationary bootstrap will however not be used anywhere for two reasons: estimating an extra

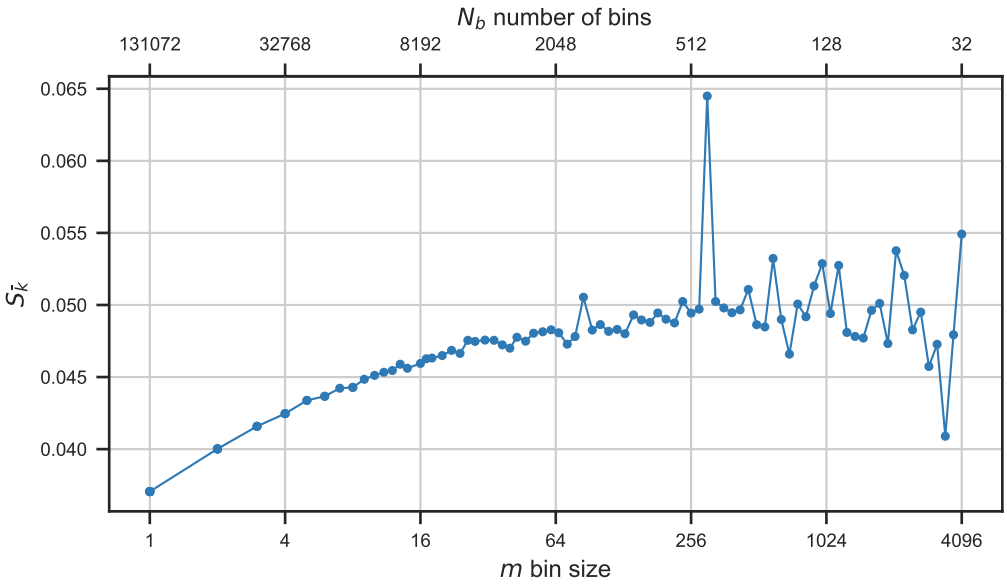

Figure 5.4: *Example of binning analysis with the standard error $S_{\bar{k}}$ of the number of components k versus the bin size m. Parameters: system size $n = 1024$ and weight $q = 1.0$. The total length of the Markov chain is $N = 131072$. A bin size of 1 corresponds to measurements taken every 2τ autocorrelation times with autocorrelation times from section 5.1.1.*

parameter p adds unwanted complexity and the randomness involved in the resampling makes the error non-deterministic.

Now the question arises for binning: what is the minimum amount of data required to get an accurate error? In Figure 5.5, a comparison between the binning and autocorrelation method was made. The different lines indicate different experiments with different system size n and weight q. The y-axis is the ratio between the error by the binning, S_{binning} divided by the error by autocorrelation, $S_{\text{autocorrelation}}$. On the x-axis, the dataset is increased, while keeping the bin size ($m = 1024$) the same. The most important observation is that all the lines converge to 1 when the number of bins/the amount of data in the data set is increased, thus the autocorrelation and binning method give consistent results for a large enough dataset. The convergence of the lines in Figure 5.5 is also quite symmetric. The same plot for $m = 512$ would show convergence to a value below 1 because the error would then be underestimated by binning.

In Figure 5.6, the standard deviation is calculated by $\sigma = S_{\bar{k}} \cdot \sqrt{N}$. The $\sqrt{N}$ correction makes the plot independent of the number of data points, but it will allow to study the fluctuations of the error when the number of data points increases. In Figure 5.6, one can clearly see that independent of the number of measurements the autocorrelation gives very consistent results. Binning is more fluctuative but it converges to the autocorrelation for larger data sets. The stationary bootstrap is also reasonable, but does not converge as much as "Binning". One could however conclude that the autocorrelation method produces accurate errors even with small datasets.

Figure 5.7 shows the amount of error estimates within the 30%-goal. The x-axis is the size of dataset and the y-axis S_{binning} divided by $S_{\text{autocorrelation}}$. Figure 5.7 measures the deviation of the binning error from the autocorrelation error, so it is assumed that the autocorrelation error is the best error which is a reasonable assumption

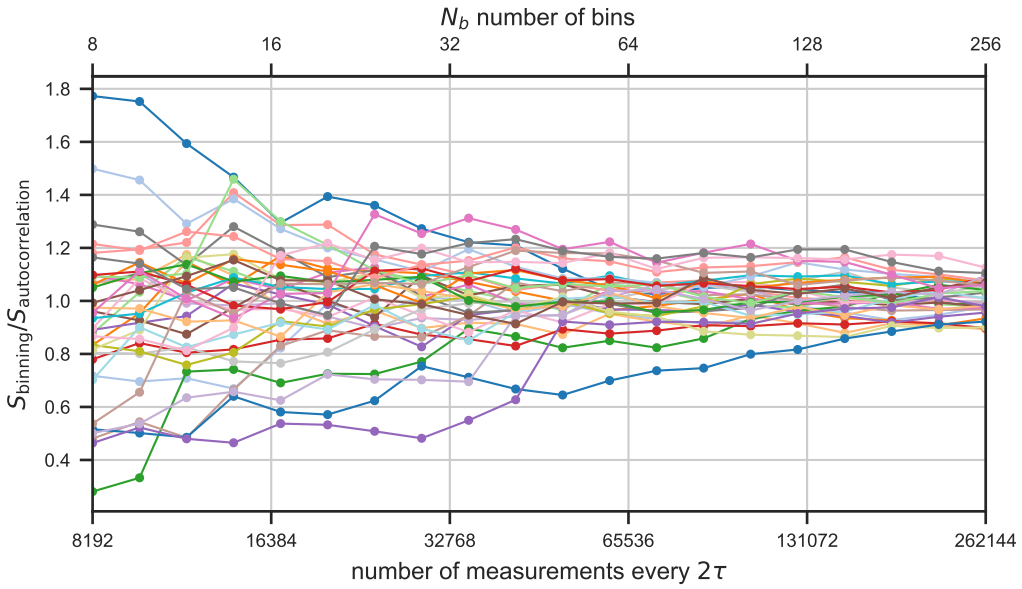

Figure 5.5: *On the x-axis one can find the number of measurements and the number of bins between these two quantities is a constant factor of* $m = 1024$ *which is bin size of for binning error estimate. The y-axis is the ratio between the error by the binning divided by the error by autocorrelation. The different lines correspond to different experiments of the* k*-components. The lines are made from a combination of* $q = 1.0, 2.0, 2.5, 3.0$ *and* $n = 256, 512, 1024, 2048, 4096, 8192$ *totalling* 24 *lines.*

based on Figure 5.6. The experiment was done for 24 Markov chains with sizes $n = 256, 512, 1024, 2048, 4096, 8192$ and weights $q = 1.0, 2.0, 2.5, 3.0$. The amount of calculated binning errors that reach the 30%-goal are 84% for $8 - 16$ bins, 92% for $16 - 32$ bins, 95% for $32 - 64$ bins, 100% for $64 - 128$ bins, 100% for $128 - 256$ bins. So at least 64 bins are required for accurate binning errors when performing measurements every 2τ, i.e. at least 65536 measurements at a rate of 2τ.

The conclusion of this analysis: autocorrelation is a very powerful tool to estimate errors and the errors are consistent with results from binning. The autocorrelation method yields more consistent results also for smaller datasets, thus reducing the computational power needed for simulations. If autocorrelation is not applicable in a situation, one could resort to binning.

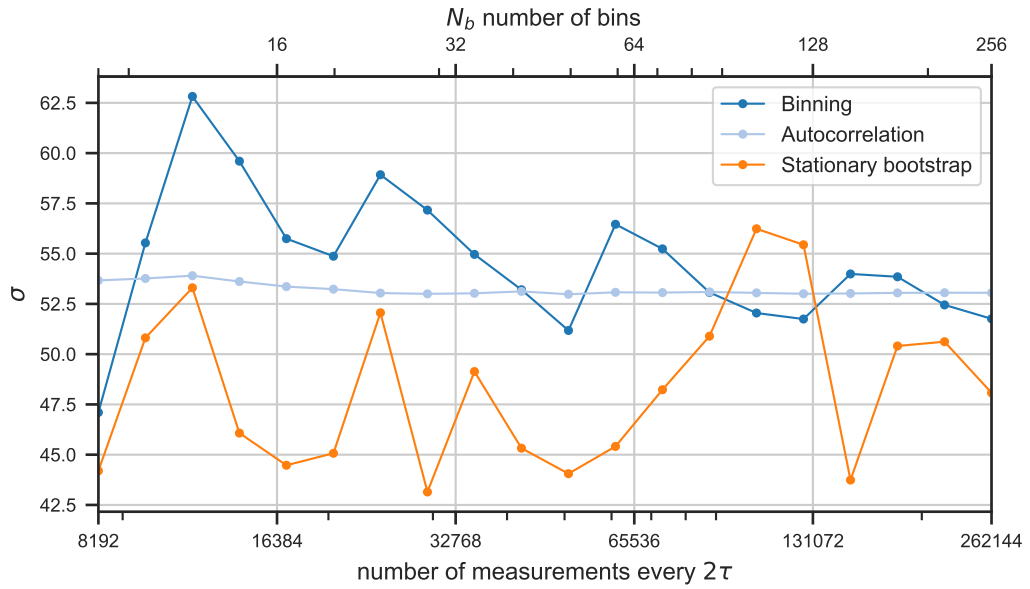

Figure 5.6: *The standard deviation, σ, versus the number of measurements every 2τ. Measurements taken of system with $n = 8192$ and $q = 1.0$. Stationary Bootstrap with $p = 0.005$ and binning with bin size $m = 1024$. The upper x-axis indicates the N_b number of bins for the "Binning" analysis.*

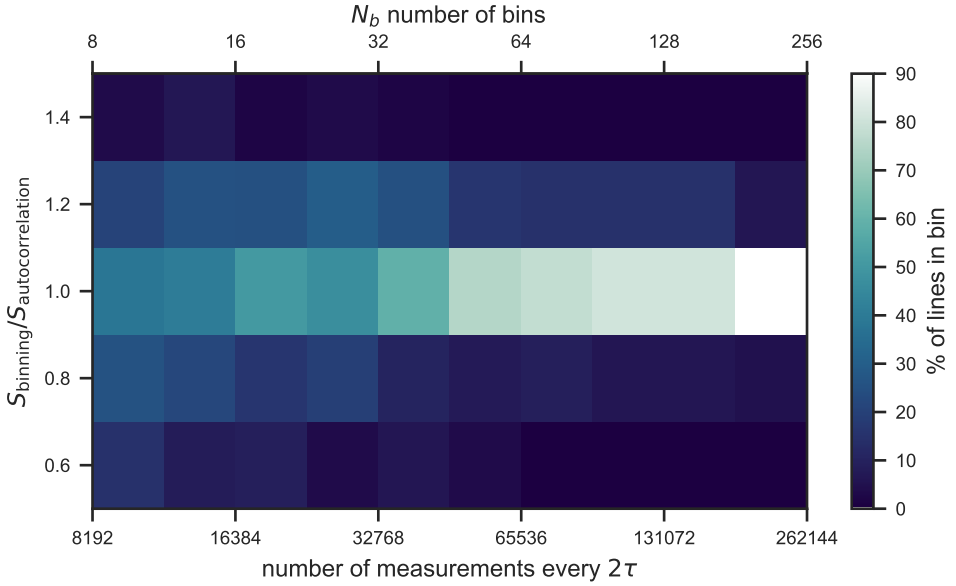

Figure 5.7: *2D-histogram of the graphs in figure 5.5. The histogram is normalized over the y-axis such that one can see the percentage error estimates within a certain factor of the autocorrelation estimate per N_b number of bins. The percentage of errors with less than 30% deviation with respect to the error estimate using autocorrelation is given by 84% for $8 - 16$ bins, 92% for $16 - 32$ bins, 95% for $32 - 64$ bins, 100% for $64 - 128$ bins, 100% for $128 - 256$ bins.*

5.1.3 Results

Figure 5.8 verifies a few expectations, for a low q $\bar{k}/n$, approaches 0 which is expected because in the limit $q \to 0$ one should recover meanders with just 1 road. For a high q, $\bar{k}/n$ is approaching 1 which is also expected, because the maximum number of roads is equal the order of the meander system, $n = k$, so $\bar{k}/n \to 1$.

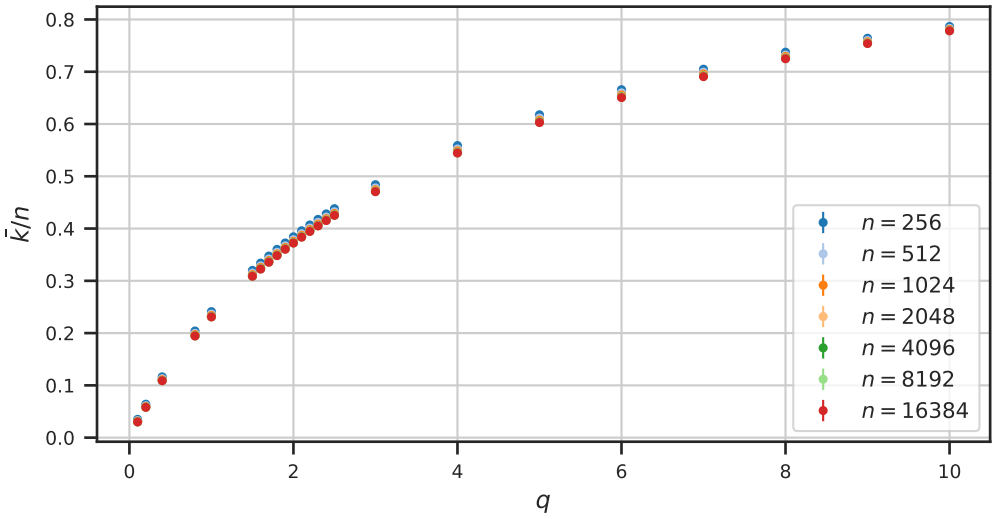

Figure 5.8: *Plot of the average number of components $\bar{k}$ normalized over n versus the weight q. The error bars are smaller than the markers and determined by binning. The parameter q is varied in steps of 0.1 around $q = 2.0$ and for the rest with a step size of $q = 1.0$.*

In Figure 5.8, it becomes clear that at $q = 2$, there is no kink for the number of components k. One can also see that there seems to be a certain bias, the higher the system size n the more $\bar{k}/n$ decreases (red below blue dots). In order to argue that this is caused by working on a discrete system the difference from the value $\bar{k}/n$ for the largest system size n_l (in this case $n_l = 262144$) is plotted in Figure 5.9. The bias decreases for $n \to \infty$.

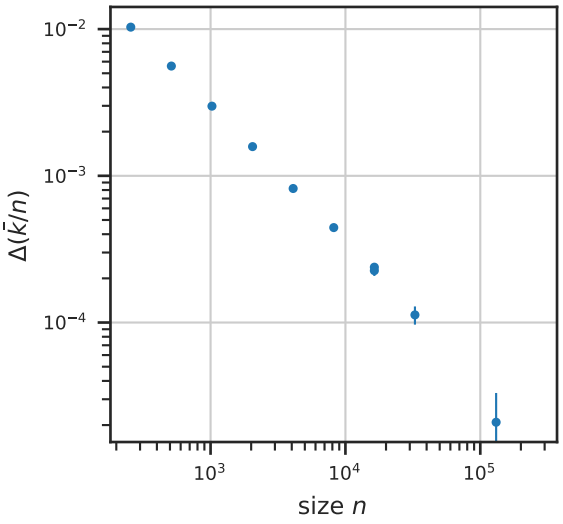

Figure 5.9: *Plot of* $\Delta(\bar{k}/n)$ *versus the size* n *where* $\Delta(\bar{k}/n)_i = \overline{k_i}/n_i - \overline{k_l}/n_l$ *and* n_l, k_l *correspond to the largest size* $n_l = 262144$.

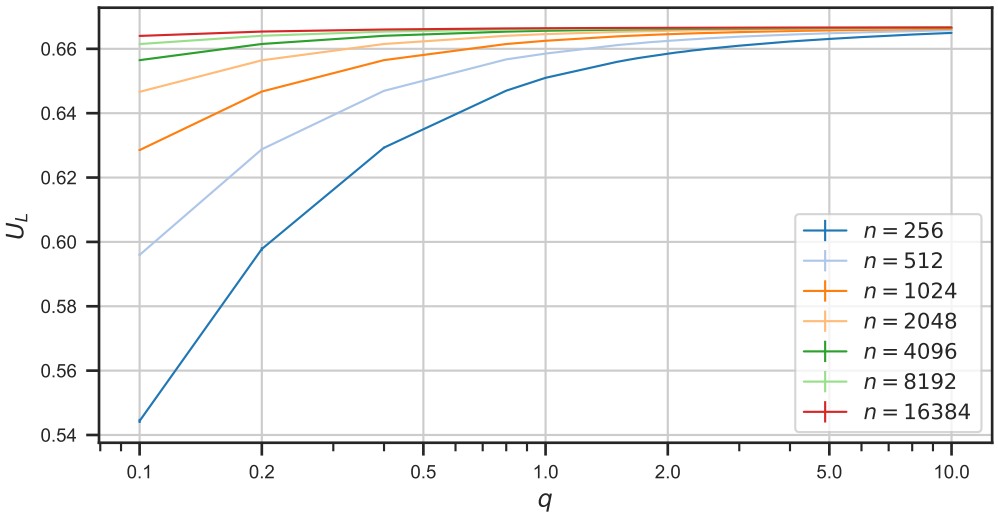

Figure 5.10: *Plot of the Binder cumulant U_L versus q. The binder cumulant is given by equation (3.31) in section 3.2. Note errors bars are determined using binning and small, most too small to see.*

Figure 5.10 does not show curves that intersect at one point for any q. This is not the expectation since $q = 2$ was expected to be the critical point of the phase transition. A binder cumulant of $2/3$ would indicate $q < q_c$. So what can explain this discrepancy?

- The Binder cumulant might not be the right method to study this kind of phase transition. The model is special because for $0 < q < 2$ there is a kind of 'constant' phase transition. Every configuration from $0 < q < 2$ is in a different universality class. For $q > 2$, the conjecture expects that there would be just one phase, the branched polymer phase.
- One might be tempted to lower q even further, that is certainly a possibility, but computationally speaking the acceptance rates of the Markov Chain Monte Carlo simulation will only decrease.

A possible explanation for not seeing a phase transition is because the number of components is a local property. It does not necessarily take into account large scale behavior. There is no direct connection to the number of roads all the way on the left in the drawing in Figure 5.11 with respect to the number of roads on the right.

The drawing in Figure 5.11 is a bit misleading because the width of the structure seems to indicate whether there is a minimum neck and thus a baby universe. Baby universes are however a property of the 2-sphere and every meander that can be taken out forms a baby universe. There are more baby universes than indicated by the outline of the drawing.

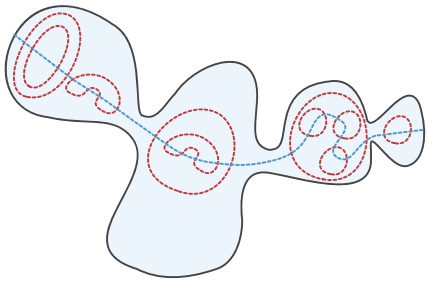

Figure 5.11: *Sketch of random surface decorated with a meander configuration*

5.2 String susceptibility

The string susceptibility was introduced in section 2.5.1. The string susceptibility can be extracted from the size distribution of baby universes. A large amount of data is required because the asymptotic (i.e. large minimum neck baby universes) of the distribution contains the most valuable information. These large baby universes in the asymptotic are however very rare. The distribution of baby universes was measured for different values of the weight q and were fitted to obtain the string susceptibility as a function of q. Histograms of the sizes of baby universes found in the Markov chain were collected to find the size distribution of baby universes. The measurement interval was taken at an interval of $128\ \tau(n,q)$ autocorrelation times, which was estimated using binning for $1 < q < 10$. The total dataset consists of 1.85 years of CPU-time. The number of independent measurements per q and system size n are given in section A.1. In the following, the measured results at $q = 1$ are first compared to the analytic results. Secondly, the numerical measurements are used to measure the string susceptibility as a function of q using an earlier derived fit function based on the distribution of baby universes around $q = 1$. Thirdly, the results of alternative fitting methods will be discussed. Lastly, the string susceptibility as a function of the weight q allows to study the phase transition conjectured at $q = 2$.

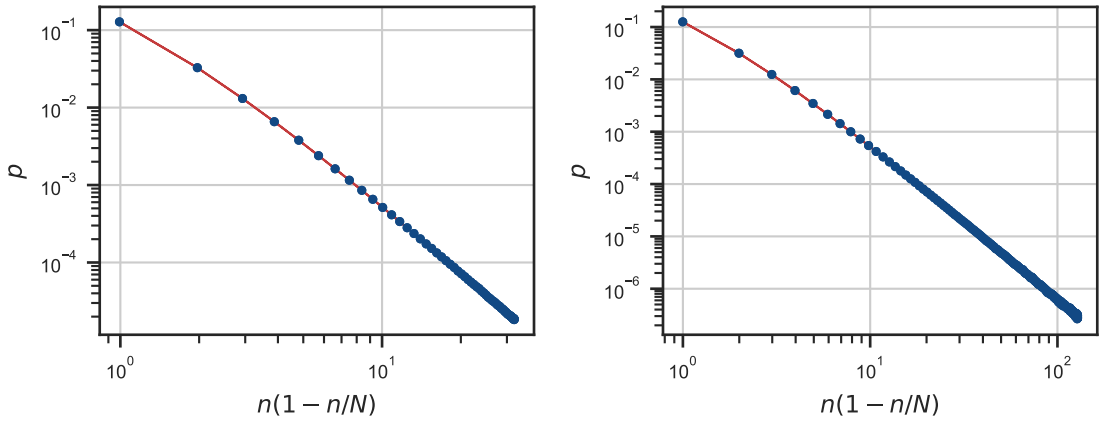

(a) (b)

Figure 5.12: *Plot of p, the probability for a meander baby universe of size n. The plots are made for (a) meanders of order $N = 128$ and (b) meanders of order $N = 512$.*

For $q = 1$, an analytic formula for the probability p of a baby universe of size n was derived as Equation (2.20) in section 2.5.1. In Figure 5.12, p is plotted as a function of $n(1-n/N)$ for two sizes $N = 128$ and $N = 512$ where n is the order of the **meander baby universe** and N is the order of the meander. Small baby universes correspond to small $n(1-n/N)$, larger baby universes correspond to large $n(1-n/N)$. The largest possible meander baby universe has order $n = N/2$. Figure 5.13, shows that large baby universes are very rare and unfortunately the probability for finding them decreases cubically with the order of the meander N.

In Figure 5.13, the analytic probability is compared to the measured data, by dividing $p_{measured}/p_{analytic}$. The x-axis is transformed as $n(1-n/N)$. The probability for the small baby universe coincides accurately. For the larger sizes the data is noisy but centered around 1. The numerically measured size distribution of baby universes at $q = 1$ therefore matches the analytic results.

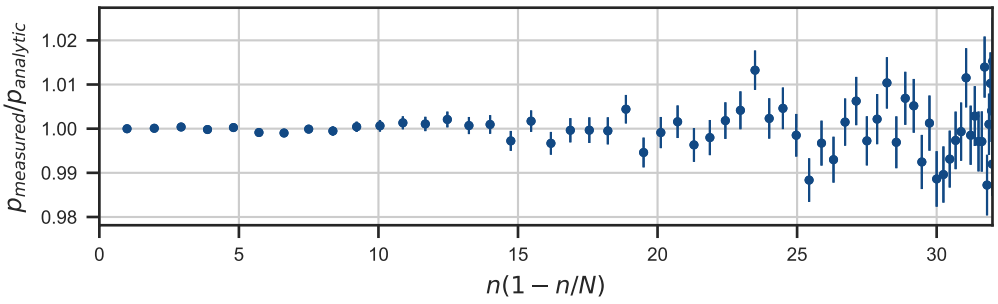

(a) $N = 128, n_{measurements} = 8.874456 \cdot 10^6$, *CPU-time* ≈ 217.2 hrs.

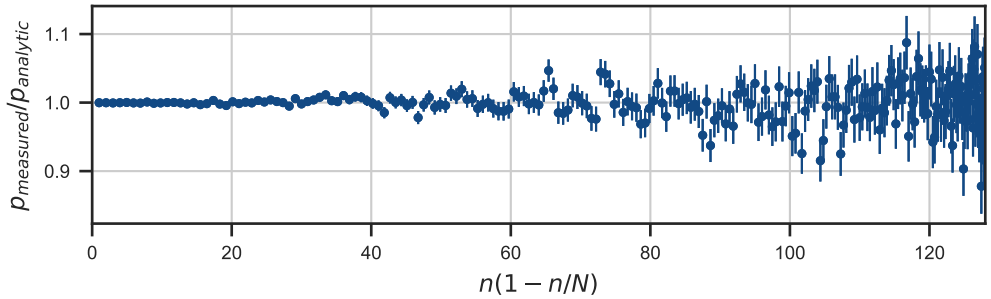

(b) $N = 512, n_{measurements} = 3.54696 \cdot 10^6$, *CPU-time* ≈ 465.3 hrs

Figure 5.13: *Comparison of measured probability to analytic probability to find a minimum neck baby universe (mimbu) of size/order n. The analytic probability is given by Equation (2.20).*

For the other values of the weight q, there is no analytic formula to compare the numerical results to. The string susceptibility can however be measured and there are several ways to do that which will be introduced in the following.

5.2.1 The approximation fitting method

In section 2.7, an approximation of the probability for a meander baby universe of size n at $q = 1$ was turned into a fit function for the string susceptibility γ_s, see Equation (2.23). The string susceptibilities obtained using this fitting method are plotted in Figure 5.14. The results at $q = 1$ are excellent. Assuming that the values of different system sizes n can be combined using a weighted average gives $\gamma_s = -0.99284 \pm 0.00022$ which is very close to the correct value $\gamma_s = -1$. This accuracy is not unexpected because the fit function is based on the analytic results for $q = 1$. The slight deviation that still exists can be attributed to systematic errors of the fitting procedure. The approximation itself introduces a systematic error since making an approximation loses information. For $1 < q < 2$ in Figure 2.23, the results clearly deviate from the conjectured relation, how can this be explained?

In order to find out, the probability for a meander baby universe of size n is fitted to numerical data to extract the string susceptibility for two different values of q. The numerical data and fits for $q = 1$ and $q = 2$ for system size $n = 512$ are plotted in Figures 5.15a and 5.15b respectively. The $q = 1$ fit yields $\gamma_s = -0.99197 \pm 0.00031$ which is similar to the expected $\gamma_s = -1.0$. For $q = 2$, the fit yields $\gamma_s = -0.5872 \pm$

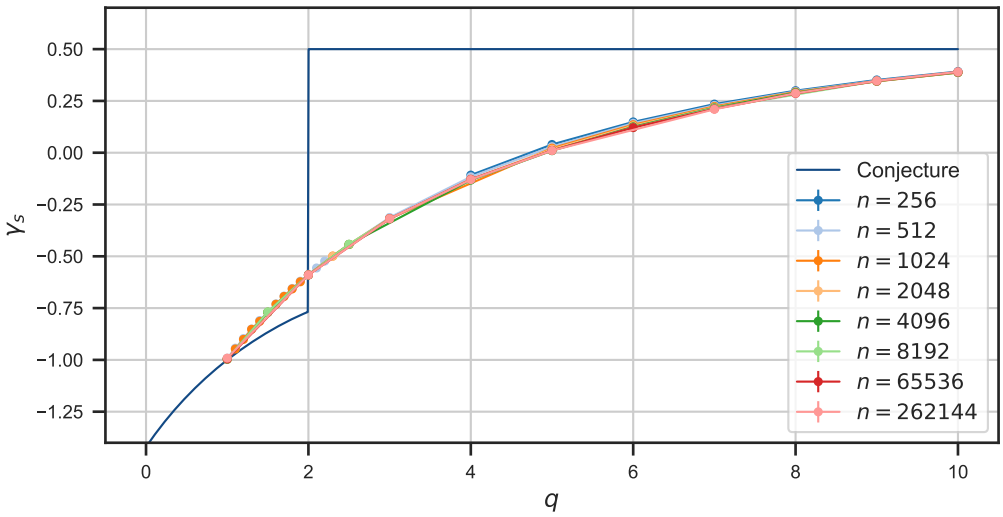

Figure 5.14: *Fitted results of the string susceptibility γ_s as a function of the weight q using the fit function given by Equation (2.23).*

0.0008 which is quite different from the conjectured $\gamma_s = -0.7676$. More precisely, for $q = 1$ the deviation is only about 0.008 where for $q = 2$ the deviation is 0.1804. The fitted string susceptibility γ_s at $q = 2$ clearly does not match with the conjecture. In Figure 5.15b, it is however visible that the fitted function for $q = 2$ does not fit the data well. The asymptotic of the fit is slightly above the asymptotic of the numerical data in Figure 5.15b. Compare that to $q = 1$ in Figure 5.15a where the fit is exactly centered in the asymptotic of the data. Thus fitting based on the approximated fit function at $q = 1$ might not be correct for different values of q.

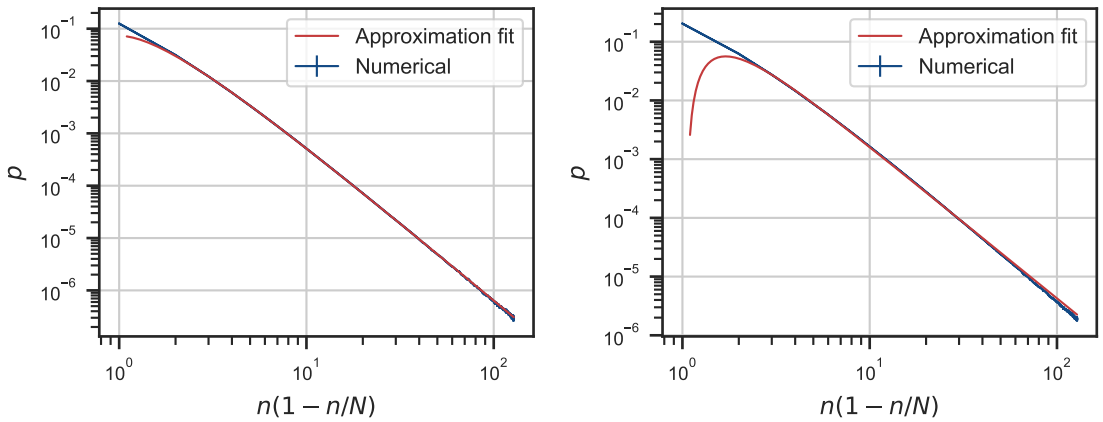

Figure 5.15: *Fitting of Equation (2.23) to p versus $n(1 - n/N)$ to extract the string susceptibility γ_s. The system size $N = 512$. (a) corresponds to $q = 1$ and (b) corresponds to $q = 2$.*

At $q = 1$ the analytic formula for the probability of a meander baby universe of size n was expanded and

turned into a fit function given by Equation (2.23) in section 2.7.

5.2.2 Linear fitting

In [23] by Ambjørn et al., two methods are introduced to fit the probability for a baby universe of size n to find the string susceptibility: a linear fit and a fit using a more sophisticated fit function. From the logarithmic p versus $(n(1-n/N))$ plots (like Figure 5.15) it is clear that the asymptotic is a straight line which will be fitted using the linear fitting method. Linear fitting itself is however inaccurate because only the asymptotic is straight, and therefore a cutoff needs to be introduced. In [23], they introduce a cutoff such that only baby universes of size $n \in [n_c, N/2]$ are used for fitting where n_c is the cutoff and $N/2$ is the maximum size baby universe.

More formally the linear method works by fitting $y = ax + b$ to the numerical data where $y = \ln p$ and $x = \ln n(1-n/N)$ where a and b are fit parameters. The slope a can be related to the string susceptibility using $\gamma_s = a + 2$, which can be derived using Equation (2.7).

The second fitting method introduced by Ambjørn et al. in [23] is by fitting the following function to the numerical data:

$$\ln(p \cdot n) = a + (\gamma_{\text{s}} - 2) \ln\left(n\left(1 - \frac{n}{N}\right)\right) + b/n \tag{5.3}$$

where a and b are fit parameters. This fit function will be called the "baby" fit[1].

In Figure 5.16, the linear, baby and the approximation fit have been plotted as a function of the cutoff n_c. The approximation-fit works very well for $q = 1$ (Figure 5.16a) but again fails for $q = 2$ (Figure 5.16b) even with cutoff. The linear and baby fit work well for both q and the linear fit converges a bit faster than the baby fit. The baby fit will therefore not be further used. For the linear and approximation fit the statistical error of the numerical data is taken into account. For the baby universe, the statistical error is not taken into account because in that case it tends to only fit well on areas with a low statistical error.

The linear fit approaches the string susceptibility for increasing cutoff n_c. The final string susceptibility can therefore be extracted by fitting the following ansatz to the results of the linear fit:

$$\gamma_{\text{s}}(n_c) = \gamma_{\text{s}} - ce^{-dn_c} \tag{5.4}$$

where c and d are fit parameters and γ_{s} is the final string susceptibility. This exponential is plotted in Figure 5.16c and yields a string susceptibility $\gamma_{\text{s}} = -0.9638 \pm 0.0019$. This method of obtaining the string susceptibility has a higher systematic error than the approximation fitting method in section 5.2.1, but it should work more accurately and reliable on all values of $1 < q < 10$. In the following, this method will be referred to as the linear+exponential method.

In Figures 5.16a and 5.16b, another fitting method was used called Random sample consensus RANSAC. RANSAC is able to get a better convergence than the linear and baby fit. It works roughly by randomly sampling what data is considered for the fit and choosing the best least-squares fit [51, 52]. The sampling removes outliers from the data. This method does however not take into account the statistical error of the data and will therefore not be used, but it might be interesting for future use.

[1] The name "baby" fit originates from the name of the article "Baby universes in 2d quantum gravity" [23] by Ambjørn et al..

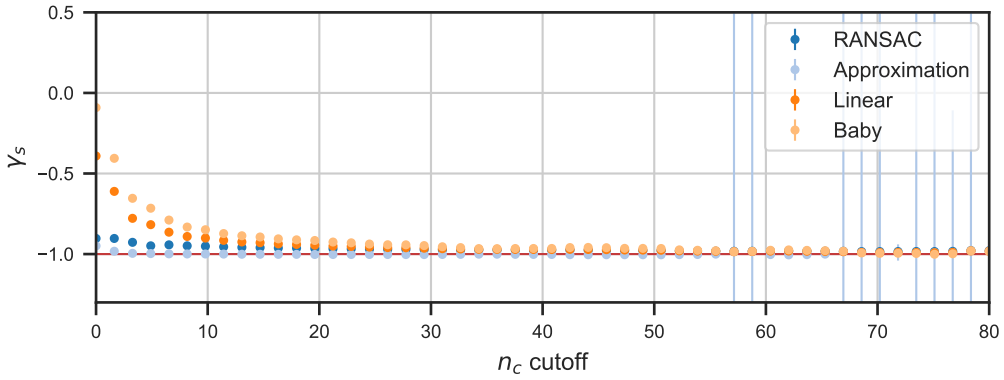

(a) $N = 512, q = 1$

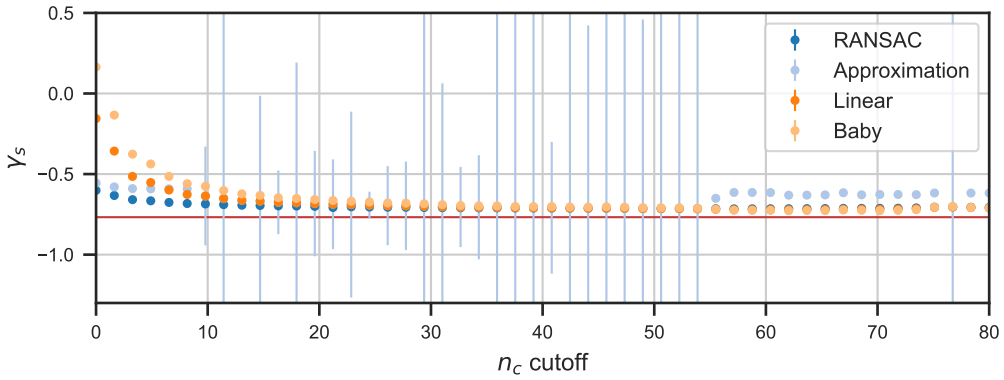

(b) $N = 512, q = 2$

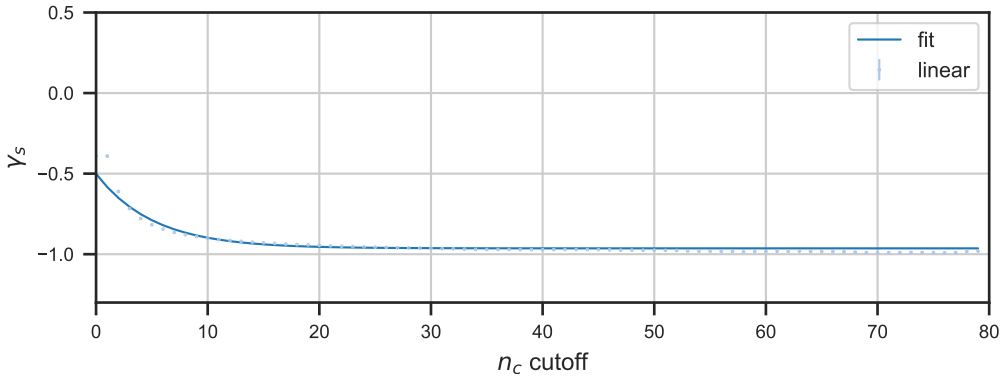

(c) $N = 512, q = 1$

Figure 5.16: *Comparison of the different fitting methods in (a) and (b) for respectively* $q = 1$ *and conjectured* $q = 0.7676$*. In (c), an exponential is fitted to the linear fit results as a function of the cutoff* n_c*. Note that the error bars in (a), (b) and (c) are determined by the covariance matrix and are often smaller than the markers.*

5.2.3 Results

In Figure 5.17, the string susceptibility is plotted as a function of q for different system sizes n. The linear+exponential method introduced in section 5.2.2 is used for the fitting with a maximum cutoff $n_c = 80$. The results in Figure 5.17 show a better correspondence to the conjectured relation between the string susceptibility and the weight q, than the results for the approximation fit in Figure 5.14.

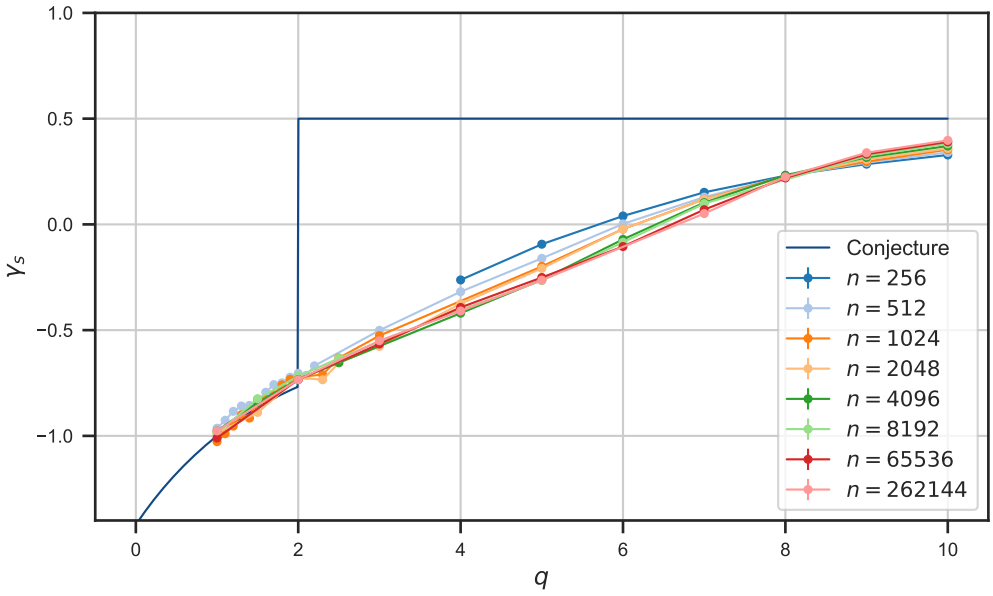

Figure 5.17: *Fitted results of the string susceptibility γ_s as a function of the weight q using linear+exponential fitting and a maximal $n_c = 80$. Errors are determined by the covariance matrix of the least-squares fit and smaller than the markers.*

At $q \approx 8.5$, the larger system sizes go from having a lower string susceptibility γ_s to having a higher string susceptibility with respect to the smaller system sizes. This location could be identified as a special point, $q_c \approx 8.5$. The region of the point q_c is cropped in Figure 5.18, where it is more clear that all the sizes exactly switch around when comparing $q = 7.0$ and $q = 9.0$.

It turns out that doing a linear fit with a set cutoff can also yield consistent results. The results for linear fitting with the cutoff set to 30 is given in Figure 5.19. The region around the point q_c is again cropped in Figure 5.20.

The correspondence of the conjectured relation between the string susceptibility and the weight q is plotted in Figures 5.17 and 5.19 by the blue line. For $1 \leq q \leq 2$, the numerical string susceptibility follows a similar shape to the conjectured string susceptibility. Approaching $q = 2$, the measure string susceptibility starts to deviate slightly. For $q > 2$, the numerical string susceptibility clearly deviates, the kink is not visible. How can this result be interpreted? The conjectures that meanders are governed by 2DQG is made in the continuum limit. Here, the conjecture is studied using discrete geometries which can cause discretization effects explaining the continuous transition from $q = 2$ to the branched polymer phase. It must however be noted that extrapolating $q \to \infty$ seems to approach the string susceptibility $\gamma_s = 1/2$ which corresponds to the branched polymer phase.

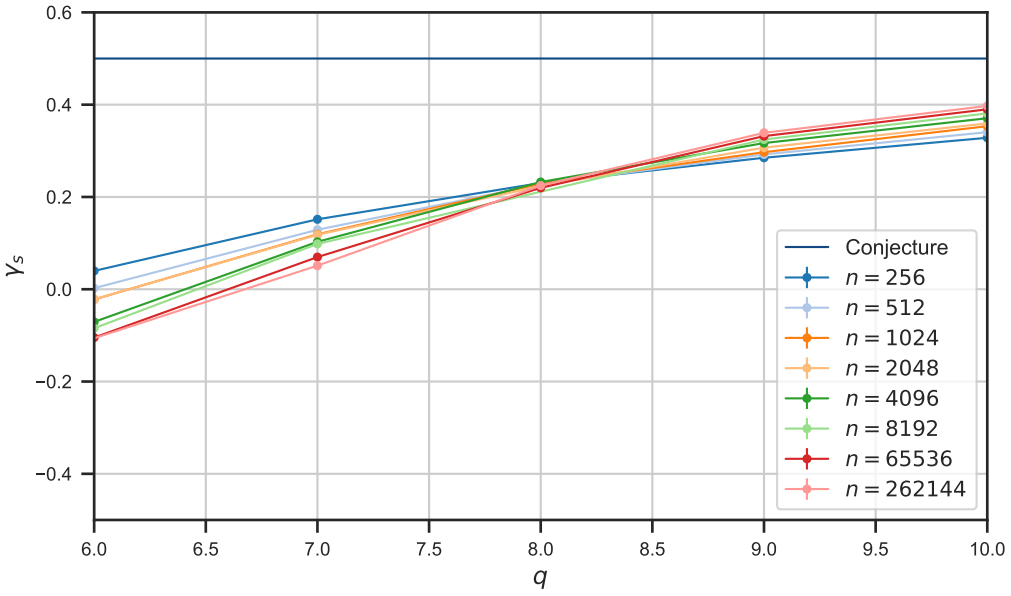

Figure 5.18: *Fitted results of the string susceptibility γ_s as a function of the weight q using linear+exponential fitting method with a maximal $n_c = 80$. Errors are determined by the covariance matrix of the least-squares fit and smaller than the markers.*

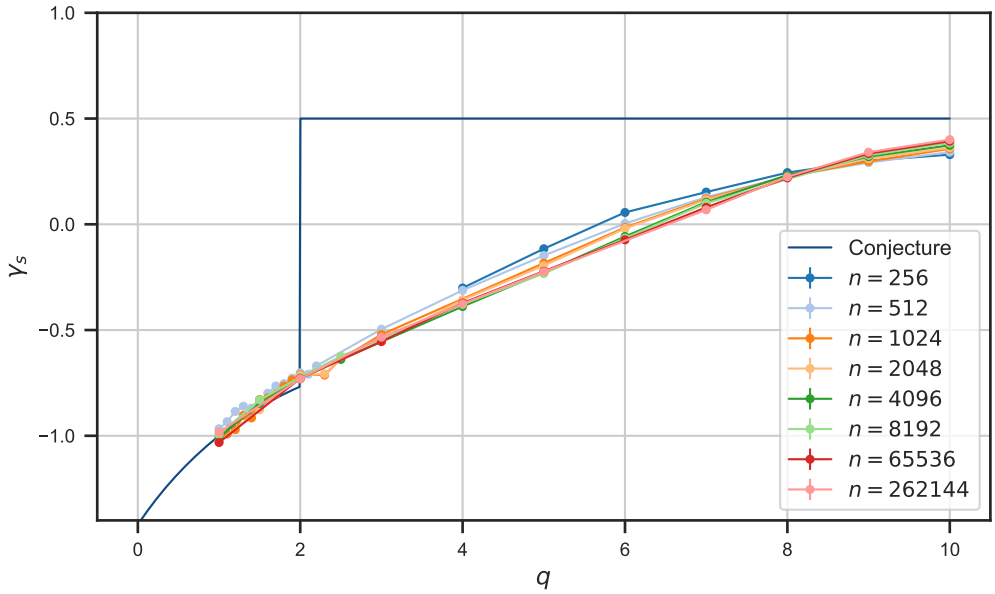

Figure 5.19: *Fitted results of the string susceptibility γ_s as a function of the weight q using linear fitting with a cutoff of 30. Errors are determined by the covariance matrix of the least-squares fit and smaller than the markers.*

This kind of smooth transition from 2DQG coupled to a CFT with $c < 1$ to branched polymers is also commonly observed in literature, for example in [53] where they measure a phase transition from $c = 1$

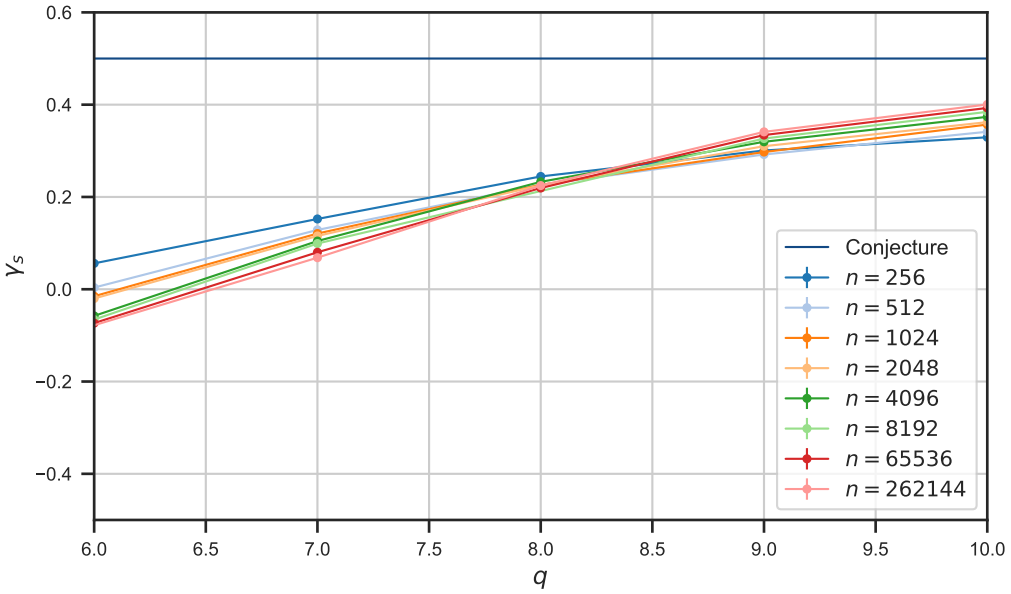

Figure 5.20: *Fitted results of the string susceptibility γ_s as a function of the weight q using linear fitting with a cutoff of 30. Errors are determined by the covariance matrix of the least-squares fit and smaller than the markers.*

to branched polymers and from $c = 0$ to branched polymers. For the meanders a phase between $c = -1$ and branched polymers is studied. It is however difficult to call it a real phase transition because for $q < 2$ the system is continuously changing phase.

Also, an explanation needs to be given for the larger system sizes having a larger string susceptibility with respect to the smaller system sizes for q higher than $q_c \approx 8.5$. The naive explanation would that for $q < q_c$, the fits approaches the string susceptibility of the phase at $q = 2$, and for $q > q_c$ one could say that the fits approach the string susceptibility γ_s of the branched polymer phase $\gamma_s = 1/2$. The reality is however probably more complex. One could make a very rough approximation of the probability p for a meander baby universe of size n by

$$p \sim n^{\gamma_s - 2} \left(1 + \left(\frac{n}{N_1(q)}\right)^{-\delta_1}\right) \tag{5.5}$$

where n refers to the total system size and $N_1(q)$ is a system size dependent on q. For $n < N_1(q)$, δ_1 will be added to the string susceptibility resulting in an effective string susceptibility $\gamma_s^{\text{effective}} \approx \gamma_s + \delta_1$. For $n > N_1(q)$, the string susceptibility will be equal to $\gamma_s^{\text{effective}} \approx \gamma_s$. The assumption in Equation (5.5) says that the string susceptibility should only increase or decrease at a set q when the system size is varied. To explain the results seen around $q_c \approx 8.5$ higher order corrections are required.

In [1], Di Francesco et al. report that their numerical results get worse when approaching $q = 2$ from below. They measured a string susceptibility higher than expected. In Figure 5.21, the results for the string susceptibility at $q = 2$ are plotted using the linear fitting with cutoff $n_c = 30$ and linear+exponential method with $n_c = 80$. Here like in [1], the string susceptibility is higher than the conjectured value. The values for the string susceptibility γ_s seem to approach the conjectured value for larger system sizes n. The linear fitting method has a systematic error that can be reduced by increasing the cutoff, however for increasing the cutoff more numerical data is required.

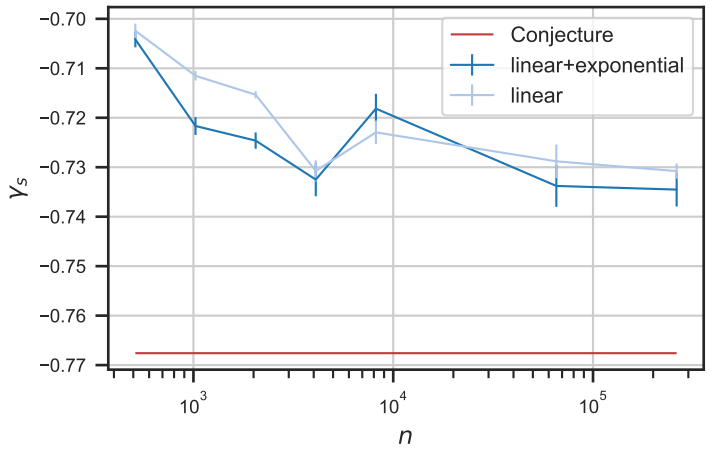

Figure 5.21: *Fitted results of the string susceptibility γ_s at $q = 2$ using linear fitting with cutoff $n_c = 30$ and linear+exponential method with $n_c = 80$. The errors are determined using the least squares covariance matrix.*

5.3 Hausdorff dimension

The Hausdorff dimension describes the dimension of a geometry, and it was first introduced in section 2.5.1. In Figure 2.20 the conjectured dependence of d_H on the weight q was plotted[2]. In the following, numerical evidence will be presented to support this conjecture. The Hausdorff complements the stringsusceptibility as an observable because it is computationally less expensive to measure for a lower $q \in [0, 2]$ where the string susceptibility γ_s is easier to measure for a higher $q \in [0, 2]$. The string susceptibility is therefore measured for $q \in [1, 2]$. The Hausdorff dimension will be used to study $q \in [0, 1]$.

5.3.1 Setup

The Hausdorff dimension has been measured for two values, $q = 0.2$ and $q = 1$. The Hausdorff dimension at $q = 1$ allows to check the overall validity of the simulations and compare to other Hausdorff dimension measurements like in [20] by Barkley and Budd. The simulations take about $1/q$ longer when below $q < 1$, therefore $q = 0.2$ was chosen as a compromise between the computational power required and approaching the meanders with just one road for which $q \to 0$.

Measuring the Hausdorff dimension is performed by measuring the distance profile of geometries produced by the Markov chain Monte Carlo simulation. The distance profile is the probability $\rho(r)$ to find an edge or face at a distance r. One can measure distance traversing the edges which is called the graph distance or the distance traversing the faces which is called the dual graph distance. The two types of distances are visualised in Figure 5.22. Both graph and dual graph distances have been measured.

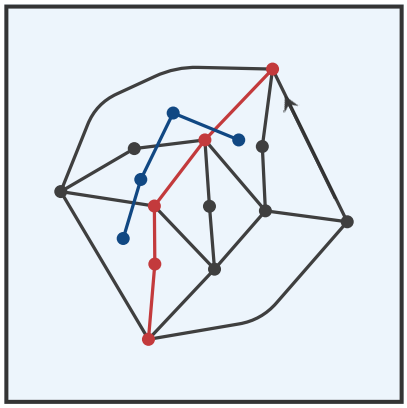

Figure 5.22: *The dual graph distance traverses faces and is displayed in blue. The graph distance traverses edges and is displayed in red.*

The distance profiles are taken from a certain randomly picked origin face or edge which results in very fluctuant distance profiles. This can be reduced by measuring the distance profile from multiple random points in the geometry. The sample rate, n_{samples}, defines how many times the distance profile is measured. Here the sample rate is put to $n_{\text{samples}} = \frac{n}{16}$ which translates to approximately $0.2\% - 80\%$ CPU-time on measuring for respectively $n = 128$ and $n = 131072$ for $q = 1$. Spending 80% CPU-time measuring is not optimal, but for all the other sizes the percentage is below 50%.

[2] The Hausdorff dimension is calculated using the conjectured Ding and Gwynne formula which depends on the Liouville coupling constant γ.

For $q = 1$, a total of 11520 independent measurements were taken at an interval of 512 sweeps. The interval of 512 sweeps was determined by doing a binning analysis and determining the minimal bin size m for independent measurements. The 11520 independent measurements consist of 720 Markov chains with different seeds. The 11520 independent measurements are split up into 10 batches with 1152 measurements. In every batch the statistical error of the distance profile is calculated using the standard error. The maximum measured system size is $n = 131072$. The simulations are worth 1.15 years of CPU-time for $q = 1$.

For $q = 0.2$, a total 2304 measurements were taken at a rate of 2048 sweeps, also determined by performing a binning analysis. The 2304 measurements consisted of 144 Markov chains. The maximum measured system size is $n = 32768$. The total dataset is divided up into 9 batches and is worth 22.3 days of CPU-time.

5.3.2 Finite-size scaling

Finite-size scaling can be used to estimate critical exponents. Finite-size scaling measures the scaling of r as a function of N by rescaling the distance profile [13]. Here finite-size scaling will be used to extract the Hausdorff dimension from the distance profiles. The distance profile of a system of size n is denoted by $\rho_n(r)$. The distance profiles of size n can be rescaled as

$$\lim_{n\to\infty} n^{1/d_H}\rho_n(xn^{1/d_H}) = \rho(x) \tag{5.6}$$

which is assumed to converge to $\rho(x)$ for $n \to \infty$ and $x > 0$ [20]. In other words, the distance profiles should overlap which they do for the correct Hausdorff dimension d_H.

The ideal way to perform this finite-size scaling and collapse the distance profiles is described by Barkley and Budd in [20]. Collapsing the distances profiles is performed by fitting distance profiles $\rho_n(r)$ of different sizes n to the largest distance profile $\rho_{n_0}(r)$ of size n_0. This corresponds to taking the function $x \to k_n\rho_n(k_n^{-1}x)$ and fitting it to the function $x \to \rho_{n_0}(x)$. The tails of the distance profiles are cut off by $\rho_n(r) \geq 1/5 \max \rho_n(r)$ because they are influenced by discretization effects [20].

Practically speaking, the distance profile $\rho_{n_0}(r)$ are interpolated linearly. The datasets of the distance profiles consist of $\mathbf{x}^\star = (x_1, x_2, \ldots, x_n)$, and $\rho_n = (\rho_n(x_1), \rho_n(x_2), \ldots, \rho_n(x_n))$. The datasets describe the function $x^\star \to \rho_n(x^\star)$. For the collapse the $\mathbf{x}^\star$ will be rescaled and the values of the new $\mathbf{x}$ are then given by: $x_i k_n^{-1} = x_i^\star$ which yields $x_i = x_i^\star k_n$. So $\mathbf{x}$ will be equivalent to changing the datasets to $\mathbf{x} = x_1k_n, x_2k_n, \ldots, x_nk_n$. The distance profiles will be rescaled to $\rho_n' = (k_n\rho_n'(x_1), k_n\rho_n'(x_2), \ldots, k_n\rho_n'(x_n))$. Also, the statistical error $S_{\rho_n}(r)$ of the distance profiles is taken into account for the collapsing.

To improve the accuracy of the collapse, a shift $s \in \mathbb{R}$ can be introduced by

$$\lim_{n\to\infty} n^{1/d_H}\rho_n(xn^{1/d_H} - s) = \rho(x) \tag{5.7}$$

which will still yield correct finite-size scaling results [20]. Firstly, the shift s_n must be determined which can be done by taking the function $x \to k_n\rho_n(k_n^{-1}(x + s_n) - s_n)$ and fitting it to the function $x \to \rho_{n_0}(x)$. The shift s can be determined by the weighted average of the fitted values of s_n [20]. Using the shift s, k_n can be determined by fitting $x \to k_n\rho_n(k_n^{-1}(x + s) - s)$ to $x \to \rho_{n_0}(x)$ [20, 22].

An estimate for the Hausdorff dimension is given by [20]

$$d_H(n) = \frac{\log(n_0/n)}{(k_n/k_{n_0})} \tag{5.8}$$

The Hausdorff dimension can be more accurately determined by fitting k_n to the following ansatz

$$k_n \approx \left(\frac{n}{n_0}\right)^{-\frac{1}{d_H}} \left(a + b\left(\frac{n}{n_0}\right)^{-\delta}\right) \tag{5.9}$$

where a and b are fit parameters with $a \approx 1$, $|b| \ll 0$ and $\delta > 0$ [20, 22].

5.3.3 Results

In Figure 5.23, the results of measuring the Hausdorff dimension for $q = 1$ **without** shift s are plotted as a function of the system size n. Equation (5.8) is used to calculate $d_H(n)$ in Figure 5.23 from the fitted k_n. The errors are determined by jackknife by using 10 batches. The predicted Hausdorff dimension by the Ding and Gwynne formula (see Equation (2.12)) is equal to $d_H = 3.58$ and drawn with the dashed line in Figure 5.23. The measured Hausdorff dimension by dual graph distance and graph distance approach the predicted value as the system size n increases. It is however clear that a larger system size is required to find out to what value the estimates approach. By fitting Equation (5.9), the Hausdorff dimension was further determined to be for the $d_H = 3.331 \pm 0.016$ dual graph distance and $d_H = 3.290 \pm 0.011$ for the graph distance. The raw fit results can be found in Table A.11 for the dual graph distance and in Table A.12 for the graph distance. In Figure 5.24, the collapsed distance profiles of the graph and dual graph distance are plotted for the fitted Hausdorff dimensions.

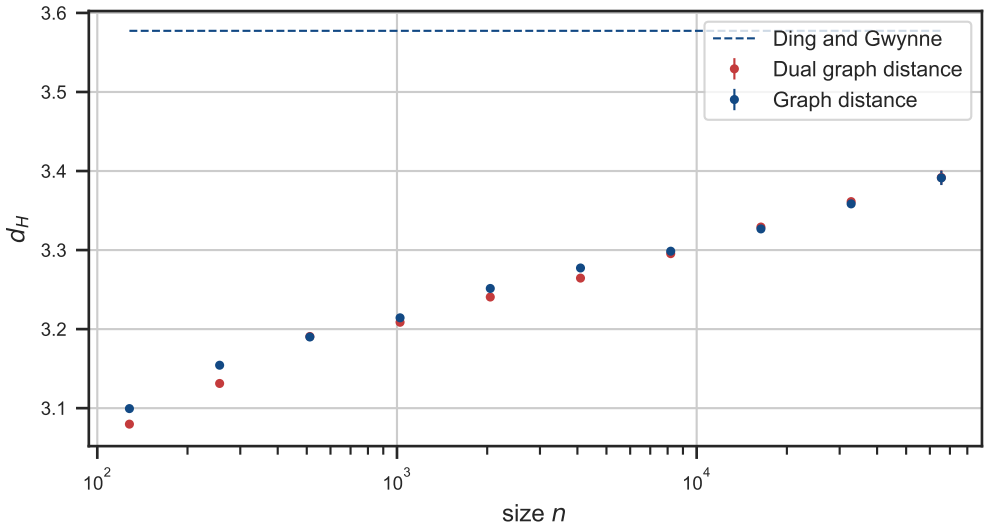

Figure 5.23: *Measuring the Hausdorff dimension d_H at $q = 1$. The expected Hausdorff dimension is $d_H = 3.58$ by Ding and Gwynne.*

Introducing the shift s changes the results significantly. The determined values for the shift s at $q = 1$ are $s = 3.297$ for the dual graph distance and $s = 5.229$ for the graph distance. Fitting using the shift s yields

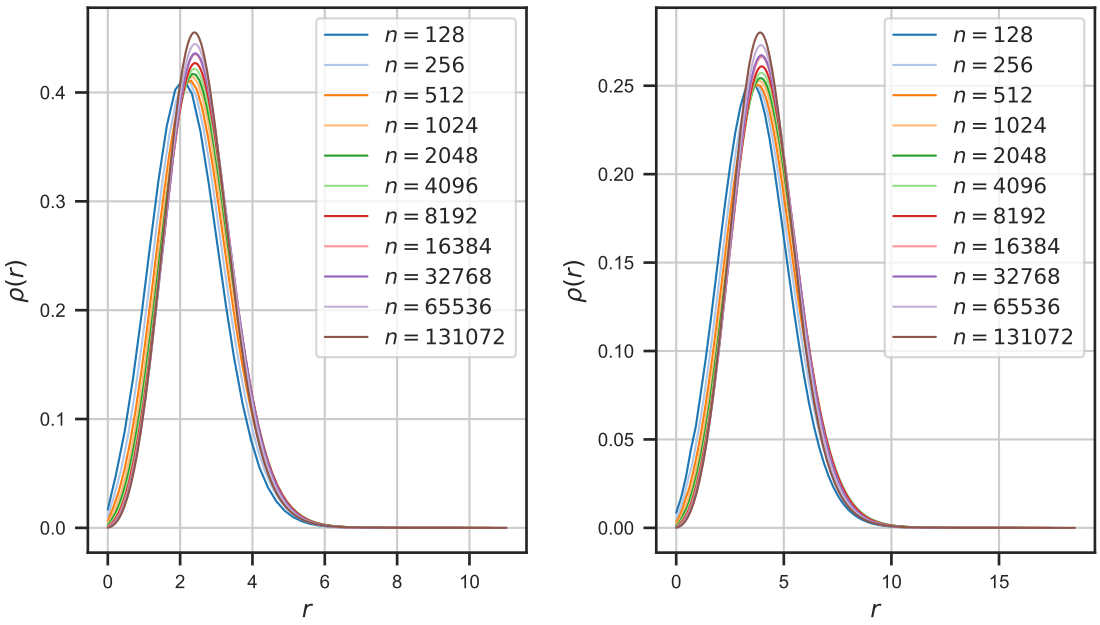

(a) (b)

Figure 5.24: *Finite-size scaling of the dual graph distance and graph distance with Hausdorff dimensions determined from fitting with Equation (5.9). The used Hausdorff dimensions are* $d_H = 3.331 \pm 0.016$ *for the dual graph distance and* $d_H = 3.290 \pm 0.011$ *for the graph distance.*

the results in Figure 5.25 where again the errors have been determined using jackknife and the Hausdorff dimension is calculated using Equation (5.8).

The results in Figure 5.25 are more accurate than without the shift and even coincide with the predicted Hausdorff dimension by the Ding and Gwynne formula (see Equation (2.12)). The Watabiki formula for the Hausdorff dimension is also plotted. The Watabiki formula is an older conjectured relation between the Liouville coupling constant γ and the Hausdorff dimension that was contradicted by numerical simulations in [20]. The dual graph distance and graph distance seem to favour the Ding and Gwynne formula for larger system sizes, but the statistical error is too large to make any hard conclusions.

Fitting using the ansatz Equation (5.9) yields for the dual graph distance $d_H = 3.5598 \pm 0.0028$ and for the graph distance $d_H = 3.540 \pm 0.006$. The statistical error on these values is determined by jackknifing and fits with a statistical error larger than 1 on the Hausdorff dimension were removed. The removed fits also do not respect the $a \approx 1, |b| \ll 0$ of the ansatz. The full fit information can be found in Table A.13 for the dual graph distance and in Table A.14 for the graph distance. The collapsed distance profiles for the measured Hausdorff dimensions can be found in Figure 5.26. Lastly, the values determined using these fits are in the range of $3.54 - 3.56$ which is lower than the conjectured values of the Hausdorff dimension of $d_H = 3.58$. By looking at Figure 5.25 however, it seems reasonable that when the simulations are extended to larger system sizes the Hausdorff dimension will converge to the conjectured value at $q = 1$.

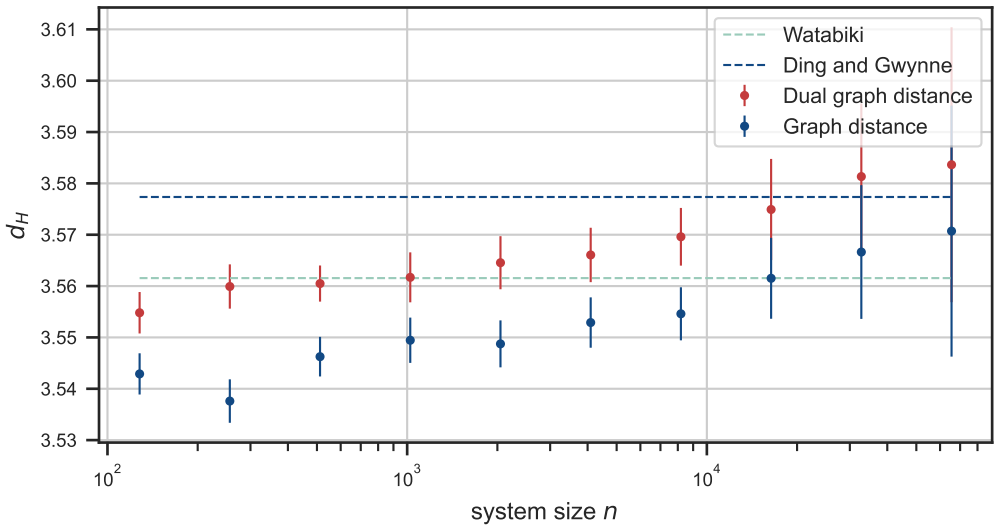

Figure 5.25: *Plot of the Hausdorff dimension at $q = 1$ calculated with Equation (5.8) for the finite-size scaling with shift s. The statistical errors are calculated by jackknifing 10 batches.*

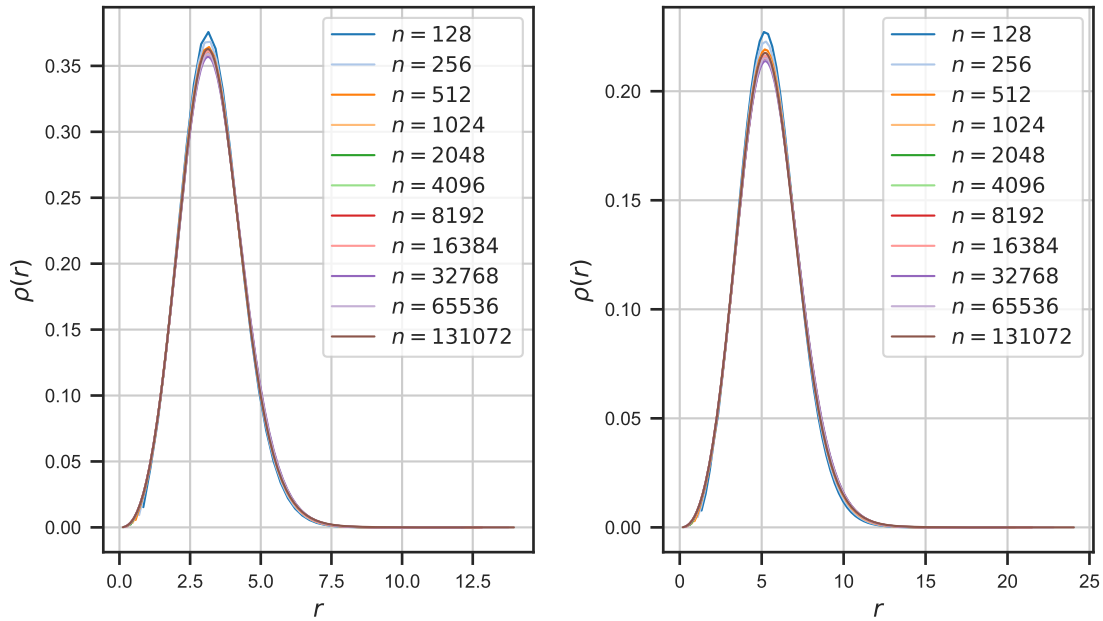

(a) (b)

Figure 5.26: *Finite-size scaling of the dual graph distance and graph distance with Hausdorff dimensions determined from fitting with (5.9). The used Hausdorff dimensions are $d_H = 3.5598 \pm 0.0028$ for the dual graph distance and $d_H = 3.540 \pm 0.006$ for the graph distance.*

For $q = 0.2$, the results are displayed in Figure 6.1. The maximum system size used for $q = 0.2$ is $n_0 = 32768$ in comparison to $n = 131072$ for $q = 1$. The statistical errors on have been determined by jackknifing. The fit results of Equation (5.9), for the Hausdorff dimension are $d_H = 3.3394 \pm 0.0024$ for the dual graph distance and $d_H = 3.355 \pm 0.019$ for the graph distance. This is again lower than the expected Hausdorff dimension of $d_H \approx 3.40$, but considering Figure 6.1 the estimates for the Hausdorff dimension could certainly approach the conjectured value of $d_H \approx 3.40$ for larger system sizes.

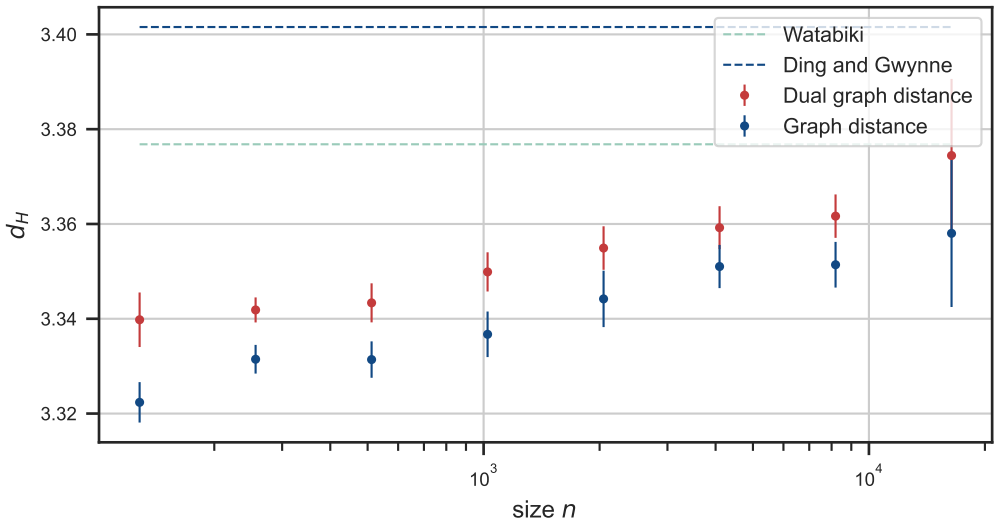

Figure 5.27: *Plot of the Hausdorff dimension at $q = 0.2$ calculated with Equation (5.8) for the finite-size scaling with shift s. The statistical errors are calculated by jackknifing 9 batches.*

In Figure 5.28, a summary is given of all the results of the Hausdorff and string susceptibility measurements.

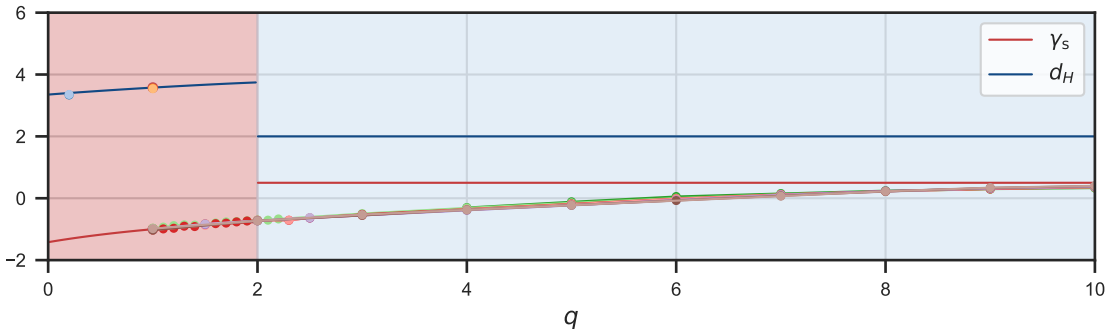

Figure 5.28: *Summary of the results of the Hausdorff dimension d_H from section 5.3 and string susceptibility γ_s from section 5.2. The lines indicate the conjectures values of the Hausdorff dimension and string susceptibility.*

CHAPTER 6

Conclusions and outlook

A discrete surface can be built based on a meander configuration and Di Francesco et al. conjectured that in the continuum limit these discrete surfaces are two-dimensional quantum gravity (2DQG). The main research question was, is there numerical evidence that verifies or falsifies this? Predictions about the string susceptibility and Hausdorff dimension conjecture have been checked using numerical evidence. Additionally, the expected phase transition for $q > 2$ has also been studied.

To check the conjectured relations Markov chain Monte Carlo techniques were used to sample geometries built by meander configurations. The sampling can be controlled by the weight q which is the weight assigned to the roads. The number of roads, string susceptibility and Hausdorff dimension of the sampled geometries have been measured as a function of the weight q.

The number of roads/components k was studied as an order parameter for the expected phase transition for $q > 2$. The number of roads k as a function of q was however smooth for all measured sizes. The analysis using Binder cumulant of the number of roads did not show any signs of a phase transition. A possible explanation for this might be that the number of roads is not a good order parameter. In conclusion, no phase transition was measured when using the number of components as an order parameter.

Measuring the string susceptibility was more fruitful. The measurements matched the analytic results for the string susceptibility at $q = 1$. The string susceptibility was fitted using several methods. Fitting based on an approximation of the analytic result at $q = 1$ gave good results at $q = 1$ for the string susceptibility but poor results for other values of q. Fitting using the linear fitting methods worked best and uses the least amount of assumptions which results in more reliable string susceptibility measurements. Between $1 < q < 2$ the string susceptibility seemed to follow the predicted curve. When approaching $q = 2$ however, the numerical string susceptibility seemed to favour a slightly higher string susceptibility than predicted. The same was reported in [1] by Di Francesco et al. The deviation can be attributed to discretization effects and/or it could be a flaw of the fitting method. The conjecture could also be wrong for $q = 2$ but more numerically evidence at $q = 2$ is required to test that. Extrapolating the string susceptibility for $q \to \infty$, the string susceptibility approaches $\gamma_{\mathrm{s}} = 1/2$ which corresponds to the predicted branched polymer phase. A more sharp transition

was predicted. The conjecture holds however for the continuum limit, studying it with discrete geometry can be a possible cause for not seeing a sharp transition to branched polymers. The smooth instead of sharp transition is therefore attributed to discretization effects.

The Hausdorff dimension at $q = 1$ was measured and matches well with the expected Hausdorff dimension for $q = 1$. The data might even seem to favour the Ding and Gwynne formula for the larger system sizes but no hard conclusions can be made because the statistical error is too high. At $q = 0.2$, the measured Hausdorff dimensions seemed to approach the expected Hausdorff dimension, but larger system sizes are required to verify this claim. It must however be noted that for larger system sizes the Hausdorff dimension could also approach to a value just below the predicted Hausdorff dimension which would mean that the predicted Hausdorff dimension is wrong.

In conclusion, studying quadrangulations decorated with meanders using Markov Chain Monte Carlo simulations and the developed flip move based on the Metropolis-Hastings algorithm resulted in new numerical evidence for larger meander systems than studied in the past. The new numerical data for larger system sizes largely supports the conjecture for $0.2 \leq q \leq 2$ and no big differences with results at smaller size systems have been found. Meanders can thus most likely be used to study statistical systems with a central charge $c \in [-4, -1]$ coupled to 2DQG. For $q > 2$, no sharp transition is found which shows that very large geometries ($n \gg 262144$) might be required to see a sharp transition.

And the next time you look at a very long meandering river, you might actually be looking at two-dimensional quantum gravity!

Outlook

Further numerical evidence can be collected in the future by extending the measurements to more values of q, in particular for the Hausdorff dimension for $q < 1$. Also, larger system sizes should be measured. This is however computationally expensive. In the future, other Markov chain Monte Carlo moves like exchanging baby universes could be introduced to reduce the autocorrelation time and therefore speed up the simulations [54].

The quadrangulations decorated with meanders are an interesting system which with enough computational resources might even be used to study the conjectured relations between the Hausdorff dimension and string susceptibility, like the Ding and Gwynne formula.

For future research, multi-river systems could be considered. This is conjectured to allow, studying CFTs coupled to gravity with different central charges between $c = -4$ and $c = 1$. When the weight for the rivers is set to $q_1 = 1$ and the weight of the roads set to $q_2 = n$, one can study the $O(n)$ loop model coupled to 2DQG [1]. The flip move can be extended easily to multi-river systems, however, keeping the algorithm $O(\log n)$ might be difficult.

The string susceptibility can be fitted using different fitting methods that are tailor-made to find just the linear parts of a fit, in section 5.2.2 RANSAC was tried which gave good results in comparison to linear fitting. In the future, RANSAC-like approaches could be tried for obtaining the string susceptibility using a fit of the probability of meander baby universes. Furthermore, a different method for measuring the string susceptibility could be used based on the method described in [45] by Golinelli. For that, the Markov chain Monte Carlo simulation would need to be changed to a grand canonical ensemble, so different system sizes can be found in the Markov chain.

Acknowledgements

I want to thank Timothy Budd for being my supervisor during my bachelor internship and being always open for questions. I enjoyed working in the field of two-dimensional quantum gravity which is on the verge of statistical mechanics, mathematics, quantum mechanics and gravity.

From May 1st till May 7th 2022, I visited the Theory group of the University of Pisa and I want to thank Timothy Budd and Massimo D'Elia for making this trip possible. The trip was sponsored by the Honours Programme Science of the Radboud University Faculty of Science.

In Pisa, I gave a talk about my bachelor internship and discussed parts of it with PhD students there. I want to thank Mohamed Aghaie Moghadam Ozbak, Giovanni Armando, Gregorio Paci, Dario Sauro, Lorenzo Maio, Manuel Naviglio and Giulia Piccitto and the others for warmly inviting me in the department and introducing me to the city of Pisa.

I also want to thank the members of the Timothy Budd research group for asking critical questions and sharing interesting ideas.

Have a look at the website of the Pisa Theory Group.

Figure 6.1: *Picture of the Leaning Tower of Pisa taken May 7th 2022.*

APPENDIX A

Tables

A.1 Practical information on string susceptibility measurements

Table A.1: *Practical data on string susceptibility measurements, number of independent measurements and total time (hours) measuring at* $q = 1$.

n	$n_{\text{independent}}$	total time (hours)
512	3546960	465.5
1024	114688	33.3
2048	16384	8.5
4096	16384	20.8
8192	16384	66.6
65536	1280	53.7
262144	1664	321.0

Table A.2: *Practical data on string susceptibility measurements, number of independent measurements and total time (hours) measuring at* $q = 2$.

n	$n_{\text{independent}}$	total time (hours)
512	1130912	260.4
1024	1183744	420.9
2048	1015808	730.7
4096	34816	71.1
8192	16384	91.3
65536	1280	77.2
262144	1624	499.1

Table A.3: *Practical data on string susceptibility measurements, number of independent measurements and total time (hours) measuring at* $q = 3$.

n	$n_{\text{independent}}$	total time (hours)
512	249152	149.3
1024	16384	8.9
2048	16384	18.5
8192	12288	89.8
65536	1280	106.1
262144	1520	608.2

Table A.4: *Practical data on string susceptibility measurements, number of independent measurements and total time (hours) measuring at* $q = 4$.

n	$n_{\text{independent}}$	total time (hours)
256	16384	2.3
512	163536	87.4
2048	20480	31.4
4096	4096	13.2
8192	4096	38.3
65536	1280	130.9
262144	1504	871.1

Table A.5: *Practical data on string susceptibility measurements, number of independent measurements and total time (hours) measuring at* $q = 5$.

n	$n_{\text{independent}}$	total time (hours)
256	16384	2.8
512	65536	27.9
1024	16384	12.4
2048	4096	7.6
4096	4096	16.3
8192	4096	52.1
65536	1136	160.4
262144	1472	1005.3

Table A.6: *Practical data on string susceptibility measurements, number of independent measurements and total time (hours) measuring at* $q = 6$.

n	$n_{\text{independent}}$	total time (hours)
256	16384	3.2
512	73728	36.6
1024	24576	26.0
2048	4096	10.1
4096	4096	22.0
8192	4096	60.4
65536	1136	180.4

Table A.7: *Practical data on string susceptibility measurements, number of independent measurements and total time (hours) measuring at* $q = 7$.

n	$n_{\text{independent}}$	total time (hours)
256	16384	3.9
512	73728	42.6
1024	24576	28.2
2048	4096	10.1
4096	4096	25.4
8192	4096	80.3
65536	1184	254.4
262144	1240	1354.5

Table A.8: *Practical data on string susceptibility measurements, number of independent measurements and total time (hours) measuring at* $q = 8$.

n	$n_{\text{independent}}$	total time (hours)
256	16384	4.1
512	70656	51.8
1024	24576	32.1
2048	4096	13.8
4096	4096	29.9
65536	1168	281.4
262144	1152	1463.6

Table A.9: *Practical data on string susceptibility measurements, number of independent measurements and total time (hours) measuring at* $q = 9$.

n	$n_{\text{independent}}$	total time (hours)
256	16384	5.9
512	70656	52.7
1024	24576	31.0
2048	4096	14.6
4096	4096	33.7
8192	3200	83.5
65536	1216	434.3
262144	1112	1456.9

Table A.10: *Practical data on string susceptibility measurements, number of independent measurements and total time (hours) measuring at* $q = 10$.

n	$n_{\text{independent}}$	total time (hours)
256	16384	5.2
512	71680	48.3
1024	24576	30.7
2048	4096	15.1
4096	4096	46.8
8192	1792	43.0
65536	1200	337.4
262144	1128	1410.2

A.2 Tables on Hausdorff dimension fits

Table A.11: *Fit results for fitting Equation (5.9) to the k_n of the dual graph distance in section 5.3.3 without shift s.*

d_H	a	b	δ
3.27 ± 0.05	0.987 ± 0.007	0.0014 ± 0.0012	0.69 ± 0.10
3.28 ± 0.04	0.988 ± 0.006	0.0017 ± 0.0014	0.65 ± 0.09
3.28 ± 0.04	0.989 ± 0.006	0.0015 ± 0.0011	0.68 ± 0.09
3.32 ± 0.09	0.990 ± 0.009	0.004 ± 0.005	0.55 ± 0.13
3.35 ± 0.09	0.987 ± 0.007	0.007 ± 0.007	0.49 ± 0.11
3.44 ± 0.15	0.981 ± 0.015	0.018 ± 0.021	0.39 ± 0.10
3.33 ± 0.09	0.990 ± 0.010	0.003 ± 0.004	0.58 ± 0.13
3.30 ± 0.06	0.989 ± 0.006	0.0038 ± 0.0031	0.57 ± 0.09
3.37 ± 0.12	0.989 ± 0.009	0.009 ± 0.011	0.47 ± 0.12
3.36 ± 0.13	0.987 ± 0.010	0.008 ± 0.011	0.48 ± 0.15

Table A.12: *Fit results for fitting Equation (5.9) to the k_n of the graph distance in section 5.3.3 without shift s.*

d_H	a	b	δ
3.38 ± 0.05	0.9855 ± 0.0035	0.010 ± 0.005	0.44 ± 0.05
3.27 ± 0.05	0.986 ± 0.007	0.0018 ± 0.0018	0.63 ± 0.12
3.27 ± 0.04	0.986 ± 0.007	0.0013 ± 0.0012	0.67 ± 0.11
3.27 ± 0.04	0.987 ± 0.006	0.0016 ± 0.0013	0.65 ± 0.09
3.25 ± 0.05	0.984 ± 0.008	0.0011 ± 0.0013	0.69 ± 0.14
3.31 ± 0.05	0.988 ± 0.005	0.0039 ± 0.0034	0.54 ± 0.09
3.30 ± 0.04	0.988 ± 0.006	0.0022 ± 0.0018	0.61 ± 0.09
3.29 ± 0.05	0.987 ± 0.005	0.0033 ± 0.0026	0.56 ± 0.09
3.30 ± 0.05	0.989 ± 0.005	0.0031 ± 0.0023	0.57 ± 0.08
3.26 ± 0.04	0.985 ± 0.006	0.0008 ± 0.0008	0.72 ± 0.11

Table A.13: *Fit results for fitting Equation (5.9) to the k_n of the dual graph distance in section 5.3.3 with shift s. Shaded in red are the removed fits.*

d_H	a	b	δ
3.561 ± 0.008	1.0040 ± 0.0028	$(0.0 \pm 2.1) \times 10^{-43}$	$(0 \pm 8) \times 10^{4}$
3.549 ± 0.005	0.9960 ± 0.0016	$(0.0 \pm 3.5) \times 10^{-39}$	$(0.0 \pm 1.5) \times 10^{5}$
$(0.0 \pm 3.2) \times 10^{8}$	0.01 ± 0.07	0.99 ± 0.08	0.3 ± 1.8
3.561 ± 0.012	0.998 ± 0.004	$(0 \pm 9) \times 10^{-40}$	$(0.0 \pm 2.8) \times 10^{5}$
$(0 \pm 4) \times 10^{9}$	0.01 ± 0.06	0.98 ± 0.06	0.3 ± 1.3
3.567 ± 0.007	0.9954 ± 0.0025	$(0.0 \pm 2.0) \times 10^{-44}$	$(0 \pm 8) \times 10^{4}$
3.568 ± 0.022	1.0016 ± 0.0020	0.0002 ± 0.0010	0.6 ± 0.5
3.563 ± 0.010	0.9998 ± 0.0035	$(0 \pm 4) \times 10^{-44}$	$(0.0 \pm 2.1) \times 10^{5}$
3.550 ± 0.006	0.9977 ± 0.0022	$(-0 \pm 6) \times 10^{-41}$	$(0.0 \pm 1.3) \times 10^{5}$
6 ± 32	0.1 ± 0.8	0.9 ± 0.8	0.1 ± 0.8

Table A.14: *Fit results for fitting Equation (5.9) to the k_n of the graph distance in section 5.3.3 with shift s. Shaded in red are the removed fits.*

d_H	a	b	δ
3.519 ± 0.015	0.996 ± 0.005	$(-0 \pm 7) \times 10^{-45}$	$(0.0 \pm 1.7) \times 10^{5}$
3.519 ± 0.018	0.991 ± 0.008	0.010 ± 0.018	-1 ± 5
3.534 ± 0.011	0.992 ± 0.005	0.008 ± 0.012	-2 ± 5
3.540 ± 0.007	0.9972 ± 0.0027	$(-0.0 \pm 1.4) \times 10^{-39}$	$(0 \pm 6) \times 10^{3}$
3.552 ± 0.010	0.993 ± 0.005	0.007 ± 0.014	$(-0.0 \pm 2.8) \times 10^{6}$
3.558 ± 0.009	0.9965 ± 0.0023	$(1 \pm 7) \times 10^{-6}$	1.3 ± 0.7
3.56 ± 0.04	1.0017 ± 0.0028	0.0004 ± 0.0024	0.5 ± 0.6
6 ± 22	0.1 ± 0.4	0.9 ± 0.4	0.1 ± 0.5
3.537 ± 0.006	0.9982 ± 0.0020	$(0.0 \pm 2.3) \times 10^{-43}$	$(0.0 \pm 1.0) \times 10^{4}$
$(0 \pm 6) \times 10^{8}$	0.01 ± 0.10	0.99 ± 0.10	0.3 ± 2.7

Bibliography

[1] P. Di Francesco, E. Guitter, and J. L. Jacobsen, "Exact meander asymptotics: a numerical check", Nuclear Physics B **580**, 757–795 (2000).

[2] P. Di Francesco, O. Golinelli, and E. Guitter, "Meanders: exact asymptotics", Nuclear Physics B **570**, 699–712 (2000).

[3] P. Di Francesco and E. Guitter, "Geometrically constrained statistical systems on regular and random lattices: From folding to meanders", Physics Reports **415**, 1–88 (2005).

[4] D. Griffiths, *Introduction to electrodynamics* (Pearson Education, 2014).

[5] A. Levan, *Introduction to General Relativity* (2020).

[6] T. Budd, "Non-perturbative quantum gravity: a conformal perspective", PhD thesis (University of Utrecht, 2012).

[7] N. Klitgaard, "New curvatures for quantum gravity nilas klitgaard new curvatures for quantum gravity", PhD thesis (Radboud Universiteit Nijmegen, 2022).

[8] C. Kiefer, "Quantum gravity: general introduction and recent developments", 10.1002/andp.200510175 (2005).

[9] C. Garban, "Quantum gravity and the kpz formula", (2012).

[10] P. Di Francesco, O. Golinelli, and E. Guitter, *Meander, folding, and arch statistics*, Vol. 26, 8-10 (1997), pp. 97–147.

[11] G. Chapuy, *An introduction to map enumeration*, www.irif.fr, 2014.

[12] N Curien, *Peeling of random planar maps*, www.imo.universite-paris-saclay.fr, 2021.

[13] T. Budd, *Monte carlo techniques*, gitlab.science.ru.nl/tbudd/monte-carlo-techniques-2021, 2021.

[14] A. Carrance, "Triangulations colorées aléatoires", PhD thesis (Université de Lyon, 2019).

[15] R. J. Wilson, *Introduction to graph theory* (Longman, 1996).

[16] S. Carroll, *Spacetime and geometry* (Pearson Education, Philadelphia, PA, 2003).

[17] D. Tong, "4. Introducing Conformal Field Theory", String Theory Notes **241**, 61–107 (2009).

[18] R. Pathria and P. D. Beale, "12 - phase transitions: criticality, universality, and scaling", in *Statistical mechanics (fourth edition)*, edited by R. Pathria and P. D. Beale, Fourth Edition (Academic Press, 2022), pp. 417–486.

[19] P. Koster, "Universality classes of 2D hyperbolic Riemannian manifolds", bachelor thesis (Radboud Universiteit Nijmegen, 2022).

[20] J. Barkley and T. Budd, "Precision measurements of hausdorff dimensions in two-dimensional quantum gravity", Classical and Quantum Gravity **36**, 244001 (2019).

[21] J. Ding, J. Dubedat, and E. Gwynne, "Introduction to the liouville quantum gravity metric", (2021).

[22] T. Budd and A. Castro, "Scale-invariant random geometry from mating of trees: a numerical study", (2022).

[23] J. Ambjørn, S. Jain, and G. Thorleifsson, "Baby universes in 2d quantum gravity", Physics Letters B **307**, 34–39 (1993).

[24] S. Jain and S. D. Mathur, "World-Sheet Geometry and Baby Universes in 2-D Quantum Gravity", 10.1016/0370-2693(92)91769-6 (1992).

[25] T. Budd, *Monte carlo methods in dynamical triangulations*, hef.ru.nl/ tbudd/randgeom/, 2017.

[26] W. van der Feltz, "Matter coupling to two-dimensional Causal Dynamical Triangulations", master thesis (2021).

[27] J. Ding and E. Gwynne, "The fractal dimension of liouville quantum gravity: universality, monotonicity, and bounds", Communications in Mathematical Physics **374**, 1877–1934 (2019).

[28] J. Ambjørn, K. Anagnostopoulos, and R. Loll, "Crossing the $c = 1$-barrier in 2d lorentzian quantum gravity", Physical Review D **61**, 10.1103/physrevd.61.044010 (2000).

[29] S. Sheffield, *Lecture on universal randomness in 2d*, youtube.com/watch?v=TXVC8ZegYwg.

[30] J. L. Jacobsen and J. Kondev, "Field theory of compact polymers on the square lattice", Nuclear Physics B **532**, 635–688 (1998).

[31] M. T. Batchelor, H. W. Blöte, B. Nienhuis, and C. M. Yung, "Critical behaviour of the fully packed loop model on the square lattice", Journal of Physics A: Mathematical and General **29**, L399 (1996).

[32] P. D. Francesco, "Folding and coloring problems in mathematics and physics", Bulletin (New Series) of the American Mathematical Society **37** (2000).

[33] J. Cardy, *Conformal Field Theory and Statistical Mechanics* *, www-thphys.physics.ox.ac.uk/people/JohnCardy/lh2008.pdf, 2008.

[34] J. L. Jacobsen and J. Kondev, "Transition from the compact to the dense phase of two-dimensional polymers", Journal of Statistical Physics **96**, 21–48 (1999).

[35] B. A. Berg, "Introduction to markov chain monte carlo simulations and their statistical analysis", Markov Chain Monte Carlo: Innovations And Applications **9**, 1–52 (2005).

[36] W. Krauth, *Statistical mechanics : algorithms and computations*, English (Oxford University Press, Oxford SE - XII, 342 pages + 1 CD-ROM., 2006).

[37] G. T. B. Mark E. J. Newman, *Monte Carlo methods in statistical physics* (Clarendon Press, Oxford, England, Dec. 1999).

[38] A. Joseph, *Markov Chain Monte Carlo Methods in Quantum Field Theories: A Modern Primer*, December (2019).

[39] P. Young, "Everything you wanted to know about Data Analysis and Fitting but were afraid to ask", (2012).

[40] W. Janke, "Statistical analysis of simulations: data correlations and error estimation", Quantum **10**, 423–445 (2002).

[41] D. N. Politis and J. P. Romano, *The stationary bootstrap* (1994), pp. 1303–1313.

[42] B. Krüger, "Simulating triangulations: graphs, manifolds and (quantum) spacetime", PhD thesis (FAU University Press, 2016), xiv, 469 S.

[43] C. Bauer, "The phase transition of spin models coupled to dynamical triangulations.", bachelor thesis (2021).

[44] D. P. Landau and K. Binder, *A guide to monte carlo simulations in statistical physics*, en, 3rd ed. (Cambridge University Press, Cambridge, England, Sept. 2009).

[45] O. Golinelli, "A monte-carlo study of meanders", European Physical Journal B **14**, 145–155 (2000).

[46] I. Jensen and A. J. Guttmann, "Critical exponents of plane meanders", Journal of Physics A: Mathematical and General **33**, 10.1088/0305-4470/33/21/101 (2000).

[47] S. Legendre, "Foldings and meanders", Australasian Journal of Combinatorics **58**, 275–291 (2014).

[48] J. Sawada and R. Li, "Stamp foldings, semi-meanders, and open meanders: fast generation algorithms", The Electronic Journal of Combinatorics **19**, 10.37236/2404 (2012).

[49] D. D. Sleator and R. E. Tarjan, "Self-adjusting binary search trees", Journal of the ACM **32**, 652–686 (1985).

[50] *Introducing json*, www.json.org.

[51] J. D. Foley, M. A. Fischler, and R. C. Bolles, *Graphics and image processing random sample consensus: a paradigm for model fitting with apphcatlons to image analysis and automated cartography* (1981).

[52] *Scikit-learn*, scikit-learn.org.

[53] G Thorleifsson and B Petersson, *Beyond the c = 1 barrier in two-dimensional quantum gravity* (1998), pp. 745–747.

[54] J. Ambjørn, P. Białas, J. Jurkiewicz, Z. Burda, and B. Petersson, "Effective sampling of random surfaces by baby universe surgery", Physics Letters B **325**, 337–346 (1994).

[55] E. van der Velden, "CMasher: Scientific colormaps for making accessible, informative and 'cmashing' plots", The Journal of Open Source Software **5**, 2004, 2004 (2020).

[56] T. Budd, *Planarmap.js*, github.com/tgbudd/planarmap.js, 2018.